BULK CRYSTAL GROWTH, CHARACTERIZATION AND THERMODYNAMIC ANALYSIS OF ALUMINUM NITRIDE AND RELATED NITRIDES

by

LI DU

B.S., East China University of Science and Technology, 2004

AN ABSTRACT OF A DISSERTATION

submitted in partial fulfillment of the requirements for the degree

DOCTOR OF PHILOSOPHY

Department of Chemical Engineering
College of Engineering

KANSAS STATE UNIVERSITY
Manhattan, Kansas

2011

Abstract

The sublimation recondensation crystal growth of aluminum nitride, titanium nitride, and yttrium nitride were explored experimentally and theoretically. Single crystals of these nitrides are potentially suitable as substrates for AlGaInN epitaxial layers, which are employed in ultraviolet optoelectronics including UV light-emitting diodes and laser diodes, and high power high frequency electronic device applications.

A thermodynamic analysis was applied to the sublimation crystal growth of aluminum nitride to predict impurities transport (oxygen, carbon, and hydrogen) and to study the aspects of impurities incorporation for different growth conditions. A source purification procedure was established to minimize the impurity concentration and avoid degradation of the crystal's properties. More than 98% of the oxygen, 99.9% of hydrogen and 90% of carbon originally in the source was removed. The AlN crystal growth process was explored in two ways: self-seeded growth with spontaneous nucleation directly on the crucible lid or foil, and seeded growth on SiC and AlN. The oxygen concentration was 2 ~ 4 x $10^{18}cm^{-3}$, as measured by secondary ion mass spectroscopy in the crystals produced by self-seeded growth. Crystals grown from AlN seeds have visible grain size expansion. The initial AlN growth on SiC at a low temperature range (1400°C ~1600°C) was examined to understand the factors controlling nucleation. Crystals were obtained from *c*-plane on-axis and off-axis, Si-face and C-face, as well as *m*-plane SiC seeds. In all cases, crystal growth was fastest perpendicular to the *c*-axis.

The growth rate dependence on temperature and pressure was determined for TiN and YN crystals, and their activation energies were 775.8±29.8kJ/mol and 467.1±21.7kJ/mol respectively. The orientation relationship of TiN (001) || W (001) with TiN [100] || W [110], a 45^{o} angle between TiN [100] and W [100], was seen for TiN crystals deposited on both (001) textured tungsten and randomly orientated tungsten. X-ray diffraction confirmed that the YN crystals were rock-salt structure, with a lattice constant of 4.88Å. Cubic yttria was detected in YN sample from the oxidation upon its exposed to air for limited time by XRD, while non-cubic yttria was detected in YN sample for exposures more than one hour by Raman spectra.

BULK CRYSTAL GROWTH, CHARACTERIZATION AND THERMODYNAMIC ANALYSIS OF ALUMINUM NITRIDE AND RELATED NITRIDES

by

LI DU

B.S., East China University of Science and Technology, 2004

A DISSERTATION

submitted in partial fulfillment of the requirements for the degree

DOCTOR OF PHILOSOPHY

Department of Chemical Engineering
College of Engineering

KANSAS STATE UNIVERSITY
Manhattan, Kansas

2011

Approved by:

Major Professor
James H. Edgar

Copyright

Abstract

The sublimation recondensation crystal growth of aluminum nitride, titanium nitride, and yttrium nitride were explored experimentally and theoretically. Single crystals of these nitrides are potentially suitable as substrates for AlGaInN epitaxial layers, which are employed in ultraviolet optoelectronics including UV light-emitting diodes and laser diodes, and high power high frequency electronic device applications.

A thermodynamic analysis was applied to the sublimation crystal growth of aluminum nitride to predict impurities transport (oxygen, carbon, and hydrogen) and to study the aspects of impurities incorporation for different growth conditions. A source purification procedure was established to minimize the impurity concentration and avoid degradation of the crystal's properties. More than 98% of the oxygen, 99.9% of hydrogen and 90% of carbon originally in the source was removed. The AlN crystal growth process was explored in two ways: self-seeded growth with spontaneous nucleation directly on the crucible lid or foil, and seeded growth on SiC and AlN. The oxygen concentration was 2 ~ 4 x $10^{18}cm^{-3}$, as measured by secondary ion mass spectroscopy in the crystals produced by self-seeded growth. Crystals grown from AlN seeds have visible grain size expansion. The initial AlN growth on SiC at a low temperature range (1400°C ~1600°C) was examined to understand the factors controlling nucleation. Crystals were obtained from *c*-plane on-axis and off-axis, Si-face and C-face, as well as *m*-plane SiC seeds. In all cases, crystal growth was fastest perpendicular to the *c*-axis.

The growth rate dependence on temperature and pressure was determined for TiN and YN crystals, and their activation energies were 775.8±29.8kJ/mol and 467.1±21.7kJ/mol respectively. The orientation relationship of TiN (001) || W (001) with TiN [100] || W [110], a 45^{o} angle between TiN [100] and W [100], was seen for TiN crystals deposited on both (001) textured tungsten and randomly orientated tungsten. X-ray diffraction confirmed that the YN crystals were rock-salt structure, with a lattice constant of 4.88Å. Cubic yttria was detected in YN sample from the oxidation upon its exposed to air for limited time by XRD, while non-cubic yttria was detected in YN sample for exposures more than one hour by Raman spectra.

Table of Contents

List of Figures

List of Tables

Acknowledgements

One finger cannot lift a small stone. A challenging project of this nature is never exclusively the work of one person. This research would not have been successful without the support, encouragement and recommendation I received from my advisory committee, colleagues, and friends in the past few years.

My sincerest gratitude to my major professor Dr. James H. Edgar. Your guidance and wisdom have been critical to my progress in this research.

I thank my many collaborators for their contribution in my study.

I thank my many group members for their help in my work.

Dedication

To My Family

Especially To

My Father 杜如诗

And

My Mother 郭新霞

Without whose love, support and encouragement,

I would not be where I am and who I am today

Preface

This PhD thesis is a result of my research study in Chemical Engineering department at Kansas State University. This work was supported by National Science Foundation and II-VI Foundation.

CHAPTER 1 - Introduction

Materials and material development are fundamental to our culture, symbolizing major historical periods of our society. The constant development of semiconductor materials which form the heart and soul of all electronic devices then results in continuous improvement of modern life. It is expected that solid state lighting devices such as light emitting diodes (LEDs) will replace incandescent light bulbs and fluorescent lamps for energy savings and durability consideration. Group III nitrides (AlN, GaN, InN) and their alloys are the leading material system for, but not limited to, applications as LEDs and laser diodes (LDs) covering the spectral wavelength from near infrared to deep ultraviolet. However, AlGaInN device technology is limited by the lack of thermally and lattice-matched substrates. The high defect density in overgrown active layers and cracking of the device layers due to the large thermal mismatch degraded device performance and lifetime. Thus, native substrates that enable homoepitaxial growth of AlGaInN layers are in high demand.

This dissertation focuses on investigating the growth of potential substrates suitable for the AlGaInN epitaxial layers development with improved efficiency and long lifetime. In this section, the basic concepts, structure and evolution of LEDs and LDs as well as the advantages of group III nitrides material system will be discussed in general. The UV LEDs will be discussed in greater detail, as challenges still remain in this field such as substrates limitation, while visible range LEDs have entered the age of maturity. The motivation of the research and a dissertation overview are also included.

1.1 Lighting Emitting Diodes and Laser Diodes

1.1.1 Background

The development of electricity and electrically powered light sources such as Edison's light bulb were important achievements setting the cornerstone for modern lifestyles. New developments in this field are constantly being made, and two of the most important are LEDs and LDs based on electroluminescence (EL). EL, which was discovered more than one hundred years ago,[1] is a phenomenon in which a material emits light in response to the passage of an electric current or to a strong electric field. Compared to traditional light sources, LEDs are smaller, brighter, more reliable, more durable and more efficient. Electrical-to-optical energy conversion efficiencies over 50% have been achieved in infrared light emitting devices. If similar efficiencies were achieved in visible light emitting devices, the result would be a 150-200 lm/W white light source that is two times more efficient than fluorescent lamps, and ten times more efficient than incandescent lamps. This could reduce the global electricity consumption used for lighting by 50% by 2025.[2] In fact, since device lifetimes easily exceed 10,000 hours compared to ~1,500 hours for light bulbs, LEDs have already begun to replace incandescent and fluorescence in many applications, such as traffic signal lights, automotive instrument panels, mobile phone backlighting, aviation cockpit displays, and architectural directed-area lighting.

1.1.2 History

The history of LEDs can be traced back to more than one hundred years ago when Henry Round at Marconi Labs noticed light emission from a SiC crystallite in 1907[1].

Independently, a Russian scientist, Oleg Losev, discovered light emission from SiC in 1920's[3]. It was not until 1960's that LEDs were extensively investigated, when high quality III-V compounds first became available.

The year 1962 was monumental for both LEDs and LDs. Infrared LEDs and lasers based on GaAs which were commercialized later in 1964, were first reported by groups working at RCA, GE, IBM and MIT[4]. The first Infrared LD was also demonstrated in this year by two different groups from GE and IBM respectively.[5, 6] In same year the first visible-spectrum (red) LD was reported by Nick Holonyak Jr.[7], who was also the first to make a practical visible-spectrum (red) LED[4]. However, LEDs suffered from low brightness and efficiency during 1960's and 1970's. LED displays could not be read under bright outdoor conditions and their high power consumption made frequent battery recharges necessary[4]. It was not until 1980's, AlGaInP visible LEDs was developed, which offered a higher level of versatility as far as the LED's color output was concerned. Today AlGaInP is still the dominant materials system for high-brightness emitters in the red, orange and yellow spectral range.

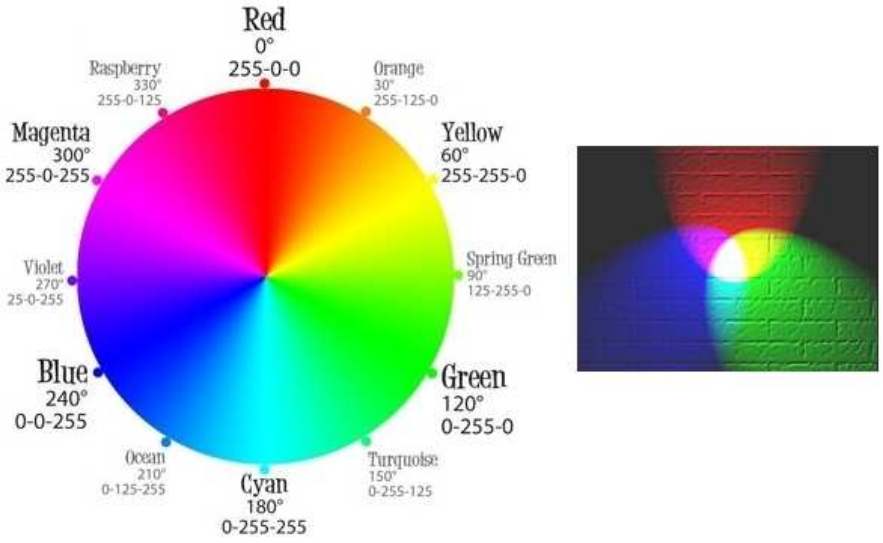

Figure 1.1 RGB color wheel and an example of LED light.

In order to create a full color image, the additive colors used in LED systems are red, green and blue (RGB color model), though RYB color model (red, yellow, blue) is more popular in history especially among artists. Figure 1.1 is the RGB color wheel and an example of LED light. By the late 1960's, technologies for red and green LEDs were available, but comparable technology was not available for blue LEDs. It was not until nearly 30 years later that commercially viable blue LEDs were developed. In 1992, the first GaN LED that emitted light in UV and blue spectral range was reported[8]. Later, after the demonstration of the first viable blue and green GaInN double heterostructure LED that achieved efficiencies of 10% by Shuji Nakamura and co-workers[9], white LEDs were developed.

1.1.3 Structure

Figure 1.2 shows the inner working of a LED; current flows easily from the p-side (anode) to the n-side (cathode). When an electron recombines with a hole radiatively, it falls into a lower energy level, emitting light. The energy of the light emitted depends on the band gap energy of the materials forming the p-n junction. Therefore the larger the band gap, the shorter the photon wavelength.

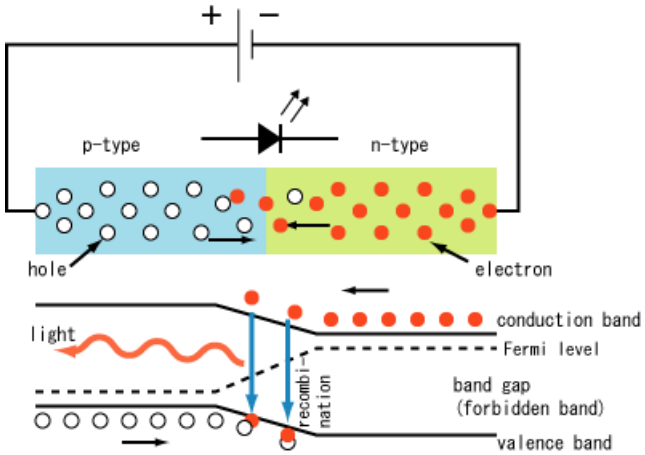

Figure 1.2 The inner workings of an LED

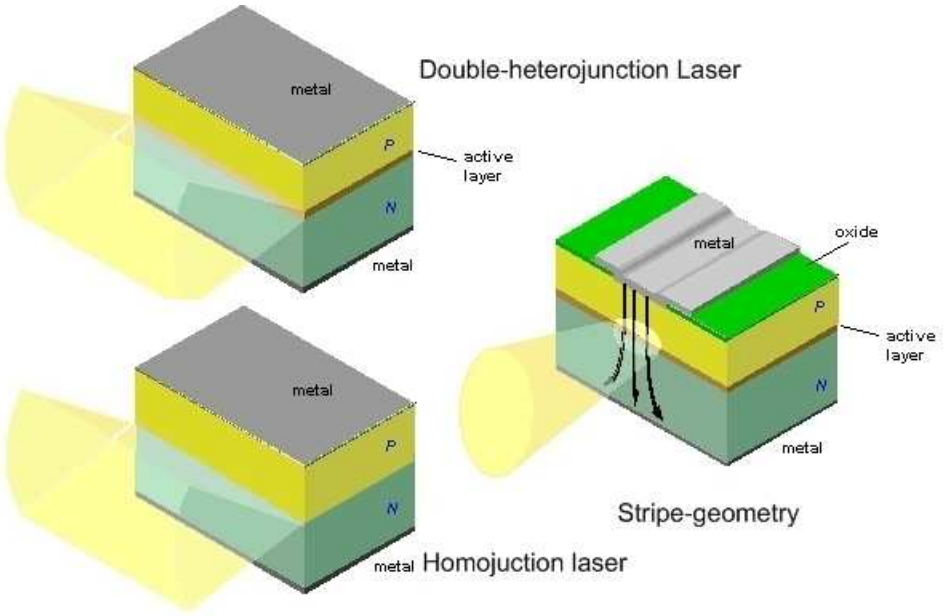

Figure 1.3 Three semiconductor laser structures

Figure 1.3 shows three basic laser structures: a homojunction laser has same semiconductor material (e.g. GaAs) on both side of the junction, enabling Fabry-Perot cavity to enhance laser action; a double-heterojunction (DH) laser has a thin layer of semiconductor (e.g. GaAs) sandwiched between layers of a different semiconductor (e.g. $Al_xGa_{1-x}As$); and a DH laser with strip geometry. In a DH laser, the carrier and optical field are confined within the active region to establish laser condition. If a strip geometry was build in the DH laser, the required operating current is reduced, the multiple-emission areas along the junction are eliminated, and the reliability is improved by removing most of the junction perimeter.[10]

1.2 Why III-Nitrides

1.2.1 The demand for direct bandgap semiconductors

The three basic processes for interaction between a photon and an electron in a solid are absorption, spontaneous emission and stimulated emission. The dominant

operating process for LEDs is spontaneous emission; for the LDs it is stimulated emission; and for photodetectors and solar cells it is absorption. Photons are emitted due to the recombination of the charge carriers, and photons are absorbed to create charge carriers. The recombination process that emits photon with the wavelength corresponding to the energy released is called radiative recombination, and it's a form of spontaneous emission. Photons presented in the material can either be absorbed, generating a pair of free carriers, or stimulate a recombination event (stimulated emission), resulting in a generated photon with similar properties to the one responsible for the event. The spontaneous emission and stimulated emission occur readily in semiconductor having direct bandgaps, but is more difficult in semiconductors having indirect bandgaps because the crystal momentum is conserved and the radiative- transition probability in a direct bandgap semiconductor is high[10]. For example, Si (indirect bandgap) is extremely inefficient at emitting light. The electrons and holes in Si usually have non-radiative commonly recombination which produces no optical emission. Therefore LEDs and LDs are almost always made of direct band gap materials.

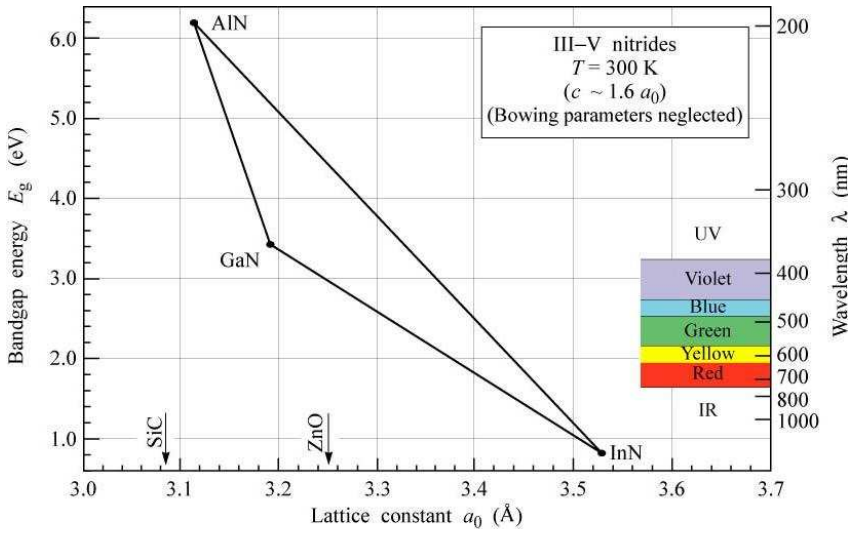

Figure 1.4 Bandgap energy versus lattice constant of III nitrides at room temperature*
***Published figure by E. F. Schubert[4]**

1.2.2 The enormous variety of broad spectra wavelength

Because of the wide direct bandgap of the three binary semiconductors InN, GaN, and AlN, the group III nitrides span a very wide range of wavelengths, covering the deep ultraviolet, near ultraviolet, visible, and even near infrared spectral range. The band gap energy versus lattice constant of AlGaInN materials system is shown in Figure 1.4[4]. No other material system offers such wide range of direct bandgap. In contract, the AlGaInP material system is suited for high-brightness LEDs only in the red, orange, amber and yellow wavelength ranges; AlGaAs is limited to only red LEDs. Unlike most semiconductors, the radiative efficiency of group III nitrides exhibits low sensitivity to presence of dislocations. They have much higher tolerance towards dislocations as compared to group III arsenides and phosphides.

1.3 Ultraviolet LEDs

After 30 years investigation from 1960's to 1990's and nearly 20 years of development since then, visible range LEDs have entered the age of maturity and are now posed to replace incandescent bulbs for general lighting applications[11]. Beyond the visible range, compact high-efficiency ultraviolet LEDs and LDs are potentially more efficient alternatives to large, toxic, low-efficiency gas lasers and mercury lamps. Microelectronic fabrication technologies need shorter wavelength light source for photolithography, to improve the resolution. DUV LEDs with wavelength from 260 to 280 nm have found applications in water/air/surface sterilization and decontamination[11]. Figure 1.5 illustrates the progress in LED development with projected performance for UV LEDs. The energy range of AlN/GaN/AlGaN compounds allow covering the UV

band from UVA (320–400 nm) and UVB (280–320 nm) all the way into the UVC range (100–280 nm) [11]. The shortest achievable wave length is on the order of 210 nm based on *c*-plane (chapter two) AlN PIN (p-type/intrinsic/n-type) homojunction LED .[12] This same wavelength has also been demonstrated for *a*-plane (chapter two) AlN p–n junction LED and its higher emission intensity along the surface normal than that of conventional *c*-plane (chapter two) LED was reported.[13]

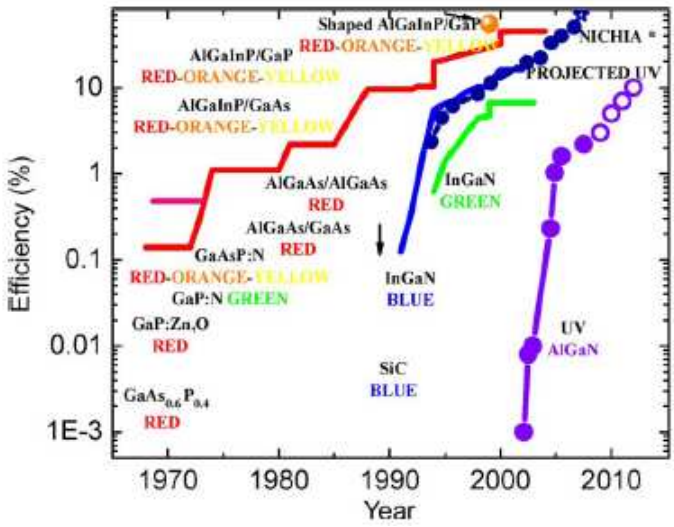

Figure 1.5 LED achieved and projected (for DUV LEDs)*

*** Published figure by M. S. Shur and R. Gaska[11].**

However, ultraviolet LEDs have not revealed their full potential yet due to the disadvantages of currently used substrates. The common substrates for AlGaInN epitaxial layers for electronic and optoelectronic devices applications are sapphire and silicon carbide. The large difference between the refractive indices of sapphire (1.75) and group III nitrides (~2.3 in GaN, ~2.15 in AlN, and ~2.9 in InN) is the origin of light waveguiding in a heterostructure on sapphire substrates, which lowers the efficiency of light extraction from the LED[14]. The waveguiding effect is negligible in LED structures grown on SiC substrates. But SiC substrates are transparent only to visible light, not to UV light. The problems of light extraction are so critical that it is necessary to remove the

substrates after the growth of LED structures to increase the overall LED efficiency.[14] In addition, DUV LEDs require AlGaN epilayers with high aluminum content. Although blue and green LEDs based on InGaN work quite well despite a high density of dislocations (10^8 cm^{-2}), the luminescence efficiency is sensitive to defect densities in the AlGaN epitaxial layers. High threading dislocation density (TDD) result from large lattice mismatch of heterostructure substrates induce an intensive non-radiative carrier recombination in optoelectronic devices, LEDs and laser diodes (LDs), reducing the internal quantum efficiency[14]. AlN and AlGaN films grown on such substrates beyond critical thicknesses suffer from cracking due to the strong tensile strain[11]. This problem can be alleviated by using native AlN substrates to form homostructures.[11, 14, 15] All in all, aluminum nitride single crystal are good candidates for DUV LEDs substrates. Furthermore, AlN itself a good source of UV LDs.

1.4 Research Overview

The research goal of this dissertation is to investigat possible substrates suitable for AlGaInN epitaxial layers. Epitaxial heterostructures of group III nitrides are the remarkable materials for a broad range of applications in electronics and optoelectronics. In the applications of EL, the red, green and blue LEDs grown on foreign substrates are commercially available; blue solid state lasers have also been demonstrated[16], but the technology for the UV LEDs and LDs technology remains to be developed. High TDD, non-UV transparence, poor thermal conductivity, and cracking of the device layers due to the large thermal mismatch are the major drawbacks of commonly used and commercialized substrates. Native AlN substrates might alleviate these problems. However, currently commercially available AlN substrates are still cost prohibitive and

have a limited usable area. Additionally, the presence of impurities in AlN such as oxygen degrades its thermal conductivity, causes structure failure, and consumes light generated by the AlN based device.

Metal nitride substrates are attractive because their electrical conductivity can simplify the device structures. Electrical current can pass through the substrateas an option that is not possible with sapphire. This reduces resistive energy losses and the area required for the device making high device packing densities possible. Transition metal nitrides such as ScN and TiN are attractive candidates for combining as layered structures or alloys with gallium nitride and related group III nitride semiconductors, because they can have similar lattice constants, share a common element and exhibit dual properties characteristics of both covalent compounds and metals.

In this dissertation, the bulk crystal growth of AlN, TiN, and YN were investigated experimentally and theoretically. Chapter 2 is the literature review of AlN and related nitrides. Chapter 3 describes the experimental equipment and material characterization methods. Chapter 4 provides the thermodynamic analysis for impurity incorporation and source purification. Chapter 5 reports bulk crystal growth of AlN including both self-seeded growth and seed growth on SiC. The nitial nucleation of AlN grown at low temperature on SiC as a function of crystal plane, and tilt degree and angle is studied. Chapter 6 and chapter 7 are the investigation of the bulk crystal growth and characterization of TiN and YN respectively. Chapter 8 is the research conclusion.

1.5 References

[1] H. J. Round, *A note on carborundum*, Electrical World, **49**, 309 (1907)

[2] "The Promise of Solid State Lighting" OIDA Report, (2001)

[3] Losev, O. V. *Luminous Carborundum Detector and Detection Effect and Oscillations with Crystals*, Phil. Mag. **6**, 1024 (1928)

[4] E. F. Schubert , Light Emitting Diodes, 2nd, Cambridge University Press, (2006)

[5] R. N.Hall, G. E. Fenner, J. D. Kingsley, T. J. Soltys, R. O. Carlson, *Coherent Light Emission From GaAs Junctions*, Physical Review Letters, **9**, 366 (1962)

[6] M. I. Nathan, W. P. Dumke, G. Burns, F. H. Dill, G. Lasher, *Stimulated Emission of Radiation from GaAs p-n Junctions*, Applied Physics Letters **1**, 62 (1962)

[7] N. Holonyak Jr., S. F. Bevacqua, *Coherent (Visible) Light Emission from* $Ga(_{As1-x}P_x)$ *Junctions*, Appl. Phys. Lett., **1**, 82 (1962)

[8] Akasaki I., *GaN based UV/blue Light-emmitting Deveices*, GaAs and related compounds conference, Inst, Conf, Ser. **129**, 851 (1992)

[9] S. Nakamura, *High-brightness InGaN Blue, Green and Yellow Light-emitting diodes with Quantum-well Structure*, J. Appl. Phys. **34**, 797 (1995)

[10] S. M. Sze, Semiconductor Devices: physics and technology, 2nd, Wiley, (2002)

[11] M. S. Shur and R. Gaska, *Deep-Ultraviolet Light-Emitting Diodes*, IEEE Transac. Electron devices, **57**,12 (2006)

[12] Y. Taniyasu, M. Kasu, and T. Makimoto, *An Aluminium Nitride Light-emitting Diode with A Wavelength of 210 Nanometres,* Nature, **441**, 325 (2006)

[13] Y. Taniyasu and M. Kasu, *Surface 210 nm light Emission from An AlN p–n Junction Light-emitting Diode Enhanced by a-plane Growth Orientation*, Appl. Phys. Lett. **96**, 221110 (2010)

[14] V. F. Mymrin, K. A. Bulashevich, N. I. Podolskaya, S. Yu. Karpov, *Bandgap Engineering of Electronic and Optoelectronic Dvices on Native AlN and GaN Substrates: a modeling insight*, t J. Cryst. Growth, **281**, 115 (2005)

[15] M. Kneissl, Z. Yang, M. Teepe, C. Knollenberg, O. Schmidt, P. Kiesel, N. M. Johnson, S. Schujman, and L. J. Schowalter, *Ultraviolet Semiconductor Laser Diodes on Bulk AlN*, J. Appl. Phys., **101**, 123103 (2007)

[16] S. Nakamura, M. Senoh, S. Nagahama, N. Iwasa, T. Yamada, T. atsushita, H. Kiyuku, Y. Sugimoto, T. Kuzaki, H. Umemoto, and K. Chocho, *Continuous-wave Operation of InGaN/GaN/AlGaN-based Laser Diodes Grown on GaN Sabstrates*, Appl. Phys. Lett. **72**, 201, (1998).

CHAPTER 2 - Aluminum Nitride and Related Nitrides

The history of the production of aluminum nitride can be traced back to 19th century as it does not occur naturally. Briegleb and Geyther[17] first synthesized AlN as a powder from liquid Al and N_2 gas in 1862. Later in 1899, Ahrons[18] reported the synthesis of AlN powder by applying a direct current arc between two Al electrodes in nitrogen. However, both methods were limited by the protective AlN film that formed on the surface of Al; it prevented the further reaction and resulted in Al-rich powders. The synthesis of AlN has greatly advanced in 20th century; many different methods have been reported for producing AlN in the form of powder, crystals, whiskers and other macro structures. However, for applications of electronic and photovoltaic devices, growth of high-purity AlN single crystals remains challenging. This chapter gives a brief review of the crystal structure, material properties, applications and crystal growth of AlN and related nitrides. The structure of silicon carbide (SiC) is also discussed here as SiC is an good seed crystal for controlling the orientation of AlN in its crystal growth.

2.1 Crystalline Structure of AlN, SiC and related nitrides

In crystallography, Miller indices with three integers are the common notation system for planes and directions in the crystal (Bravais) lattices. A direction is defined as a line or a vector between two points. It is denoted as [*uvw*] where *u*, *v*, and *w* are the integers correspond to the reduced projections along the *x*, *y*, and *z* axes respectively. And the equivalent directions in a crystal structure are grouped together in a direction family denoted as <*uvw*>. However in hexagonal crystal structure, some crystallographic

equivalent directions do not have same set of indices. So in the case of hexagonal or rhombohedral lattice systems Bravais-Miller index with 4 numbers works better. Conversion from the three-index system to the four-index system, *[uvw]* → *[u'v't w']* is accomplished by the following formulas[19] :

$$u' = n(2u - v)/3 \quad \textbf{(2-1)}$$

$$v' = n(2v - u)/3 \quad \textbf{(2-2)}$$

$$t = -(u' + v') \quad \textbf{(2-3)}$$

$$w' = nw \quad \textbf{(2-4)}$$

where the *u' v' t* are the integers pertaining to the projections along the respective three axes which have 120^{o} between each other in the basal plane, and *w'* are the integers perpendicular the basal plane. The planes for a crystal structure are represented in a similar way. The notation (*hkl*) denotes a plane orthogonal to a direction [*hkl*] and {*hkl*} denotes the set of all planes that are equivalent to (*hkl*) by the symmetry of the lattice.

2.1.1 Crystal Structure of AlN and related Nitrides

The common group III nitrides share the same three crystal structures: wurtzite (α-phase), zincblende (β-phase) and rocksalt (NaCl) structures, as shown in Figure 2.1. At thermodynamic equilibrium, aluminum nitride, gallium nitride and indium nitride have the hexagonal wurtzite structure. The cubic zincblende structure for GaN and InN can be stabilized by epitaxial growth of thin films on the (001) crystal planes of cubic substrates such as Si and GaAs[20]. The rocksalt or NaCl structure can be induced in AlN, GaN and InN at very high pressures[20]. The rocksalt structure is also the equilibrium crystal structure for TiN, YN, ScN and ZrN. Detailed information on the three structures is listed in Table 2.1.

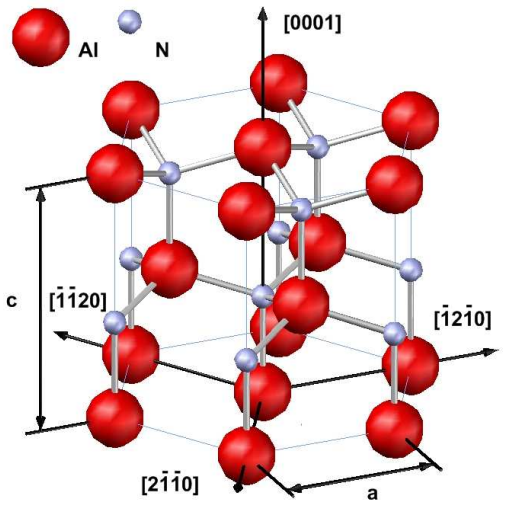

a. Wurtzite structure.

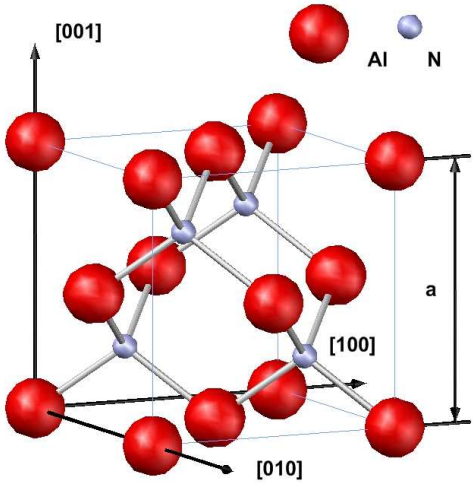

b. Zincblende structure.

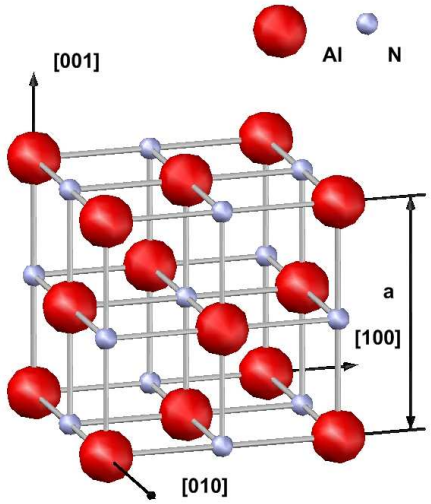

c. Rocksalt structure.

Figure 2.1 Three common crystal structures for group III nitrides.

Table 2.1 Crystal structures.

	wurtzite	zincblende	rocksalt
Space group	$P6_3mc(C_{6v}^4)$	$F\bar{4}3m(T_d^2)$	$Fm3M(O_h^5)$
Lattice system	Hexagonal	Cubic	Cubic
Structure at Equilibrium	AlN, GaN, InN, 4H-SiC, 6H-SiC(α)	3C-SiC (β)	TiN, ZrN, ScN, YN

The wurtzite structure has a hexagonal unit cell and is non-centrosymmetric with (0001) as the primary polar plane. It consists of two interpenetrating hexagonal close packed (HCP) sublattices that are formed by two individual atom types offset along the c-axis by 5/8 of the cell height. It has three lattice parameters: the hexagonal prism edge length **a**, the hexagonal prism height **c**, and the cation-anion bond length ratio **u** along the [0001] axis in the unit of **c**.

Both the zincblende and the rocksalt structure have cubic unit cells with a single lattice parameter **a**. The zincblende has (111) as the primary polar plane with atom positions the same as the diamond crystal structure and can be considered as two interpenetrating face centered cubic (FCC) sublattices that are formed by two individual atom types offset by one quarter of the distance along a body diagonal. The rocksalt crystal structure has a NaCl structure with (111) as primary polar plane and can be described as interpenetrating FCC sublattices each with one type of atom, but offset along the cube edge by half the edge length.

Both the wurtzite and the zincblende crystal structures have close-packed planes and each atom (i.e. nitrogen) is tetrahedrally coordinated by four atoms of the different type (i.e. III-metal atoms). But the stacking sequence of the N and metal atom bilayers along their primary polar plane directions either [0001] or [111] is different. The second nearest neighbor atom pairs are eclipsed in the wurtzite structure but are staggered in the

zincblende structure (Figure 2.2a). If the atom pairs in the basal plane are labeled as A, then the atom pairs in the next layer may sit at either position B or C (Figure 2.2b). Thus the stacking sequence of the close-packed primary polar plane (0001) for wurtzite is ABABAB; while the stacking sequence of the close-packed primary polar plane (111) for zincblende is ABCABC. As a result, the zincblende polytype is related to the wurtzite polytype by rotations and translations within the unit cell.

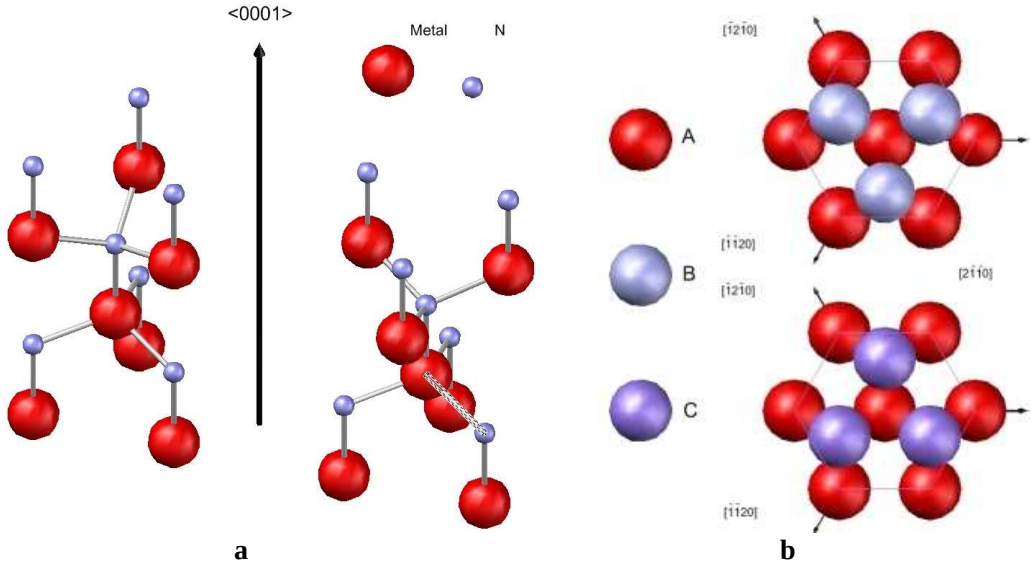

Figure 2.2 Possible atom stacking orientations in close packed structure
a: Comparison of bonds between close packed planes for the wurtzite (l) and zinc blende (r) structures; b: Possible stacking orientations of atoms in a close packed hexagonal structure.

The planes terminating with either all group III atoms or all nitrogen atoms are called polar crystal planes. All of the above three structures contain polar planes. In cubic crystal structures, group III (Al Ga or In) terminated planes are denoted as (111) or (111) A and group V terminated planes are denoted as (-1-1-1) or (111)B. In the wurtzite structure, the atoms along the <0001> direction are arranged in bilayers consisting of two closely spaced hexagonal layers, one with Al atoms and the other with nitrogen atoms. Therefore, the AlN basal surface can be either Al- face or N- face and the (0001) and (000-1) surfaces of AlN are inequivalent (Figure 2.3). By convention, the

crystallographic [0001] axis points from the N-face to the Al-face. The terms Al-face and N-face referred to the orientation of the AlN lattice, and describe lattices related to each other by an inversion operation. The Al-face and N-face polarities are also referred to as +c and –c polar, respectively. Here, Al-face / N-face is different from Al-terminated / N-terminated. Termination should only be used to describe a surface property[18]. Both an Al-face and a N-face orientation might be either Al-terminated or N-terminated; as a result, AlN possesses different properties along different <0001> polar directions. Both bulk and surface properties can vary significantly depending on whether the surface is nitrogen or metal face[18]. An extended defect consisting of a region of material with a polarity opposite to the polarity of the surrounding crystal matrix is known as inversion domain.

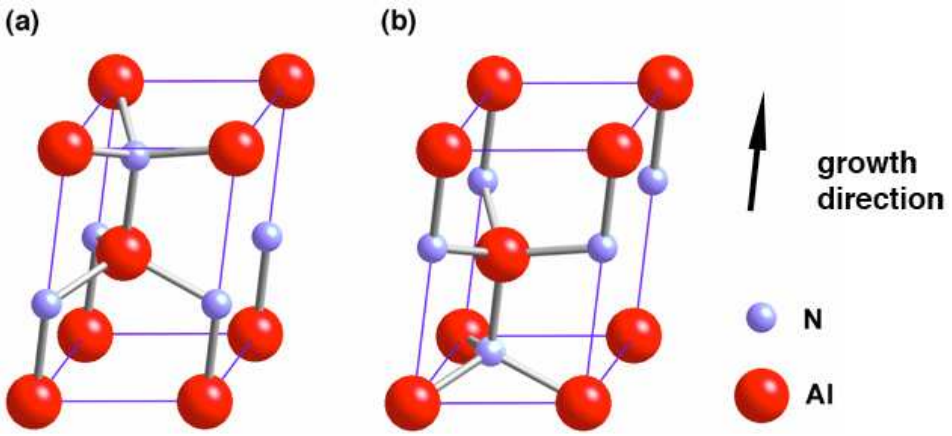

Figure 2.3 AlN primitive unit cell indicating (a) Al-polar and (b) N-polar structures.

2.1.2 Crystal Structure of SiC

The crystallography and polymorphs in silicon carbide play important roles in controlling the nature of the surfaces available for the epitaxial growth of III-nitride semiconductors. The basic unit of SiC is a covalently bonded tetrahedron of Si atoms with a C at its center or vice versa, i.e. either CSi_4 or SiC_4[21]. The bonding of silicon and carbon atoms is 88% covalent and 12% ionic, with a distance between the Si and C atoms

of 1.89 Å[22]. The shortest distance between the nearest Si atoms is approximately 3.08 Å. SiC exists in more than 250 polytypes – one-dimensional variations of the stacking sequence of close packed biatomic planes[23]. The various polytypes are distinguished by the stacking order between the succeeding double layers of carbon and silicon atoms. The stacking of the bilayers follows one of three possible relative positions which have already been shown in Figure 2.2. Other than wurtzite and zincblende, the other polytype structures in silicon carbide may be a combination of these two. There are two common ways to describe the crystal structures in the silicon carbide system, as proposed separately by Jagodzinski[24,25] and Ramsdell[26]

In Jagodzinski's method[24,25], each layer is described as having either a local cubic (k) or hexagonal (h) structure, based on the position of the center atom or centroid of the immediate layer neighbors. If the positions of the centroid in the layers above and below are different, the structure is described as cubic. For example, ABCABC stacking sequence describes a cubic bilayer structure. If the centroid of the two layers above and below is in the same spatial position, then the layer is described as hexagonal, such as each bilayer in the ABABA stacking sequence. Therefore two stacking sequences exist in this method: sequences with layer transitions only, which is denoted by "kkkk", and sequences with layer transitions and rotations denoted by "hhhh". For instance, (hkk)2 and hkhk describes a unit cell with six bilayers (6H) and 4 bilayers (4H) respectively.

The second method was proposed by Ramsdell[26] and is based on hexagonal symmetry consisting of a number followed by a letter. The number is used to describe how many double layers are there in the stacking sequence before the sequence is repeated. The letter represents the crystal symmetry (hexagonal (H), cubic (C),

rhombohedral (R)). In the silicon carbide system there are five small period polytypes which occur most often within the crystal structures and may be considered the 'basic' structures: 2H, 3C, 4H, 6H, and15R. Each of the longer period polytypes may be considered as a combination of these five short period polytypes. This latter notation will be utilized in the remainder of the dissertation. By observing the SiC crystal perpendicular to the c-axis, the stacking sequence of 2H, 3C, 4H, 6H- SiC can be projected[21] as shown in Figure 2.4. The height of the unit cell, c, varies with the different polytypes hence the ratio c/a also differs from polytype to polytype. The measured c/a ratios are approximately 1.641, 3.271 and 4.098 for the 2H-, 4H- and 6H-SiC polytypes, respectively, very close to the ideal values (3/8, 23/8 and 33/8)[21]. The frequently mentioned planes and directions in hexagonal SiC is shown in Figure 2.5, they are also work for other hexagonal structures.

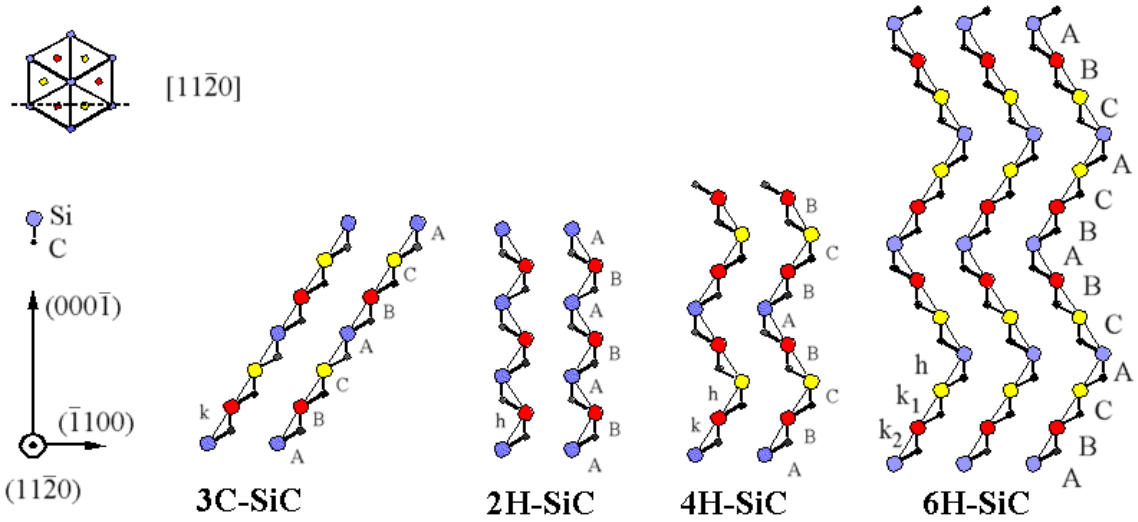

Figure 2.4 Stacking sequence for 4 main polytypes of silicon carbide

2.1.3 Crystal Structure of Related Transition Metal Nitrides

As the crystal growth and characterization of TiN and YN was invested in this study, the basic structures and composition for their nitrides group is reviewed here. By

convention, the term nitride is only applied to those compounds that nitrogen forms with elements of lower or about equal electronegativity. [27] According to the nitrides classification based on their electronic structure and bonding characteristics,[28] there are five general categories. Transition metal nitrides in Group IVB and group VB including TiN, ZrN and VN are interstitial nitrides; while group IIIB nitrides (ScN and YN) are saltlike nitrides. Because of the large difference in electronegativity and atomic size between nitrogen and the metal in the interstitial, the nitrogen atom nests readily in the interstices of the metal lattice. And their bonding is mostly metallic with some covalent and ionic bond components, giving those metallic characteristics such as high electrical and thermal conductivities. [29] For saltlike nitrides, atomic bonding is ionic as the difference in electronegativity between other elements and nitrogen is large. Although some of these nitrides have high melting points, they are sensitive to hydrolysis and react readily with water or moisture to give ammonia and the corresponding metal oxide or hydroxide[29], for example YN[30]. Table 2.2 is the crystal structure for transition metal nitrides and their host metal and Table 2.3 is the lattice constants and molar mass for AlN, SiC and related nitrides.

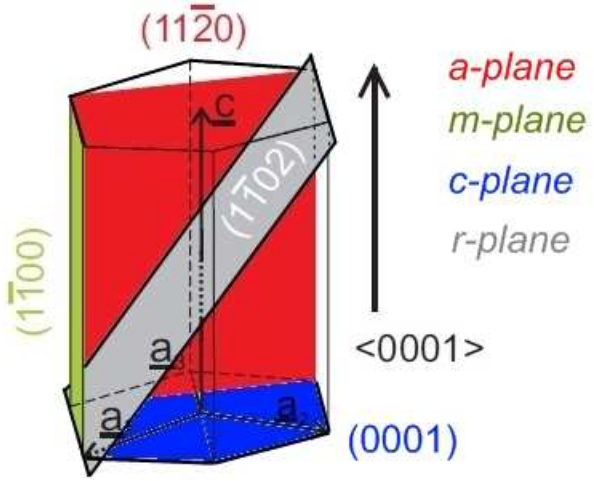

Figure 2.5 Common planes and directions in hexagonal structure

Table 2.2 Crystal structure for transition metal nitrides and their host metal

Host Metal	Sc	Y	Ti	Zr	Hf	V	Nb	Ta
Crystal struture	hcp	hcp	α: hcp β: bcc	α: hcp β: bcc	α: hcp β: bcc	bcc	bcc	bcc
Nitrides structure	fcc	fcc	fcc	fcc	fcc	hcp (M_2N) fcc(MN)	hcp (M_2N) fcc (MN)	hcp (M_2N) fcc (MN)

Note: α is the low temperature form, β is high temperature form

Table 2.3 Lattice constants and molar mass for AlN and related nitrides

	Molar mass g/mol	Lattice Constant Wurtzite		Lattice Constant **a** (Å) Zincblende	Lattice Constant **a** (Å) Rocksalt
		a (Å)	**c** (Å)		
AlN	40.9883	3.112[18]	4.982 [18]	4.38 [20]	4.04 [20]
GaN	83.7298	3.189[18]	5.185 [18]	4.49~4.55 [20]	4.098 [20]
InN	128.8250	3.54[18]	5.705 [18]	4.98-5.17	-
SiC	40.0962	4H: 3.0730[22] 6H: 3.0806[22]	4H: 10.053[22] 6H:15.1173[22]	3C: 4.3596[22]	-
TiN	61.8738	-		-	4.24
ZrN	105.2309	-		-	4.567
ScN	58.9626	-		-	4.50
YN	102.9126	-		-	4.88

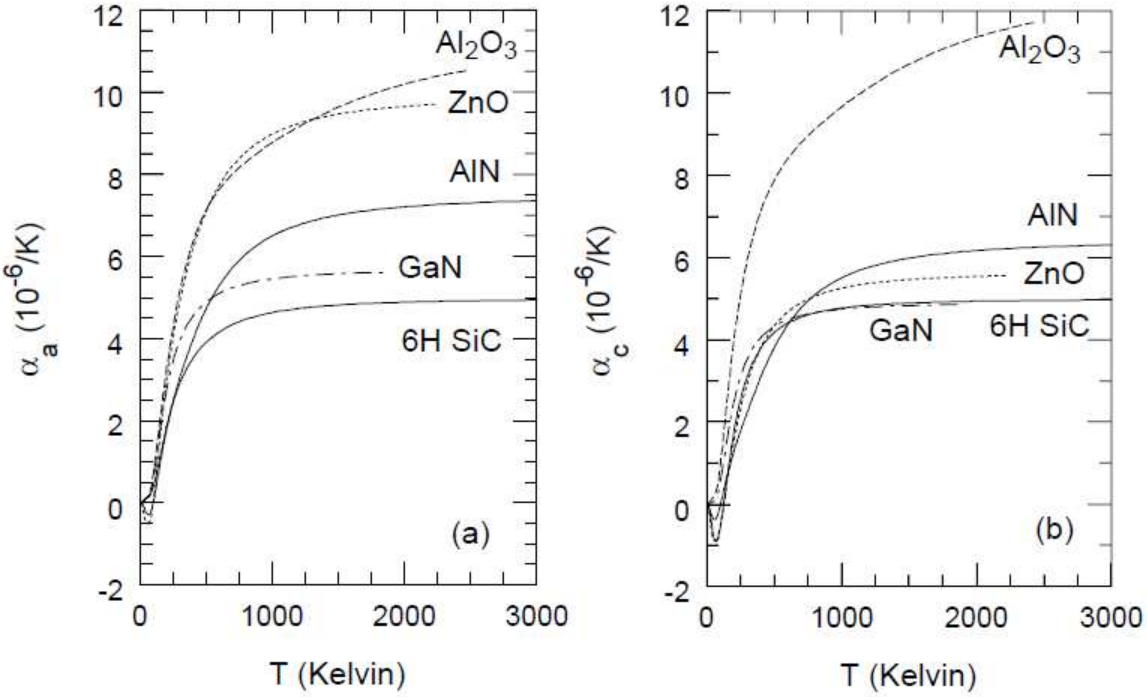

Figure 2.6 Thermal expansion of GaN, AlN, Al_2O_3, 6H-SiC, and ZnO*
***Published figure by R. R. Reeber and K. Wang [37] (a) a-axis; (b) c-axis.**

2.2 Material Properties

The properties of materials are determined in part by their structure. The anisotropic of crystalline lattice AlN is reflected in its properties. For example, the thermal expansion of AlN is anisotropic due to the direction-specific nature of the wurtzite bonding, therefore the coefficients of thermal expansion are different in the **a** and **c** directions. The wurtzite structure has the highest symmetry compatible with the existence of spontaneous polarization[31,32,33] and the piezoelectric tensor of wurtzite has three non-vanishing independent components. Thus the polarization in AlN has both a spontaneous and a piezoelectric component.

2.2.1 Thermal Properties and Mechanical Properties

Because of the anisotropic thermal expansion perpendicular and parallel to c axis in hexagonal materials, the c/a ratio becomes smaller with increasing temperature. The thermal expansion of AlN has been determined experimentally[20, 34 , 35] over a broad temperature range (77-1623 K) and has been predicted over a broader temperature range (25–2000K) using a semi-empirical multi-frequency Einstein model.[36,37] Figure 2.6 is the calculated thermal expansion of GaN, AlN, Al_2O_3, 6H-SiC, and ZnO.[37]

Its high melting temperature and high thermal conductivity are the important beneficial properties of AlN for substrate applications. The melting temperature for AlN is 3023 K between 100 and 500 atm of nitrogen .[38] Although the theoretically estimated value at room temperature was 3.2 W/cm K[20], the measured thermal conductivity for single crystal AlN varied from 2.5 to 3.4 W/cm K[20, 39, 40, 41]. Differences in the purity and density of the AlN account for the large variations in thermal conductivity. Oxygen impurities in particular degrade the thermal conductivity. Oxygen enters the nitrogen

sublattice substituting on nitrogen sites[39]; simultaneously, aluminum vacancies are created for charge compensation. For every three oxygen atoms incorporated on nitrogen sites one aluminum vacancy is created. The resulting Al vacancies cause a reduction in lattice constants. These defects and impurities scatter phonons, which are the heat carriers in AlN thus reducing the thermal conductivity. Hence, to achieve the maximum thermal conductivity, the oxygen concentration in AlN must be as low as possible.

Several researchers have reported on the mechanical properties of AlN. Different methods have been applied to determine the single crystal elastic constant matrix for AlN[20]. Gerlich and co-workers reported Young's modulus of 308 GPa and bulk modulus of 160 GPa from sound velocity measurement[42], while another study[43] measured Young's modulus and Poisson's ratio to be 329.7 GPa and 0.239 respectively. In Goldberg's book[44], the bulk modulus was reported to be 210 GPa. With Knoop diamond indenter, the hardness of AlN was obtained to be -12 GPa on the basal plane (0001).

2.2.2 Electronic and optical properties

In order to determine the electrical and transport properties, intentionally doped materials of high crystal quality are necessary for Hall measurements. This is difficult for AlN due to the large ionization energies of most dopants. The unintentionally doped single crystals have been reported to have high resistivity in the range of 10^7-10^{13} Ωcm[20]. And the relative dielectric constant of AlN was reported to be as high as 8.5[45]. These reasons make it difficult to test the electrical properties of AlN.

AlN has a direct energy band gap at the center (Γ point) of the Brillouin zone (BZ). Figure 2.7 is the schematic diagram for the band structure of wurtzite AlN based on Christensen and Gorczyca's research[46]. AlN conduction band has a single minimum (Γ_{7c})

at BZ Γ point, while the valence band is split at the Γ point by the crystal field and the spin-orbit interaction. The band gap for wurtzite AlN is generally over 6 eV as measured various methods including optical absorption[47, 48], ellipsometry[49], cathodoluminescence[50] , photoluminescence[51, 52], and the commonly quoted value at room temperature is 6.2 eV. However, measurements of the band gap for zincblende AlN are lacking.

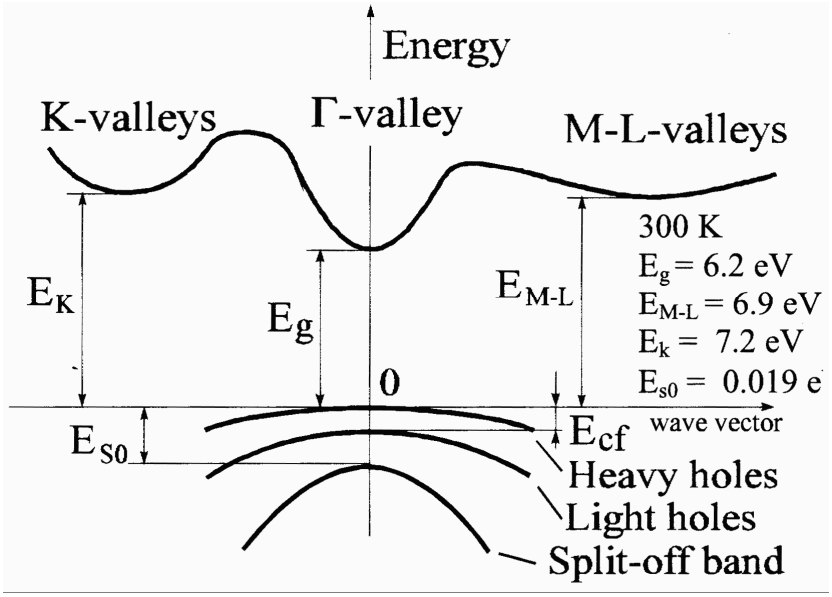

Figure 2.7 Band structure of wurtzite AlN*

***Published figure by N. E. Christensen, I.Gorczyca [46].**

The fundamental band gap energy of unstrained AlN was reported to be 6.096 eV at 1.7 K[53], while the crystal field splitting parameter was –230 meV and the exciton energies were 6.025, 6.243, and 6.257 eV for the A, B, and C excitons, respectively. The A transition is allowed for light polarized parallel to the c-axis. This may explain why earlier absorption measurements consistently resulted in larger values for the band gap; these measurements were typically performed with light polarized perpendicular to the c-axis, and likely probed the B or C transitions. These results imply that (0001)-oriented devices grown with AlN or high Al content AlGaN alloys will be better edge emitters than surface emitters[53].

Raman spectroscopy provides information on the vibrational states of GaN, AlGaN and AlN that are sensitive to the crystalline quality, the stress, the free carrier concentration, the aluminium composition and the temperature, and therefore can be employed for process and crystal growth monitoring. Because of the wurtzite structure, AlN has eight sets of phonon modes: $2E_2$, $2A_1$, $2E_1$ and $2B_1$, of which both E_2 sets, one A_1 set and one E_1 set are Raman active and the B_1 modes are silent[54]. By comparing the phonon modes of crystal sample, information on crystal properties and quality can be obtained. For instance, the width of the E_2 Raman peak reflects the crystalline quality and stress affects the E_2 phonon frequency[54]. Information on the free carrier concentration can also be obtained as collective excitations of free carriers (plasmons) interact with the A_1(LO) longitudinal optical phonons, but not with the non-polar E_2 phonons, which are only affected by stress and the crystalline quality[54]. The change of aluminum composition x in $Al_xGa_{1-x}N$ layers can affect both the E_2 and the A_1(LO) phonon frequency, therefore the composition information can be collected from Raman modes[54].

Raman spectra of optical phonons in AlN were taken in backscattering geometry on different well-developed facets of a self-seeded bulk crystal[55], and the dependence of phonon spectra on crystal orientation was reported. The results indicated that facets belonging to the same crystal class showed similar Raman spectra, while the appearance or absence of the A1(LO), A1(TO), E1(LO), and E1(TO) phonon bands in the spectra could be used to distinguish the basal *c*-plane facets from the prismatic {10-10} facets Besides E2 modes, *C*-plane facets showed A1 (LO) and E1 (TO) bands, while prismatic facets showed the A1 (TO), E1 (LO) and E1 (TO) bands.

2.3 History and Application of AlN

2.3.1 History

The earliest report of AlN crystal production is probably the study of Fichter and Oesterheld in 1915[56]. They heated AlN powder in the one atmosphere nitrogen ambient in an electrically heated furnace consisting of graphite or tungsten tubes to obtain AlN crystals. Metallic Al and AlN crystals were found in the recondensed materials, and the graphite apparatus also introduce carbon to the material.

It was not until 1960's that the reports of bulk AlN single crystal growth started increasing. Vapor transport in nitrogen by sublimation of AlN powder[57, 58, 59, 60] or vaporization of Al metal were most common methods[57, 61, 62]. The crystal morphology varied with the temperature. Taylor and Lenie[57] reported various crystal morphology at different growth temperature, including whiskers between 1450°–1750°C, prismatic needles between 1800 – 1900°C, and thin platelets at temperatures above 1900°C. Drum and Mitchell[59] observed whiskers at source temperature below 1900°C, and a mixture of basal platelets and whiskers at source temperatures range of 1950°–2150°C. The size and color of the AlN crystals varied. Taylor and Lenie[57] got prismatic needles 0.5 mm in diameter and up to 30 mm long. Davies and Evans[60] obtained whiskers 18–20 mm long with an average growth rate of 1.5 mm/h. Crystals were colorless[61,62] or varied in color from white[57], to various shades of blue[57,62] and brown[62].

Taylor and Lenie[57] claimed that blue coloration was due to the presence of aluminum oxycarbide (Al_2OC), which is isomorphous with AlN. They proposed that a solid solution formed between AlN and Al_2OC from a reaction between Al and the carbon monoxide (CO) expected to be present in furnaces lined with graphite. Crystals

were grown in controlled atmospheres of pure nitrogen, nitrogen with 0.5–2% carbon monoxide, and nitrogen with 1% methane. Blue crystals were grown only in the presence of CO, and a deeper shade of blue was observed with increasing amount of CO in nitrogen. Chemical analysis confirmed the presence of C and O in the crystals[57].

2.3.2 Application

Group III-nitrides and their alloys are good candidates for optoelectronic devices because they form a continuous alloy system whose direct optical band gaps in the wurtzite phase range from 0.7 eV for InN to 6.1 eV for AlN, potentially allowing band gap engineering in a wide wavelength range from infrared (~1770 nm) to deep ultraviolet (~200 nm). Their high thermal and chemical stability, breakdown electric fields, and maximum electron velocities are advantageous for application areas such as high-power, high frequency, and high-temperature devices where classical semiconductors, such as silicon, and the conventional III-Vs (e.g. GaAs, AlAs, AlP) have fundamental limitations. In addition, the piezoelectric properties of AlN make it highly suitable for surface acoustic wave devices.

Presently, epitaxial heterostructures involving these semiconductors are being grown on a number of substrates. The two most commonly used substrates, sapphire and SiC, are not closely lattice-matched to the III-nitride overlayers, leading to a high defect density in the overgrown active layers, limiting device performance and lifetime. Additional limitations of the currently available substrates include device layers cracking due to the large thermal mismatch, and poor thermal conductivity. Thus, the performance of III-nitride semiconductor devices will be greatly improved by the availability of native substrates. High-quality, single crystalline AlN substrates with low dislocation densities

are expected to decrease defect density in the overgrown device structures by several orders of magnitude and, thereby, greatly improve the performance and lifetime of III-nitride devices.

AlN has a number of excellent properties that make it a highly desirable candidate as a substrate for III-nitride epitaxy. Its crystalline structure is the same as that of GaN, with a lattice mismatch in the c-plane of approximately 2.5% (Table 2.3 Lattice constants and molar mass for AlN and related nitridesTable 2.3). Since AlN makes a continuous range of solid solutions with GaN, it plays an important role in GaN-based devices and is highly suited as a substrate for AlGaN devices with high Al concentrations or structures with graded layers. Its high thermal conductivity makes it desirable for high-temperature electronic and high power microwave devices where heat dissipation is critical. Its high resistivity us important for power microwave devices. The direct, large optical bandgap of AlN makes it suitable for ultraviolet applications such as light-emitting diodes and laser diodes down to wavelengths as short as 200 nm.

2.4 Crystal Growth

III- nitrides films and crystals have been fabricated by many different methods on different substrates, such as vapor phase epitaxy including hydride vapor phase epitaxy (HVPE), molecular beam epitaxy (MBE) including plasma-induced molecular beam epitaxy (PIMBE), metal organic vapor phase epitaxy (MOVPE), metal organic chemical vapor deposition(MOCVD), pulse laser deposition (PLD), supersonic molecular beams, reactive sputtering, and high-temperature/ high pressure growth, including physical vapor transport (PVT, for AlN) and liquid solution growth (high-pressure solution, ammonothermal, and Na flux method for GaN). The growth of large-size and high-

quality AlN and GaN crystals for substrates is still in its infancy. The production of high quality crystalline materials with improved structural perfection and large size at a low cost (1) and bulk crystal growth of materials with extreme thermodynamic characteristics, such as high temperature melting points, high melting dissociation pressures, incongruent phase diagrams, and anisotropic segregation (2) are the two main challenges of today's crystal growth[63]. In this part of dissertation, the focus is on the bulk sublimation crystal growth of AlN and related nitrides.

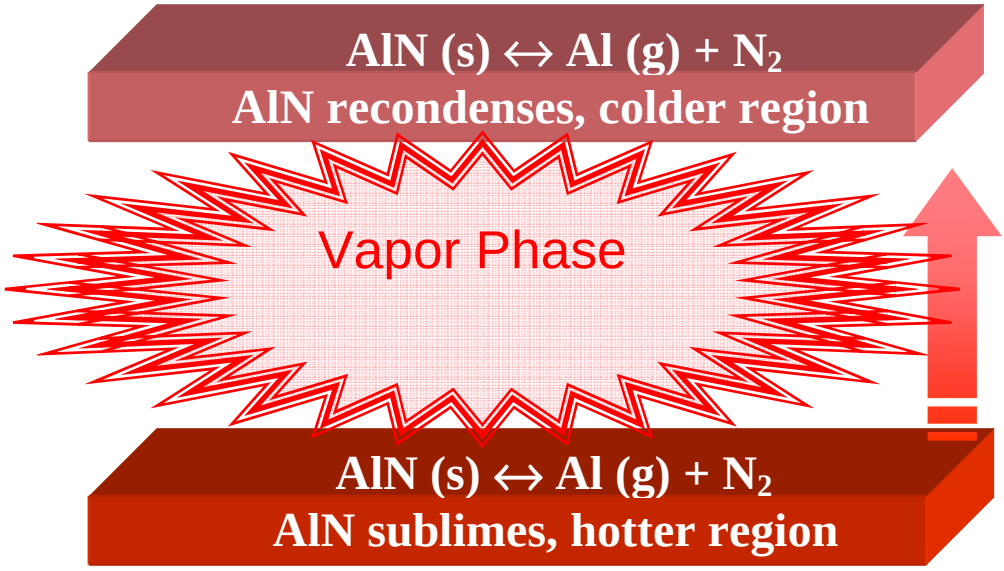

Figure 2.8 Physical vapor transport

2.4.1 Physical Vapor Transport

The majority of commercialized semiconductor bulk crystals are grown using melt growth methods such as Czochralski (CZ), float-zone (FZ), and vertical Bridgman growth. However, the melt growth is precluded if the melting point temperature is too high, or if the melt decomposes, or the melt reacts with the crucible. Physical vapor transport (PVT) growth techniques, provides an alternative crystal growth method and is the most successful bulk crystal growth method for aluminum nitride to date.

The process (Figure 2.8) starts with the source sublimation at a temperature below the melting point. A temperature gradient is maintained between the high temperature source sublimation zone and relatively low temperature crystal recondensation zone. Then the source substance is transported to the lower temperature zone through the gas phase and recrystallizes there. The process takes place in a closed or semi-open system (crucible). It is called seeded growth if a selected substrate or seed crystal is applied for the source to crystallize on, or self-seeded growth if the nucleation occurs spontaneously at crucible walls.

Sublimation crystal growth can be modeled by considering the following phenomena. The temperature gradient provides the driving force of the crystal growth. At the temperatures below its triple point, a pure solid can sublime, and equilibrium pressure for a particular temperature is called the solid/ vapor saturation pressure p^{sat}. Consider the system to be initially in a non equilibrium state with respect to mass transfer between phases and possible reactions. Then any changes which occur in the system take the system ever closer to an equilibrium state. If the chemical potential of each species in all phases are equal, the system reaches its phase and chemical equilibrium. At the source zone (highest temperature), the chemical potential difference between the vapor and solid phase drive the mass transport from solid phase to vapor phase; while at the crystal zone (lowest temperature), the reverse process results in crystallization.

The driving force of the crystallization or growth affinity can be defined as chemical potential difference: $\Delta\mu = \mu_v - \mu_s$; where μ_v and μ_s are the chemical potentials of the vapor and solid, respectively. Crystallization occurs when the vapor pressure p of the gaseous species at the vapor-crystal interface is higher than p^{sat}, which is a function of

temperature. The degree of supersaturation can be defined as $\sigma = (p - p^{sat}) / p^{sat}$ If the vapor is ideal gas, the chemical potential difference can be expressed in terms of local vapor pressure p and saturation pressure p^{sat}:

$$\Delta\mu = kT \ln(p / p^{sat}) \quad \textbf{(2-5)}$$

where k is Boltzmann's constant(1.38 x 10^{-23} J/K) and T is the temperature of the solid.

According to the kinetics gas theory, one can estimate the maximum growth rate through Hertz-Knudsen equation. It is shown that the incident flux, F , is related to the gas density above the surface by

$$F = nc / 4 \quad \textbf{(2-6)}$$

where n is molecular gas density (molecules/m^3) and average molecular speed c (m/s) is given from the Maxwell-Boltzmann distribution of gas velocities by integration:

$$c = \sqrt{8kT / m\pi} \quad \textbf{(2-7)}$$

where m is molecular mass (kg). Consider the vapor as ideal gas [$n = N / V = P / (kT)$], then the net vapor flux J to the surface based on Hertz-Knudsen equation is:

$$J = \alpha F = \frac{\alpha P}{\sqrt{2\pi mkT}} \quad \textbf{(2-8)}$$

where α is the sticking coefficient, defined as the probability that an impinging vapor particle is adsorbed onto the surface. Neglecting the effects of gas phase diffusion between source and crystal and assuming that the sticking coefficient is one, the maximum growth rate V from the equilibrium vapor pressures over the source (p) and seed (p^{sat}) can be estimated as following:

$$r^{\max} = \frac{V_a (p - p^{sat})}{\sqrt{2\pi mkT}} \quad \textbf{(2-9)}$$

where V_a is the atomic volume. Obviously, the maximum growth rate estimated above is proportional to the vapor supersaturation. Another prerequisite of this estimation is that

the crystal surface is rough or there are enough kink sites (kink sites are special surface positions whose chemical potential is equal to that of the bulk crystal; they are favorable incorporation sites for adatoms and help determine the equilibrium with the vapor phase) on the surface, therefore there are sufficient sites available on the crystal surface for incorporation of adsorbed atoms.

If the substrate/surface reaction process is the growth rate limiting step, for example at a high gas species flow rate, one should also considered the process of: a) adsorption, dissociation and desorption at growth surface; b) mobility of the species (possible reactants and products) on the surface; c) incorporation at the lattice sites. These are critically dependent upon the physical and chemical state of the growth surface. Burton, Cabrera, and Frank[64] developed an analytical model for crystal growth by step propagation in terms of steady- state motion of an equidistant train of flat steps across a crystal surface. The BCF theory explains the equilibrium structure of crystal surfaces, the step velocity on crystal surfaces, and the growth rate of crystal surfaces. The ledge and kink density, ie surface roughness, of a particular crystal plane depends upon the inter-atomic bonding forces between surface atoms and their neighbors. The mechanism for step movement was the deposition of atoms onto the terraces and subsequent capture and in corporation of the diffusing atoms at the step edge. Based on the theory assumption, an analytical solution for step velocity and growth rate can be obtained.

The BCF theory assumes there is a flux of atoms from the vapor phase impinging on the surface during the growth process. Atoms become adsorbed and these adatoms can execute jumps to adjacent surface sites or back to the vapor phase. Defining the average amount of time an adatom spends on an infinite flat surface before desorbing back to the

gas phase as τ and the diffusion coefficient as D, the average distance x that the as atoms diffuse during the life time τ can be calculated by Einstein formula:

$$x_{diff}{}^{2} = D_{diff}\tau \qquad \textbf{(2-10)}$$

Where $D_{diff} = a^2\upsilon'\exp(-E_{diff}/kT)$ and $\tau = \upsilon^{-1}\exp(E_a/kT)$, a is the lattice constant, ν and ν' are frequency factors on the order of the atomic frequency of vibration (~10^{13} s^{-1}), and E_{diff} and E_a are the activation energies for surface diffusion and desorption. Once the adatoms attach at a kink, the kink moves forward one step. The growth rate can be obtained by indentifying the forward speed of the step (step velocity).

The near steps adatom surface concentration n_e and the far from steps adatom surface concentration satisfy $(n-n_e)/n_e = \sigma = (p-p^{sat})/p^{sat}$. Thus the velocity of a single step on surface is

$$V_{\infty} = 2\sigma\theta_e D_{diff}/x_{diff} \qquad \textbf{(2-11)}$$

Where θ_e is equilibrium surface coverage, it is denoted as n_e divided by total surface site concentration n_t[65]. If the average spacing between steps is l and the step height is h, the velocity of a parallel train of steps and vertical growth rate are given by

$$V_{BCF} = V_{\infty}\tanh(l/2x_{diff}) \qquad \textbf{(2-12)}$$

$$r_{BCF} = V_{BCF}(h/l) \qquad \textbf{(2-13)}$$

Therefore, in the steady state, all steps move at the same velocity, and both the step velocity and vertical growth rate is proportional to the supersaturation.

2.4.2 Bulk Crystal Growth of AlN by PVT

Bulk AlN crystal growth can be obtained at a temperature as low as 1800 °C, but temperature higher than 2200 °C are required to achieve commercially viable growth rates of 500 μm/ hour with good crystal quality[66]. Such a high operation temperature is

quite demanding on the furnace design and materials of construction. Besides the requirement of high durability at a high temperature, the selected material has to be inert to chemically aggressive Al vapor, a negligible source of contamination to the growth process, reusable for multiple growths, relatively inexpensive, and manufacturable in various shapes and dimensions. Studies suggest that graphite and boron-containing crucibles should be avoided[66], while tungsten [67] and sintered TaC [68] crucibles offer acceptable performance.

In practice, at such high growth temperatures, the experimental growth rate can be thousands of times less than the maximum, predicted from thermodynamics, i.e. the equilibrium pressure difference between the source and seed. The vapor transport mechanisms in AlN sublimation was investigated at different conditions.[69, 70] At high pressure (760 Torr), vapor transport was controlled by diffusion in the gas phase, while at low pressure (10^{-4} Torr), it was dominated by drift of the reactive species, Al and N_2. A 2-dimensional[71, 72] model and a 1-dimensional [73] model have been established for vapor phase transport, the 2D model can reveal more important information than the 1D model, such as recirculation and radial components distribution. Considering the case of no adsorption or nucleation barriers at the source and seed interfaces, a detailed two dimensional model accommodating the thermal convection and Stefan flow was formulated for AlN sublimation growth by Edgar's group[71, 72]. The dependence of growth rate distribution on various process parameters was studied experimentally and explained by modeling calculation. The growth rate was related to the process parameters such as pressure, temperature, temperature gradient, and distance between source and seed:

$$r = k\frac{\exp(\Delta S/R - \Delta H/RT)}{P^{1.5}T^{1.2}}\frac{\Delta T}{\delta} = k\frac{\exp(A - B/T)}{P^{1.5}T^{1.2}}\frac{\Delta T}{\delta} \qquad \textbf{(2-14)}$$

where the k, A and B are constants, the temperature gradient $\Delta T / \delta$ is obtained from temperature difference ΔT and source-seed distance δ. The $T^{1.2}$ has a more profound effect than the exponential factor and the growth rate is proportional to $P^{-1.5}$ and temperature gradient. The activation energy for AlN growth was 681 kJ/mol, which is close to the heat of sublimation of AlN, 630 kJ/mol.

The process was defined as self-seeded growth if no crystal seeds/substrates were provides and the nuclei formed on the crucible lid during the early stage of the growth. Then the growth competitions between different nuclei resulted in single crystal regions of varying sizes and orientations. This growth process has been invested by several groups[74, 75, 76, 77], with shapes changing from long needles to well-faces crystals. A crystal boule up to 15 mm in diameter and several cm in length was achieved[75]. Epelbaum and coworkers studied the natural growth habit of AlN bulk crystals at temperature range of 2050–2250°C with a small temperature gradient of 3–5°C/cm[78]. The morphology and color of the crystals changed as the temperature was increased, from nearly transparent six-sided prismatic needles, to columnar crystals, and to thick platelets. The color of the crystals also varied from transparent to dark amber or brownish as the temperature increased.

SiC is most commonly used for substrate of AlN growth due to the availability of high quality SiC single crystal wafers and the lack of commercial AlN single crystal wafers. The small lattice mismatch with AlN, which is about 1% for 6H-SiC and 1.2% for 4H-SiC of the ***a*** lattice constant (Table 2.3), and the ability to control the polarity and orientation of AlN crystals are additional advantages of SiC seeds. A series of extensive studies were reported from Dr. Edgar's group[79, 80, 81, 82,83].The growth temperature was

typically 1800°C. SiC wafers (both on-axis and off-axis) with silicon and carbon terminations were used as substrates. Continuous thick layers of AlN on SiC were achieved by first using an AlN buffer layer that was deposited by MOCVD, although cracks formed during cool down due to stress resulting from the thermal expansion coefficient mismatch[79]. Without the buffer layer, AlN nucleated as individual hexagonal hillocks and platelets in an island-like growth mode[80]. AFM images revealed scratches and steps on as-received 6H-SiC substrates, which served as nucleation sites for individual AlN grains grown[81]. Another procedure introduced an AlNSiC alloy interlayer to reduce the cracking of the AlN bulk layer[82]. It was predicted[83] that AlN grown on 6H-SiC should be at least 2 mm thick in order to avoid cracking during cool down from a growth temperature of 2000°C. Thus the stability of the SiC seeds and the cracking of the AlN layers due to the high process temperature involved and the difference in thermal expansion between AlN and SiC and are still important issues need to be addressed for this process.

Seeded growth on recently available AlN native seeds eliminates many of the problems associated with heteroepitaxial growth. Schlesser *et al*[84] produced transparent, single-crystal *c*-platelets prepared by vaporization of Al in N_2 using AlN seeds. The growth temperature was 2200°C with a temperature gradient of about 3°C/mm, and X-ray rocking curves confirmed good single crystal quality. The growth rates on the two c-faces of opposite polarity differed by a factor of 2–3, with the Al polarity showing slower and smoother growth. By continuing growth of AlN on a previously prepared AlN seed, Noveski *et al*[85]produced a boule up to 1.5” in length and 1.25” in diameter. Centimeter-sized, single-crystal grains were observed in polished cross sections of boules and

epitaxial re-growth was demonstrated regardless of the orientation of individual grains. Herro *et al* [86] investigated AlN growth on seeds of differing polarities. They conclude growth along the <0001> polar directions was more stable on N-polar seeds, which was controlled by single growth center and leading to a mirror like growth facet. The growth on Al-polar seeds showed numerous growth centers leading to a deterioration of crystal quality, which suggested a lower supersaturation required for Al-polar direction. A comparison of seeded growth of AlN boules on *m*-(101-0) and *c*-(000-1) AlN seeds was reported recently by Lu et al[87] who found that the with a dislocation density in both crystals in the range 10^2–10^5cm^{-2}. The study showed that the impurity concentration varies with seed orientation[88]. The oxygen concentration in *m*-plane grown AlN crystals, 2 x 10^{18} cm^{-3}, was about 1/5 of that in *c*-plane grown crystals, whereas the carbon concentration in *m*-plane grown crystals, 2 x 10^{19} cm^{-3}, was twice of that in *c*-plane grown crystals.

2.5 References

[17] F. Briegleb and A. Geuther, *The Formation of Aluminum Nitride*, Ann. D. Chem. **123**, 228 (1862).

[18] O Ambacher, *Growth and applications of Group III-nitrides*, J. Phys. D: Appl. Phys. **31**, 2653–2710 (1998)

[19] W. D. Callister, Jr. Materials Science and Engineering: an introduction, 3rd edition, John Wiley & Sons, Inc., New York, 41, (1994).

[20] J. H. Edgar, Properties of Group III Nitrides, Institution of Engineering and Technology, (1994)

[21] Y. Shi, Z.Y. Xie, L. Liu, B. Liu, J.H. Edgar and M. Kuball, *Influence of Buffer Layer and 6H-SiC Polarity on the Nucleation of AlN Grown by the Sublimation Sandwich Technique*, J. Crystal Growth, **233**, 177 (2001)

[22] G.L. Harris, G.L. Harris (Ed.), Properties of Silicon Carbide, Inspec/IEE, **13**, 6 (1995)

[23] N.W. Jepps, T.F. Page, in: P. Krishna (Ed.), Progress in Crystal Growth and Characterization, Pergamon Press, New York, **7**, 259 (1983)

[24] N. W. Jepps and T. F. Page, P. Krishna (Ed.), Crystal Growth and Characterization of Polytype Structures, Vol. 7, Pergamon Press, Oxford, **7**, (1983)

[25] H. Jadodzinski, Acta. Crystallog. **2**, 201-207 (1949)

[26] L. S. Ramsdell, *Studies on Silicon Carbide*, Am. Mineralo- gist, **32**, 64- 82 (1947)

[27] F. A. Cotton, and G. Wilkinson, Advanced Inorganic Chemistry, Interscience Publishers, New York, (1972)

[28] F. Benesovsky, R. Kiefer, and P. Ettmayer, Nitrides in Kirk-Othmer's Encyclopedia of lndustrial Chemistry, 4th Ed., John Wiley & Sons (1993)

[29] H. O. Pierson, Handbook of Refractory Carbides and Nitrides, William Andrew Publishing/Noyes, (1996)

[30] L. Du, J.H. Edgar, R. A. Peascoe-Meisnerb, Y Gongc, S Bakalovac and Kuballc, *Sublimation Crystal Growth of Yttrium Nitride*, J. Cryst. Growth, **312**, 2896 (2010)

[31] F. Bernardini, V. Fiorentini and D.Vanderbilt, *Spontaneous Polarization and Piezoelectric Constants of III-V Nitrides*, Phys. Rev. B, **56,** R10024 (1997)

[32] J. F. Nye, Physical Properties of Crystals, Oxford University Press, Oxford, (1985)

[33] M. Posternak, A. Baldereschi, A. Catellani, and R. Resta, Phys. Rev. Lett. **64**, 1777 (1990)

[34] W.M. Yim, RJ. Paff J. Appl. Phys. **45**, 1456 (1974)

[35] G.A. Slack, S.F. Bartram, J. Appl. Phys. **46**, 89 (1975)

[36] Wang K and Reeber R R, Mater. Res. Soc. Symp. Proc. **482**, 863 (1998)

[37] R. R. Reeber and K. Wang, Mat. Res. Soc. Symp. Proc. **622**, T6.35 (2000).

[38] M.E. Levinshtein, S. L. Rumyantsev, M. S. Shur, Properties of Advanced Semiconductor Materials GaN, AlN, InN, BN, SiC, SiGe,John Wiley & Sons, Inc., New York, 31-47(2001)

[39] G.A. Slack, R.A. Tanzilli, R.O. Pohl, J.W. Vandersande, J. Phys. Chem. Solids, **48**, 641 (1987)

[40] G.A. Slack, T.F. McNeIIy, J. Cryst. Growth, **42** 560, (1977)

[41] J. C. Rojo, L. J. Schowalter, K. Morgan, D. I. Florescu, F. H. Pollack, B. Raghothamachar, M. Dudley, *Single-Crystal Aluminum Nitride Substrate Preparation from Bulk Crystals*, Mat. Res. Soc. Symp. Proc. **680**, E2.1 (2001)

[42] D. Gerlich, S.L. Dole, G.A. Slack, J. Phys. Chem. Solids, **47**, 437 (1986)

[43] K. Wang and R. R. Reeber, MRS Internet J. Nitride Semicond. Res., **4S1**, G3.18 (1999)

[44] CF. Cline, J.S. KaIm, J. Electrochem. Soc., 110, 773, (1963)

[45] J. H. Edgar, S.Strite, I. Akasaki, H. Amano, and C. Wetzel, Gallium Nitride and Related Semiconductors, INSPEC, London, (1999)

[46] N. E. Christensen, I.Gorczyca, *Optical and Structural Properties of III-V Nitrides under Pressure*. Phys. Rev. B **50**, 4397 (1994)

[47] G. A. Cox, D. O. Cummins, K. Kawabe, and R. H. Tredgold, J. Phys. Chem. Solids **28**, 543 (1967)

[48] G. A. Slack and T. F. McNelly, J. Cryst. Growth, **42**, 560 (1977)

[49] T. Wethkamp, K. Wilmers, C. Cobet, N. Esser, W. Richter, O. Ambacher, M. Stutzmann, and M. Cardona, Phys. Rev. B **59**, 1845 (1999)

[50] E. Silveira, J. A. Freitas, Jr., M. Kneissel, D. W. Treat, N. M. Johnson, G. A. Slack, and L. J. Schowalter, Appl. Phys. Lett. **84**, 3501 (2004)

[51] E. Kuokstis, J. Zhang, Q. Fareed, J. W. Yang, G. Simin, M. A. Khan, R. Gaska, M. Shur, C. Rojo, and L. Schowalter, Appl. Phys. Lett. **81**, 2755 (2002)

[52] J. Li, K. B. Nam, M. L. Nakarmi, J. Y. Lin, and H. X. Jiang, *Band Structure and Fundamental Optical Transitions in Wurtzite AlN*, Appl. Phys. Letters, **83,** N25 (2003)

[53] L. Chen, B. J. Skromme, R. F. Dalmau, R. Schlesser, Z. Sitar, C. Chen, W. Sun. J. Yang, M. A. Khan, M. L. Nakarmi, J. Y. Lin, H.-X. Jiang, *Band-edge exciton states in AlN single crystals and epitaxial layers*, Appl. Phys. Lett. **85**, 4334 (2004)

[54] M. Kuball, *Raman spectroscopy of GaN, AlGaN and AlN for process and growth monitoring/contro* , Surf. Interface Anal. **31**, 987 (2001)

[55] M. Bickermann, B. M. Epelbaum, P. Heimann, Z. G. Herro, A. Winnacker, *Orientation-dependent phonon observation in single-crystalline aluminum nitride*, Appl. Phys. Lett. **86**, 131904 (2005)

[56] F. Fichter and G. Oesterheld, Z. Electrochem. **21**, 50 (1915)

[57] K. M. Taylor and C. Lenie, J. Electrochem. Soc. **107**, 308 (1960)

[58] P. E. Evans and T. J. Davies, Nature **197**, 587 (1963)

[59] C. M. Drum and J. W. Mitchell, Appl. Phys. Lett. **4**, 164 (1964)

[60] T. J. Davies and P. E. Evans, Nature, **207**, 254 (1965)

[61] H. D. Witzke, Phys. Stat. Sol. **2**, 1109 (1962)

[62] C. M. Drum, J. Appl. Phys. **36**, 816 (1965)

[63] R. Fornari, M. Roth, *Recent Advances in Bulk crystal growth*, MRS bulletin **34**, 239 (2009)

[64] W. K. Burton, N. Cabrera, F. C. Frank, Phil. Trans. Roy. Soc. Ser. **A 243**, 299 (1951)

[65] R. Ghez and S. S. Iyer, IBM J. Res. Develop. **32**, 804 (1988)

[66] D.Enrentraut and Z. Sitar, *Advances in Bulk Crystal Growth of AlN and GaN*, MRS bulletin **34**, 259 (2009)

[67] B.Liu, J.H. Edgar, Z. Gu, D. Zhuang, B. Raghothamachar, M.Dudley, A.Sarua, M. Kuball, H.M. Meyer, MRS Internet J. Nitride Semicond. Res. **9,** 66 (2004)

[68] R. Schlesser, R Dalmau, D. Zhuang, R. Collazo, Z. Sitar, J.Cryst. Growth **281**, 75 (2005)

[69] S. Yu. Karpov, D. V. Zimina, Yu. N. Makarov, E. N. Mokhov, A. D. Roenkov, M. G. Ramm, Yu. A. Vodakov, *Sublimation Growth of AlN in Vacuum and in a Gas Atmosphere*, Phys. Stat. Sol. (a) **176**, 435 (1999)

[70] A. S. Segal, S. Yu. Karpov, Yu. N. Makarov, E. N. Mokhov, A. D. Roenkov, M. G. Ramm, Yu. A. Vodakov, *On mechanisms of sublimation growth of AlN bulk crystals*, J. Cryst. Growth **211** 68, (2000)

[71] L. Liu and J. H. Edgar, J. Cryst. Growth, 220, 243 (2000)

[72] L. Liu, J. H. Edgar: AG*global Growth Rate Model for Aluminum Nitride Sublimation*, J. Electrochem. Soc. **149**, G12 (2002)

[73] V. Noveski, R. Schlesser, S. Mahajan, S. Beaudoin, and Z. Sitar, J. Cryst. Growth **264**, 369 (2004)

[74] J. H. Edgar, L. Liu, B. Liu, D. Zhuang, J. Chaudhuri, M. Kuball, S. Rajasingam: *Bulk AlN Crystal Growth: self-seeding and seeding on 6H-SiC substrates*, J. Cryst. Growth **246**, 187 (2002)

[75] L. J. Schowalter, G. A. Slack, J. B. Whitlock, K. Morgan, S. B. Schujman, B. Raghothamachar, M. Dudley, K. R. Evans, *Fabrication of Native, Single-crystal AlN Substrates*, Phys. Stat. Sol. **0** 1997 (2003)

[76] M.Bickermann, B.M. Eprlbaum, A. Winnacker, Phys. Status Solid **C7**,1993 (2003)

[77] V. Noveski, R.Schlesser, B.Beaudoin, Z.Sitar, J. Crystal. Growth **279**, 13 (2005)

[78] B. M. Epelbaum, C. Seitz, A. Magerl, M. Bickermann, A. Winnacker, *Natural Growth Habit of Bulk AlN Crystals*, J. Cryst. Growth **265** 577 (2004)

[79] Y. Shi, Z. Y. Xie, L. H. Liu, B. Liu, J. H. Edgar, M. Kuball, *Influence of buffer layer and 6H-SiC substrate polarity on the nucleation of AlN grown by the sublimation sandwich technique,* J. Cryst. Growth **233** 177,(2001)

[80] B. Liu, Y. Shi, L. Liu, J. H. Edgar, D. N. Braski, *Surface morphology and composition characterization at the initial stages of AlN crystal growth*, Mat. Res. Soc. Symp. Proc. **639** G3.13.1, (2001)

[81] L. Liu, B. Liu, Y. Shi, J. H. Edgar, *Growth mode and defects in aluminum nitride sublimed on (0001) 6H-SiC substrates*, MRS Internet J. Nitride Semicond. Res. **6** 7.1 (2001)

[82] Y. Shi, B. Liu, L. Liu, J. H. Edgar, H. M. Meyer III, E. A. Payzant, L. R. Walker, N. D. Evans, J. G. Swadener, J. Chaudhuri , Joy Chaudhuri, *Initial nucleation study and new technique for sublimation growth of AlN on SiC substrate*, Phys. Stat. Sol. **188,** 757 (2001)

[83] L. Liu , B. Liu, J. H. Edgar, S. Rajasingam, M. Kuball, *Raman characterization and stress analysis of AlN grown on SiC by sublimation*, J. Appl. Phys. **92,** 5183 (2002)

[84] R. Schlesser, R. Dalmau, Z. Sitar, *Seeded growth of AlN bulk single crystals by sublimation*, J. Cryst. Growth 241 416-420 (2002)

[85] V. Noveski, R. Schlesser, B. Raghothamachar, M. Dudley, S. Mahajan, S. Beaudoin, Z. Sitar, *Seeded growth of bulk AlN crystals and grain evolution in polycrystalline boules*, J. Cryst. Growth **279** 13 (2005)

[86] Z. G. Herro, D. Zhuang, R. Schlesser, R. Collazo, Z. Sitar, *Seeded growth of AlN on N- and Al-polar <0001> AlN seeds by physical vapor transport*, J. Cryst. Growth **286** 205 (2006)

[87] P. Lu, R. Collazo, R.F. Dalmau, G. Durkaya, N. Dietz, B. Raghothamachar, M. Dudley, Z. *Sitar, Seeded growth of AlN bulk crystals in m- and c-orientation*, J. Cryst. Growth **312** 58 (2009)

[88] P. Lu, R. Collazo, R. F. Dalmau, G. Durkaya, N. Dietz, and Z. Sitar, *Different optical absorption edges in AlN bulk crystals grown in m- and c-orientations,* Appl. Phys. Lett. **93**, 131922 (2008)

CHAPTER 3 - Experimental

3.1 Equipment

The sublimation-recondensation technique was performed in a system comprised of a resistively-heated tungsten furnace with a growth chamber, a controller, and a vacuum system as the main components (Figure 3.1). The power output was controlled by the controller, which was also used to monitor, and/or control process parameters such as heater temperature, growth temperature, chamber cooling water temperature, chamber pressure and pump inlet pressure. The vacuum system include a mechanical pump, a diffusion pump and gas supply cylinders, which can provide base pressure to the chamber as low as 10 x 10^{-7} torr.

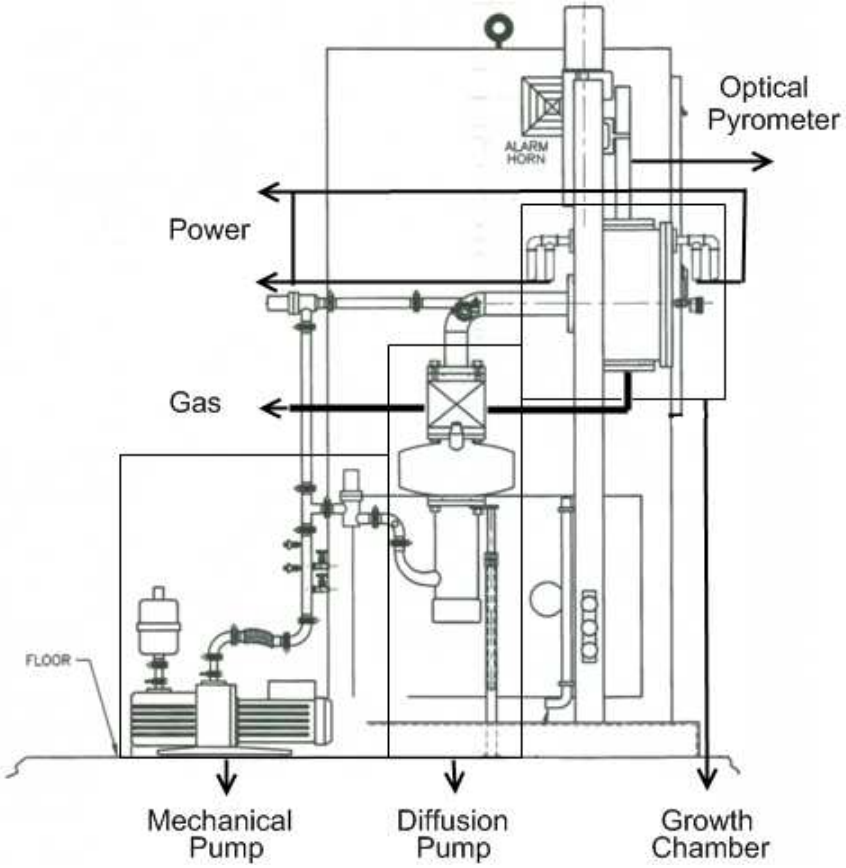

Figure 3.1 Schematic diagram of the furnace.

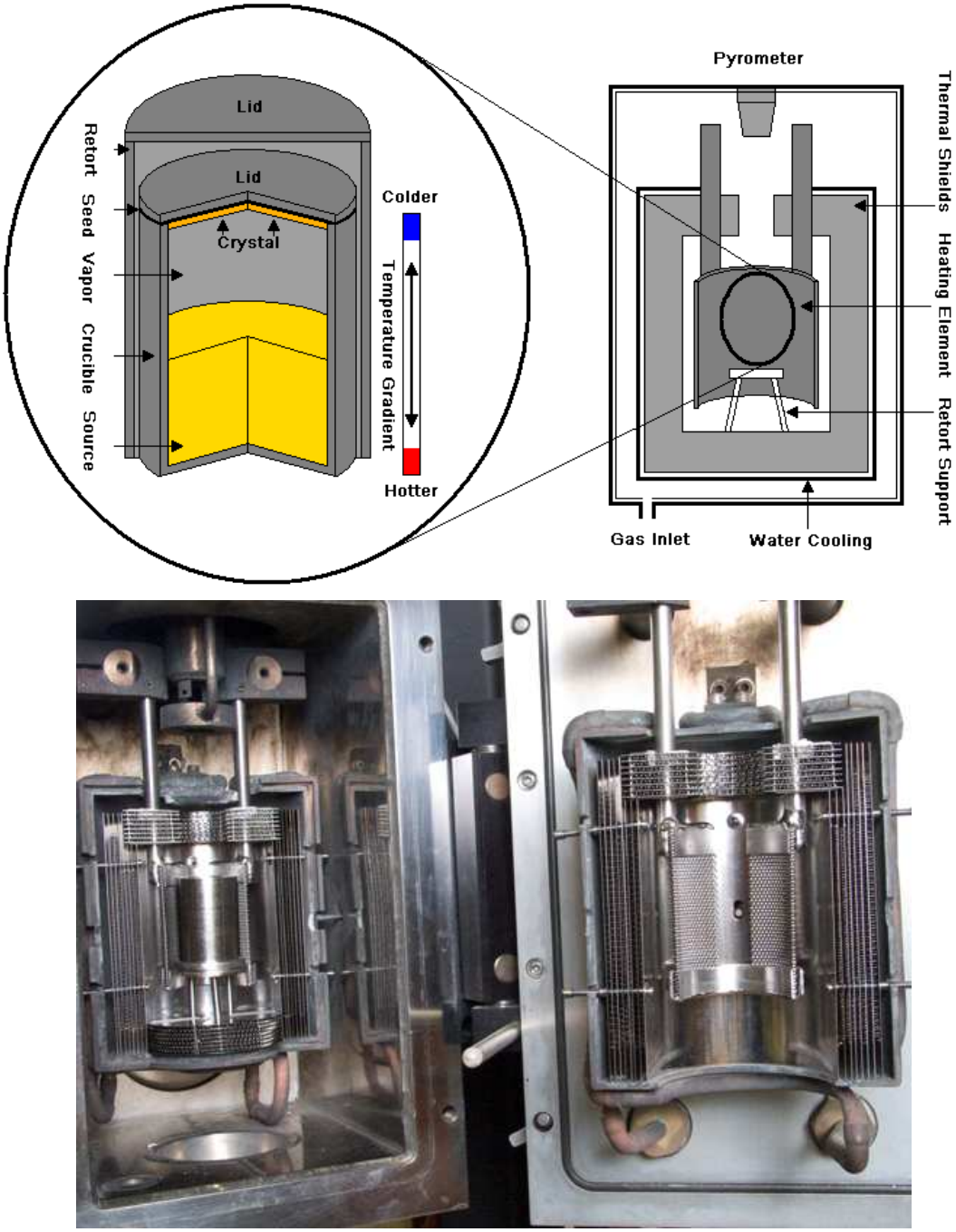

Figure 3.2 Schematic diagram and photo of the furnace chamber.

Figure 3.2 shows a schematic diagram of the growth chamber, as well as a photo of the chamber. The two wire mesh tungsten heating elements were surrounded by tungsten heat shields enclosed in a water cooled jacket. The temperature inside of the heating elements was measured by an optical pyrometer on the top the chamber. The

axial temperature increased in the vertical direction so crystal sublimation-recondensation growth could occur and the vertical temperature gradient was established from a pre-measured temperature profile. Since Al vapor seriously deteriorates the tungsten components, especially the heating elements and thermal shields, and its loss from the crucible reduces the growth rate, a covered crucible where crystal growth occurred, was placed in a covered retort to help confine the Al vapor. The nitride crystals formed on the crucible lid in the case of self-seeded growth, or on seed crystals placed between the lid and top of the crucible in the case of seeded growth. All components in the furnace were made of tungsten. The height of the retort support system was adjustable so that the temperature gradient could be varied. By adjusting the input power, the source sublimation and crystal recondensation temperatures were controlled. The highest operation temperature the furnace was capable of reaching was about 2400°C. Based on a comparison between AlN growth rate in this furnace and that reported by other researchers using other furnaces, the actual furnace temperature may be 100 °C higher than what was measured with the optical pyrometer.

3.2 Source Purification

Oxygen and carbon were residual impurities having highest concentration in the AlN source powder. Both as-received AlN powders and AlN samples exposed to the air needed purification before being used in experiments. The procedures involved for these two types of sources are different. The process for the AlN powder source is more complicated, aimed at reducing the maximum possible impurities. The source / seeds / crystals exposed to the air when the furnace was opened need a purification process before continuing a growth, to remove surface oxides and hydroxides.

For the as-received AlN powder source purification, two methods have been proved effective for reducing the impurities especially oxygen. In the first method, a low temperature source anneal at about 1000 ~ 1200 °C with ultra pure nitrogen ambient was first applied followed by high temperature sintering (>1900 °C) under an ultra pure nitrogen. The first and second steps usually last about 1 ~ 2 hours and 4 ~ 6 hours, respectively. In the second method, a carbothermal reduction step was added into and between the two steps at about 1500°C for about 2 hours. These methods last a similar amount of time as carbothermal reduction can reduce the high temperature sintering time. A detailed description, including the theory explaining its basis is presented in chapter 4.

For long duration growths, additional source had to be added to the crucible as the original source was consumed. When the growing crystal was exposed to the air, oxides and hydroxides formed on the surface, so an additional purification step was needed. After the air-exposed sample was put back to the growth chamber, it was first annealed in a 5% hydrogen and 95% argon gas mixture at about 1200°C and a pressure higher than one atmosphere for 1~4 hours depending on how long the samples were exposed to air and then followed the desired growth procedure.

3.3 Metal Nitridation

For TiN, ZrN, ScN and YN crystal growth, a nitridation step was sometimes needed if a metal source was used. This was necessary if a commercial nitride source was not available. The metal sources were nitridized in the ultra pure nitrogen ambient with pressure higher than one atmosphere (800~900 torr). The temperature required for nitridation varied from metal to metal, from 1200°C to 1800°C. This is discussed in detail in chapter 5. The conversion of the metal to nitride was monitored by measuring the mass

change of the source to determine its metal/N ratio. If the solid mixtures tended to sinter together, nitridation was performed in multiple heat treatments with grinding in between, to ensure good contact of nitrogen gas with the solid.

3.4 Sublimation Growth

If no seeds were employed, the growth was called self-seeded growth. Crystals spontaneous nucleated and grew either on the thick tungsten lid or thin tungsten foil. Generally, the resulting crystals were polycrystalline, except in the case if TiN, ehich was epitaxial on individual tungsten grains (This is also discussed in chapter 5). Ultra high purity nitrogen was used as ambient gas. Because of the temperature gradient, the solid source sublimed in the higher temperature zone (source sublimation) and drives the following reaction in the forward direction, then recondensed in the lower temperature zone (crystal recondensation) and drives the reaction in the reverse direction: $2MN(s) \leftrightarrow 2M(v) + N_2(v)$. Seeded growth was also investigated in this research. Commercialized SiC wafers were used as substrates. Since Si vapor from SiC can form a low temperature eutectic with tungsten, with SiC substrates, the growth temperature was limited to 1800 °C to avoid this problem. All the substrates including the foil/lid for the AlN recondensation were cleaned by solvents in the order of TCE, acetone, methanol, and then rinsed by DI water, before crystal growth.

3.5 Characterization

3.5.1 X-ray Diffraction

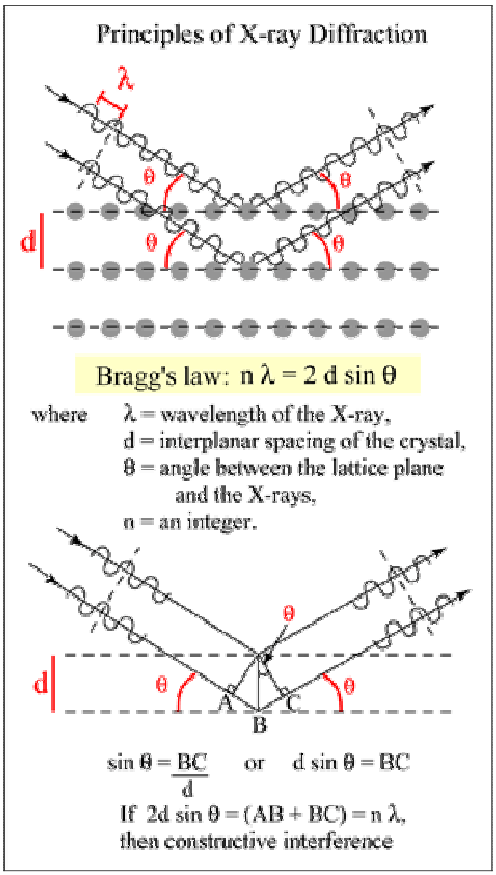

Figure 3.3 Schematic diagram for X-ray Diffraction

Information regarding the crystal structure, chemical composition, and physical properties of the crystals was obtained by x-ray diffraction (XRD). X-rays are electromagnetic radiation with typical photon energies in the range of 100 eV - 100 keV. X-rays striking the material are scattered in all directions. In addition, regularly spaced atoms in a crystal structure can diffract X-rays. Strong diffraction occurs when Bragg's law is satisfied[89]: $\lambda = 2d\sin\theta$, where angle θ is the half angle between the diffracted beam and the original beam diffraction, λ is the wavelength of the X-rays, and d is the interplanar spacing between the planes that cause constructive reinforcement of the beam. A geometric explanation for this phenomenon is shown in Figure 3.3. The lower ray in each figure must travel a farther distance than the upper. If the extra distance (A-B-C) is exactly an integer number of wavelengths (1, 2, 3 ...) then the two X-rays will leave in-

phase. If the distance A-B-C is not an integer number of wavelengths, the two rays will be out of phase, destructive interference will occur. Using a known wavelength (λ) of X-rays, and measuring the angle θ, the spacing d of various planes in a crystal can be obtained. From a comparison of the diffraction pattern with expected peak positions, the crystal structure of materials can be determined.

There are several x-ray diffraction techniques that provide specific types of information about the crystals. Powder XRD is commonly used to identify unknown substances, the materials crystal structure, the lattice constant, and the magnitude of strains in crystalline materials. Thin film XRD can be used to characterize the crystallographic structure and preferred orientation of thin films deposited on substrates. Single-crystal XRD is usually used to solve the complete structure of crystalline materials, for example proteins. In an x-ray pole figure, one can investigate the distribution of crystalline orientations within a crystalline thin-film sample. X-ray rocking curves can quantify the grain size and mosaic spread in crystalline materials.

In this study, powder XRD was used to distinguish the nitrides from metal source, and the fraction of metal converted to nitride, especially for YN. X-ray rocking curves were used to studied the crystal quality, which is indicated by peak widths. X-ray pole figures were used to investigate the orientation distribution of crystals on a substrate. A pole figure is a stereographic projection showing the orientation distribution of a certain direction (pole) within the crystals of the specimen. Figure 3.4 is the x-ray pole figure for AlN crystals on tungsten foil. The distribution for 5 orientations associated with diffraction peaks from AlN are listed. The goal for this research was to investigate the initial growth stage of AlN crystals. The basal plane was set to be (001) and one can

identify the distribution for selected orientation from the pole figure. With tungsten as the substrates (self seeded growth), AlN deposits with a textured orientation, with the (002) plane (C axis up) parallel to the substrate after only 10mins of growth.

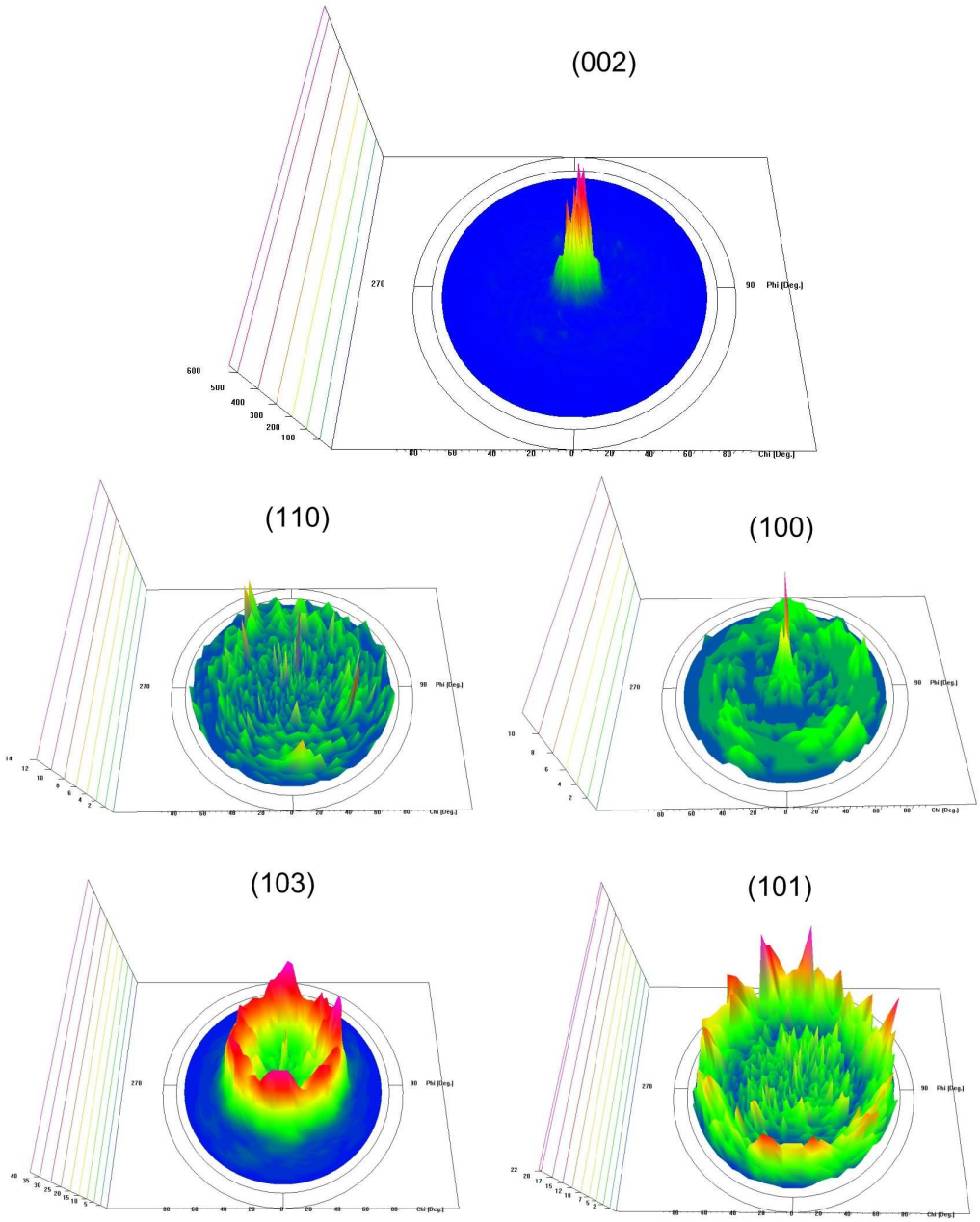

Figure 3.4 X-ray pole figure for thin layer AlN crystals on tungsten substrate.

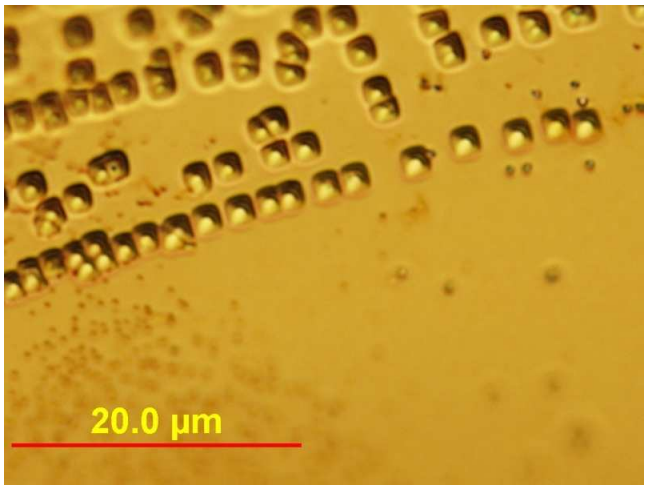

Figure 3.5 Optical photo of pits produced by defect slective etching on TiN crystals.

3.5.2 Microscopy

Optical microscopy was usually the first step used to study the crystal surface morphology. Low magnification images from 10x up to 1000x were obtained. The crystal size, characteristic shapes and visual color were viewed. It was also used to determine the defect selective etching pits densities (Figure 3.5). In this study, optical microscopy was also used to monitor the oxidation of YN crystals as the variation of thickness of surface oxides affects the crystal color under the light (described in Chapter 5).

Scanning electron microscopy (SEM) (Figure 3.6) was also used in this study. This technique uses a focused beam of high-energy electrons to generate a variety of signals at the surface of solid samples. A beam of electrons is produced at the top of the microscope by an electron gun and is accelerated to an energy in the range 0.1- 30keV[90]. The beam travels through electromagnetic fields and lenses, which focus the beam down toward the sample. The accelerated electrons carry significant amounts of kinetic energy, and this energy is dissipated as a variety of signals produced by electron-sample interactions when the incident electrons are decelerated in the solid sample. These signals include secondary electrons (used to produce SEM images), backscattered electrons

(BSE), diffracted backscattered electrons (EBSD that are used to determine crystal structures and orientations), photons (characteristic X-rays that are used for elemental analysis), visible light (cathodoluminescence--CL), and heat.

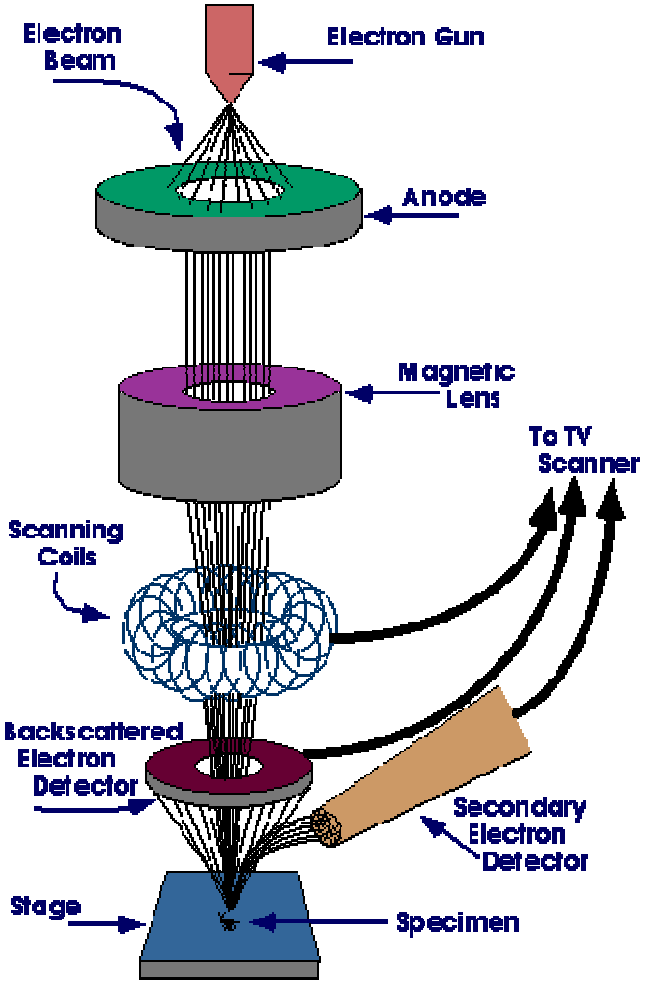

Figure 3.6 Schematic diagram for SEM.

Secondary electrons and backscattered electrons are commonly used for imaging samples. Secondary electrons are most valuable for showing morphology and topography on samples. Backscattered electrons are most valuable for illustrating contrasts in composition in multiphase samples. Both types of images were used in the study. Figure 3.7 are the SEM top view photos for AlN deposited on SiC substrates. Fig.3.6a is produced by secondary electrons and Fig.3.6b is produced by backscattered electrons at

same region. In order to show the morphology better, the left photo was used in this thesis. Figure 3.8 showed SEM photos for the cross section of the AlN crystal on SiC. The upper region is mainly AlN and the bottom region is mainly SiC. Obviously, the photo produced by BSE can give a better detail as it provided cleared contrast.

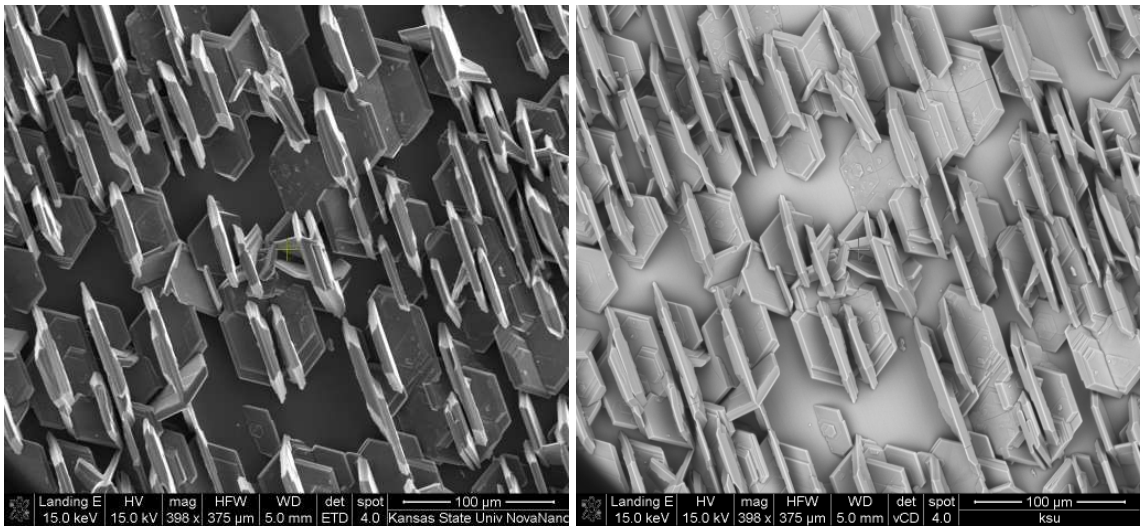

a **b**

Figure 3.7 SEM top view photo for AlN on SiC produced by SE (a) and BSE (b).

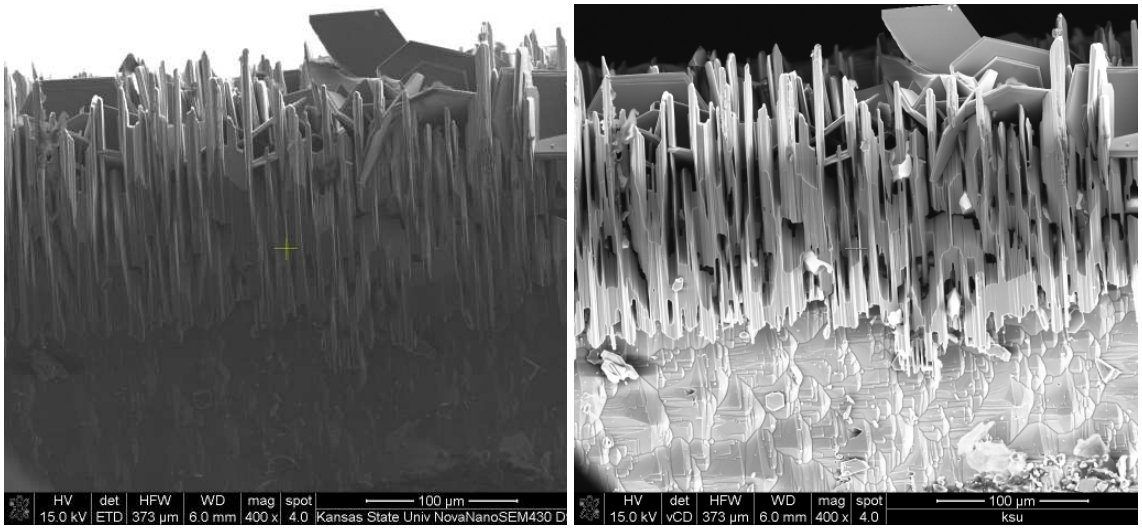

a **b**

Figure 3.8 SEM side view photo for AlN on SiC produced by SE (a) and BSE (b).

SEM is also capable of performing analyses of selected point locations on the sample with energy dispersive x-ray spectroscopy integrated. An energy-dispersive (EDS)

detector is used to separate the characteristic x-rays of different elements into an energy spectrum, which is analyzed to determine the abundance of specific elements. This analysis is non-destructive as x-rays generated by electron interactions do not damage the sample. This approach is especially useful in qualitatively or semi-quantitatively determining chemical compositions. For example in the AlN seeded growth on SiC substrate study, the SiC usually decomposed at the temperature for AlN growth. EDS was used in this study to identify the composition of the crystals on the substrates especially at the initial growth stage.

An SEM that is equipped with electron backscattering diffraction detectors (EBSD) can be used to examine the crystallographic orientation for crystals. Accelerated electrons in the primary beam of a SEM can be diffracted by atomic planes in crystalline materials. These diffracted electrons can be detected when they impinge on a phosphor screen and generate visible lines, called Kikuchi bands, or EBSP's (electron backscatter patterns). These patterns are effectively projections of the geometry of the lattice planes in the crystal, and they give direct information about the crystalline structure and crystallographic orientation of the grains. In this study, EBSD was used to determine the orientation of single TiN crystal grains relative to the orientation of the tungsten grains that it was deposited upon. The relationship between the crystals and the underline substrate was determined by examining a series of samples.

Like EBSD, Electron Channeling Contrast Imaging (ECCI) is also a scanning electron microscope diffraction based techniques.[91] It consists of a commercial scanning electron microscope (SEM) coupled with diode detectors to collect electrons backscattered or forescattered from a crystalline sample.[92] ECC images are produced

from electrons which channel down the crystal planes. When the crystal specimen is tilted near a Bragg angle, because of the localized bending of lattice planes by the individual dislocations, strong fluctuations in the backscattered or forescattered electron yield are created[92]. These changes in electron yield are recorded as dark/ bright intensity fluctuations in the resulting backscattered / forescattered electron images and provide a value for the total dislocation density from the images. Tilt, strain, the presence of defects which distort the crystal planes such as changes in crystallographic orientation or in lattice constant[91], threading dislocations (TDs) and surface steps[93] make changes in grey scale in the ECCI image, and can then be can be revealed. ECCI is used in metallurgy[91] and reported recently to image screw or mixed dislocations in GaN and SiC[92]. In this study, dislocations in the AlN crystals were investigated by ECCI.

3.5.3 Raman

Raman is a common vibrational spectroscopy for assessing molecular motion and fingerprinting species, which is similar to IR (infrared spectroscopy). When a monoenergetic beam of light impinges upon a sample, photons are absorbed and scattered by the material. Most of these scattered photons have exactly the same wavelength as the incident photons and are known as Rayleigh scatter (Figure 3.9), but a tiny portion of the scattered radiation shifted to a different wavelength: Raman scattering. This shift in energy gives information about the phonon modes in the system, and information of materials can be collected. Most of the Raman scattered photons are shifted to longer wavelengths (Stokes shift), but a small portion are shifted to shorter wavelengths (anti-Stokes shift).

By compare the phonon modes of crystal sample, information on crystal properties and quality can be obtained. For instance, the width of the E_2 Raman peak reflects the crystalline quality and stress affects the E_2 phonon frequency[94]. The application of Raman on the Al composition in $Al_xGa_{1-x}N$ layers and growth temperature monitor of GaN layers has been proved[94]. In this study, Raman was used to characterize YN and strain in the AlN crystals.

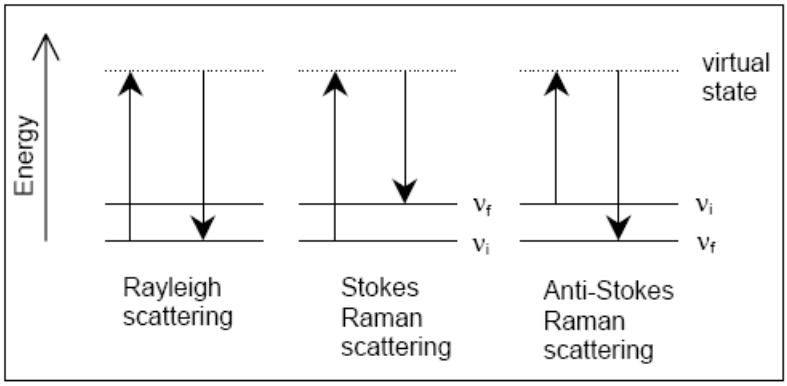

Figure 3.9 Energy-level diagrams
Energy-level diagrams of: Rayleigh scattering, Stokes scattering, and anti-Stokes scattering.

3.5.4 Other methods

Auger spectroscopy is another common surface analytical technique based on Auger effect that named after its discoverer -- a French physicist Pierre Auger: The emission of an electron from an atom accompanying the filling of a vacancy in an inner electron shell.[95] It utilizes the emission of low energy electrons in the Auger process and is one of the most commonly employed analytical techniques for determining the composition of the surface layers of a sample. In this study, scanning auger microprobe was used to measure the surface monolayer elemental composition such as Al, N and O for the crystals, substrates and cross-sectional area. With sputtering attached, the depth profile of each element can be obtained.

Wet etching is a simple method to characterize the crystal polarity and defects. In defect selective etching, defects such as dislocations etch faster than regular area. Only nitrogen polarity basal plane of AlN crystal etches in aqueous potassium hydroxide (KOH), while aluminum polarity basal plane is inert. Both aqueous (KOH) liquid and eutectic KOH/NaOH solution was used in the etching studies. The samples were then rinsed with DI water and blown dry with nitrogen. An example of TiN crystals defect selective etching was shown in Figure 3.5.

LECO analysis is a common technique in this study to measure the overall element concentration in the sample such as C, O, N, Al and Si. LECO is the “generally accepted” industry standard for combustion analysis. It employs a solid- state infrared (IR) and thermal conductivity (TC) detector, with accuracy and precision to five orders of magnitude (sub-ppm to tens of percent).

3.6 References

[89] B.D. Cullity, Elements of X-ray Diffraction, Addison-Wesley publishing Company, Inc. 84 (1956)

[90] J. Goldstein, D. E. Newbury, D. C. Joy, C. E. Lyman, P. Echlin, E. Lifshin, L. Sawyer, J.R. Michael, *Scanning Electron Microscopy and X-ray Microanalysis*, 3rd ed. Kluwer Adacemic/Plenum Pulbishers, 23 (2003)

[91] A.J. Wilkinson and P.B. Hirsch, *Electron Diffraction Based Techniques in Scanning Electron Microscopy of Bulk Materials*, Micron, **28**, 279, (1997)

[92] Y. N. Picard, J. D. Caldwell, M. E. Twigg, C. R. Eddy, Jr., M. A. Mastro,R. L. Henry, and R. T. Holm, *Nondestructive Analysis of Threading Dislocations in GaN by Electron Channeling Contrast Imaging,* Appl. Phys. Lett. **91**, 094106 (2007)

[93] Twigg, Picard, Caldwell, Eddy Jr., Mastro, Holm, Neudeck, Trunek, and Powell, *Diffraction Contrast of Threading Dislocations in GaN and 4H-SiC Epitaxial Layers Using Electron Channeling Contrast Imaging* J. Electron. Mater., **39**, 6 (2010)

[94] M. Kuball, *Raman Spectroscopy of GaN, AlGaN and AlN for Process and Growth Monitoring/Control* , Surf. Interface Anal. **31**, 987 (2001)

[95] A. D. McNaught and A. Wilkinson, Compendium of Chemical Terminology, 2nd IUPAC Blackwell Scientific Publications, Oxford (1997).

CHAPTER 4 - Thermodynamic Analysis and Source Purification of AlN

The unintentional incorporation of impurities in AlN crystals growth by PVT is a significant problem caused by the relatively low purity of source materials and the extremely high temperature employed. Typically, the bulk crystal produced by this technique have high oxygen concentration, on the order of 10^{19} O atoms/cm.[3 96, 97] Currently, commercial AlN powders are produced mainly by the carbothermal nitridation of Al_2O_3 and direct nitridation of aluminum[98]. Impurities introduced in these processes such as carbon and oxygen are probably the origin of the principle impurities in the final AlN crystals. Moreover, aluminum has a strong affinity for oxygen[99]; hence additional oxygen and hydrogen was introduced to the source AlN powder because of the native surface oxide or hydroxide. In addition, the application of graphite furnace or graphite components in the bulk crystals growth also introduces the carbon impurity. Additionally , SiC , a commonly used substrates can be additional source of Si and C.

The effect of impurities on the final product has been widely studied. The main optical absorption band of AlN was extended from 3.5 to 5.5 eV for samples with O~10^{21}/cm^3, thus the present of oxygen in the AlN consumes light generated by the AlN based device [100], hence greatly reduce the efficiency of the device. Oxygen incorporation also degrades AlN thermal conductivity[101, 102] and crystal quality has been found to degrade dramatically at high oxygen concentrations[101]. Adding select impurities can be benefitis: Fukuyama's group [103, 104] showed that adding carbon can reduce oxygen

content. In addition, the oxygen effect on the AlN crystal growth also has other effects. M. S. Ramm' group analyzed the role of oxygen in the sublimation growth[105]; closed-box thermodynamics calculations on six selected gaseous species indicated that the vapor contamination by oxygen gives rise to gaseous Al_2O and AlO promoting Al-containing species transport to the seed at temperatures lower than 2000 K. Additionally, the critical oxygen fraction in the vapor corresponding to Al_2O_3 inclusion generation on the AlN surface was determined[105]. Thus, High degree of AlN powder purification is required to prevent the growing AlN crystals from inclusions. Obviously, in order to get AlN crystals with good quality, the residual impurities concentration should be limited. However, few studies have focused on the AlN powder purification process; purification procedures are still under investigation. This chapter is the combination of past efforts on impurities incorporation and AlN source purification based on published results.[106, 107, 108] Both thermodynamic analysis and experiment results are reported.

4.1 Thermodynamic Analysis

The goal of this thermodynamic analysis is to understand which volatile species form and can transport impurities through the gas phaseduring the AlN crystal growth. This analysis assumes there are no adsorption or nucleation barriers at the source and seed interfaces. Pure N_2 gas was the ambient gas. The total pressure was calculated from the ideal gas law knowing the initial temperature and pressure. Two solid-vapor equilibriums were assumed, one at the source sublimation zone at temperature Ts, the other at the crystal growth zone at temperature Tc. The furnace was modeled as a one dimensional temperature gradient along the sublimation-recondensation direction.

Table 4.1 Possible species formed for each system of elements

Al-O-C-N system | **Al-O-N system** | **Al-O-H-N system**

	N-C-O	Al-C	N-C	N-O	Al-N	Al-O	Al-H-O	H-N	H-N-O	
Solid Liquid		Al_4C_3 C,		AlON*	AlN Al, Al	Al_2O_3	$Al(OH)_3$* AlOOH* H_2O			Liquid Solid
Gas	CO_2, CO, C_3O_2, C_2O, NCO	C, C_2, C_3, C_4, C_5, AlC	CNN, NCN, CN, C_2N, C_2N_2, C_4N_2	NO, NO_2, NO_3, N_2O, N_2O_3, N_2O_4, N_2O_5	Al, Al_2, N, N_2, N_3, AlN	O, O_2, O_3, Al_2O, AlO, Al_2O_2, AlO_2	H_2O, H_2O_2, HO, AlH, OAlH, AlOH, OAlOH	H_3N, H_4N_2, H_2N_2, H_2N, HN, H_2	HNO, $HONO_{cis}$ $HONO_{trans}$ HONO2	Gas
		CH	CH_2 CHN	CH_3 CHNO	CH_4 CHO	C_2H C_2H_4O	C_2H_2 CHNO	C_2H_4		

Al-O-C-H-N system

Si-C-Al-N system incude (Al-N, Si-C, Al-C, Si-N)

	Si-C						Si-N		
Gas Liquid Solid	Si,	Si_2,	Si_3, Si Si	Si_2C, SiC	SiC,	SiC_2	Si_2N	Si_3N_4	SiN,

The crystal growth zone was assumed to be 5 to 50 °C lower in temperature than the source sublimation zone, thus ΔT equals Tc minus Ts. Reactions used in thermodynamic calculation were represented as:

$$aA(s) + bB(g) = cC(g) + Dd(g) \tag{4-1}$$

Then the equilibrium constant of the reaction were expressed by:

$$K = \frac{\alpha_C^c \cdot \alpha_D^d}{\alpha_A^a \cdot \alpha_B^b} = \exp(-\frac{\Delta rG^0}{RT}) = \exp(-\frac{\sum \upsilon_i \Delta_f G_i^{\ 0}}{RT}) \tag{4-2}$$

Where α_i is the activity of the reactants or products i with reference to their standard states (pure substance, activities of unity and 0.1 M Pa) and ν is the stoichiometric coefficients. Free energy of formation $\Delta_f G^0_i$ comes from JANAF data[109].

All possible electrically neutral species for which thermodynamic data was available in the JANAF table[109] were considered in this study. They are listed in Table 4.1 in three columns: Al-O-N, Al-O-C-N, and Al-O-H-N. Impurities and their concentration in the as-received AlN powder according to the analysis by the supplier are listed in Table 4.2. An inert gas fusion technique (LECO analysis) was used to measure the hydrogen concentration since it is not reported by the AlN source powder supplier, and to verify the oxygen concentration as aluminum has a strong affinity for oxygen. To simplify the thermodynamic analysis, impurities with concentrations lower than 0.01 at% were assumed to be negligible. Values of 0.9wt% oxygen and 0.024wt% hydrogen were obtained.

Table 4.2 The concentration of impurity elements in AlN powders*.

Element	Al	N	O	C	H	Ga	Si	Fe	Ni
Wt%	65.4 Wt %	33.6%	0.84%	0.06%	0.02%	70ppm	30ppm	10ppm	10ppm

***: O and H are from LECO analysis, others are from[110]**

To simplify the analysis, simple systems considered for 4 cases according to the impurity source: Al-O-N, Al-O-H-N from, Al-O-C-N, and Al-N-Si-C representing sublimation recondensation growth in a tungsten furnace (or other non-reacting furnace) with oxides only, a tungsten furnace with oxides and hydroxides, a graphite furnace ($\alpha_{C_s} = 1$), and AlN growth on SiC seeds respectively. Al-O-N system was investigated at the Ts range of 1700 ˚C to 2400 ˚C, which spans the full range of temperatures typically employed for AlN crystal growth by PVT. As we previous summarized the analysis by several groups on AlN hydroxides[107], and experimentally demonstrated that a heat treatment under 900˚C in either vacuum or under nitrogen can decompose the aluminum hydroxides, the investigated temperature for Al-O-H-N system was started from 900 ˚C. These two systems can be considered for the cases that impurities came only from the purchased AlN powder. The highest temperature of interest for AlN growth on SiC seeds is lower than the other cases, as higher temperatures lead to rapid SiC decomposition.

4.1.1 Al-O-N

Thermodynamics calculation predicted that the major gas-phase species present are N_2, Al, Al_2O, Al_2, and AlO; gas species AlN, Al_2O_2, AlO_2, NO, NO_2, N_2O, N_3, O, O_2 with pressure lower than 10^{-6} atm are negligible, while other gas species NO_3, N_2O_3, N_2O_4, N_2O_5, O_3, N with pressure lower than 10^{-28} atm are unlikely to be present in the vapor. Figure 4.1shows the partial pressure of the major gas species as well as AlN. Aluminum gas (Al) has the highest partial pressure. Dialuminum monoxide (Al_2O) is strongly favored over all other possible oxygen containing compounds. A possible representative reaction for the formation of Al_2O is:

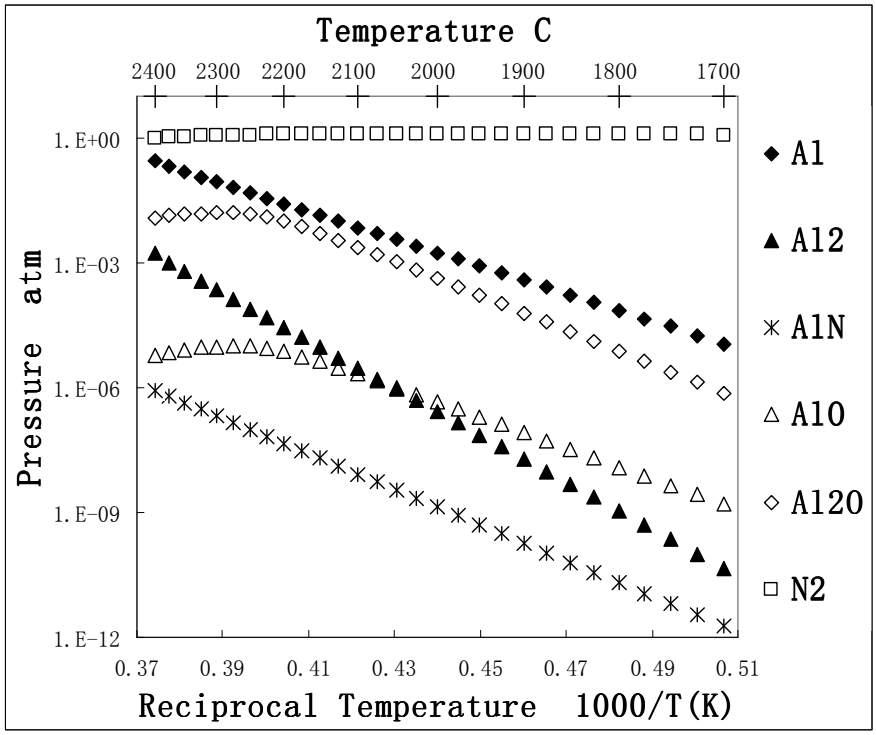

Figure 4.1 Partial pressure of the majority gas species in Al-O-N system.

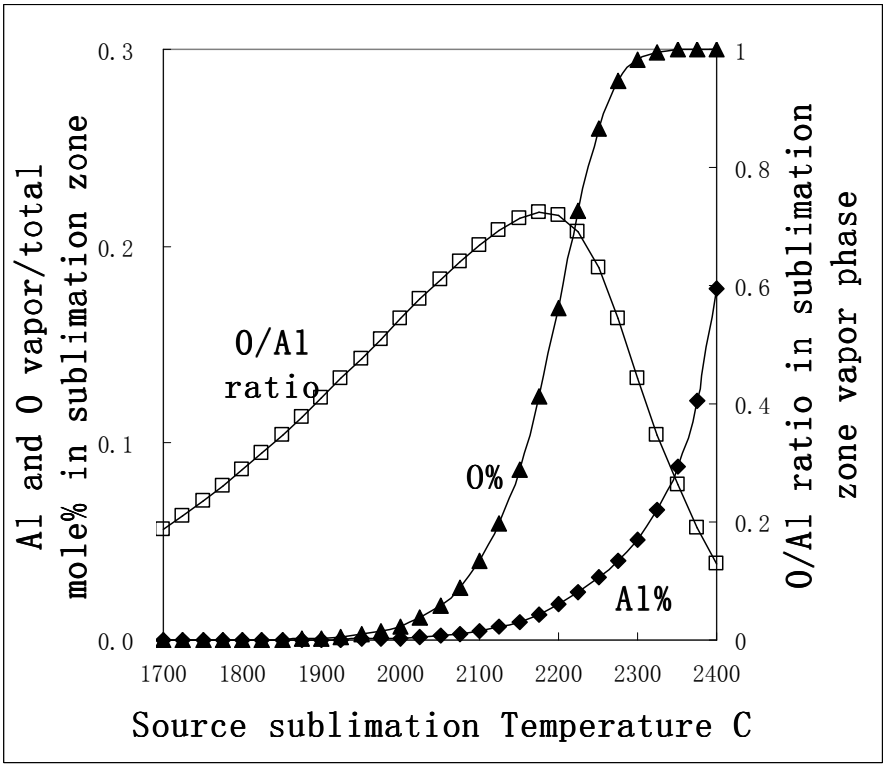

Figure 4.2 O/Al ratio in vapor and element vapor/total mole% for sublimation zone

$$Al_2O_3(s) + 4Al(g) \Leftrightarrow 3Al_2O(g) \quad (4\text{-}3)$$

And equilibrium constant (in logarithmic form) for this reaction is:

LogK: 3.328(2100 K), 3.164(2200 K), 3.010(2300 K), 2.865(2400 K), 2.728(2500 K)

All the reactions forming other oxygen containing species have negative *LogK*s.

Figure 4.2 shows the quantity of Al and O entering the vapor phase in percentage of the total element mole number and the O/Al mole ratio in the vapor phase for AlN sublimation zone. Both Al and O begin to enter the gas phase at 1900˚C. Much of the oxygen originally present in the source enters the gas phase: 56.3% at 2200˚C and 99.5% at 2300˚C. In comparison, less of the Al present in the source enters the gas phase: 6.0% at 2200˚C and 17.1% at 2300˚C. The O/Al ratio in the vapor is always higher (>0.03885) than in original source (0.02314) reaching a maximum around 2200 ˚C. This maximum is probably the consequence of the relatively strong stability of Al_2O at high temperature drawing the equilibrium to the right, while depletion of oxygen from the source and higher Al vapor pressure from AlN causes a decrease in the O/A as the temperature increases.

Figure 4.3 shows the O/Al ratio in the vapor phase of crystal growth zone as a function of the temperature difference (TD); each curve represents AlN sublimation-recondensation process at same sublimation temperature (Sub-T) but different growth temperature (Grow-T). The O/Al ratio increases then decreases as the Grow-T decreases from 5 to 50°C in the Sub-T range of 1700˚C ~1900˚C, for instance, looking at the 1800˚C curve, the O/Al ratio is 0.0862 in the source zone (when TD is 0); it increases to 0.1012(when TD is -30°C) and then decreases to 0.0985(when TD is -50°C). In comparison, in the Sub-T range of 1900˚C ~2400˚C, the O/Al ratio never decreases but

keeps increasing, which suggests Al_2O is not stable in the gas phase when Sub-T is below 1900 ˚C. As most of the oxygen goes to vapor (Sub-T: 2200˚C ~2400˚C), O/Al ratio increases much faster (dashed curve is sharper than real curve) as the Grow-T decreases from 5 to 50°C, which implies that oxygen tend to stay in vapor at high temperature.

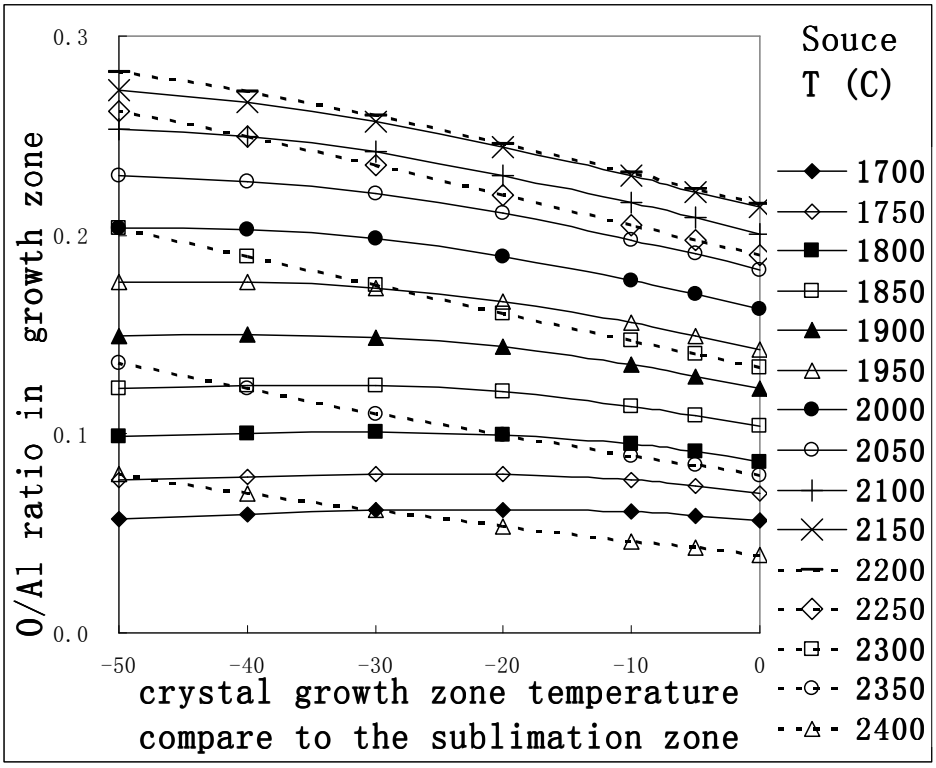

Figure 4.3 O/Al ratio in the vapor phase of the crystal growth zone

4.1.2 Al-O-H-N

When aluminum oxides react with water vapor in the air, hydroxidation occurs. As native hydroxides are always accompanied with native oxides, the hydrogen impurity is adding to the above basic system now and the new system is Al-O-H-N. Aluminum hydroxides are easily decomposed in the AlN source annealing process. The amorphous thin film that forms may be a mixture of one or several Al-O-H compounds such as aluminum trihydroxide $Al(OH)_3$, aluminum oxide hydroxide AlOOH / $Al_2O_3 \cdot H_2O$, or aluminum oxide Al_2O_3 [111]. Aluminum hydroxides are easily decomposed; several

studies[107] showed significant amounts of water desorbing after simple heating process at temperature lower than 900 °C. According to our thermodynamic calculation, all the H enters vapor phase and the Pp of hydrogen containing species remain unchanged in the typical Ts range of 1700 ˚C to 2400 ˚C.

When the studied temperature range was reduced to 900 °C to 1200 °C, for a total pressure of 500 torr (0.658 atm, Figure 4.4a) and 1 torr (0.001 atm, high vacuum, Figure 4.3b), thermodynamics calculation predicted that the major gas-phase species present are N_2 and OAlOH. Although the Al vapor higher pressure is higher under vacuum (about 10^{-9}), it is a minor gas species. Gas species Al_2O, Al_2, AlO, AlN, Al_2O_2, AlO_2, NO, NO_2, N_2O, N_3, O, O_2 with pressure lower than 10^{-10} atm are negligible, while other gas species NO_3, N_2O_3, N_2O_4, N_2O_5, O_3, N, H_2O, H_2O_2, HO, H_2, AlH, OAlH, AlOH, H_3N, H_4H_2, H_2H_2, H_2N, HN, HNO, HONOc, HONOt, $HONO_2$, with pressure lower than 10^{-28} atm are unlikely to be present in the vapor. While Al_2O gas is only stable at high temperature (higher than 1900˚C), OAlOH gas is stable at lower temperature regardless of the ambient. In addition, the lower Al/O mole ratio in OAlOH (0.5) than Al_2O (2) indicates less source mass is lost during the removal of oxygen from the solid phase. Since no crystal growth process is happening, the species OAlOH is actually removing the O and H from the source.

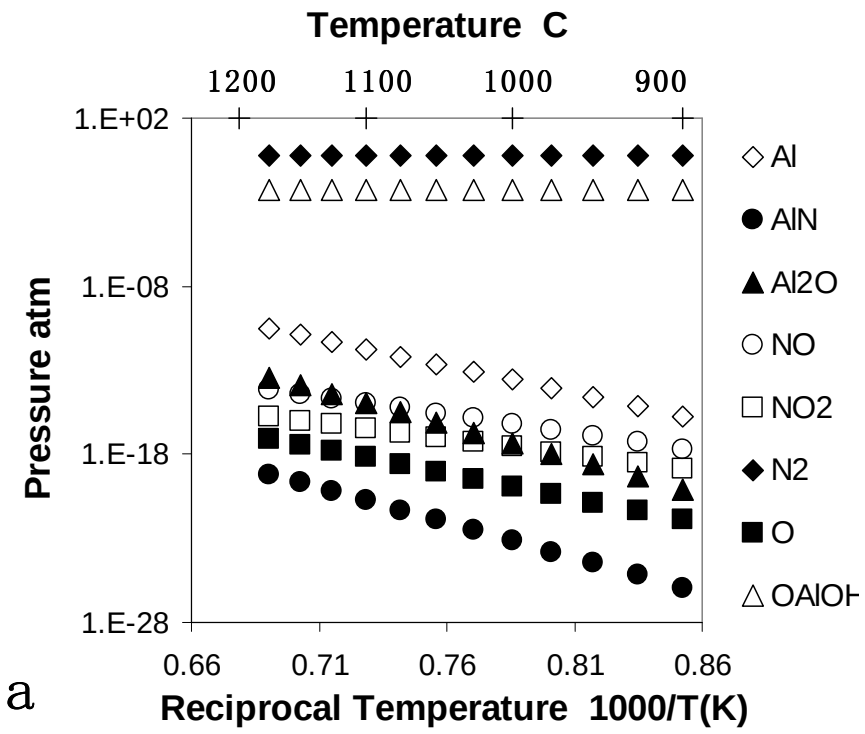

a

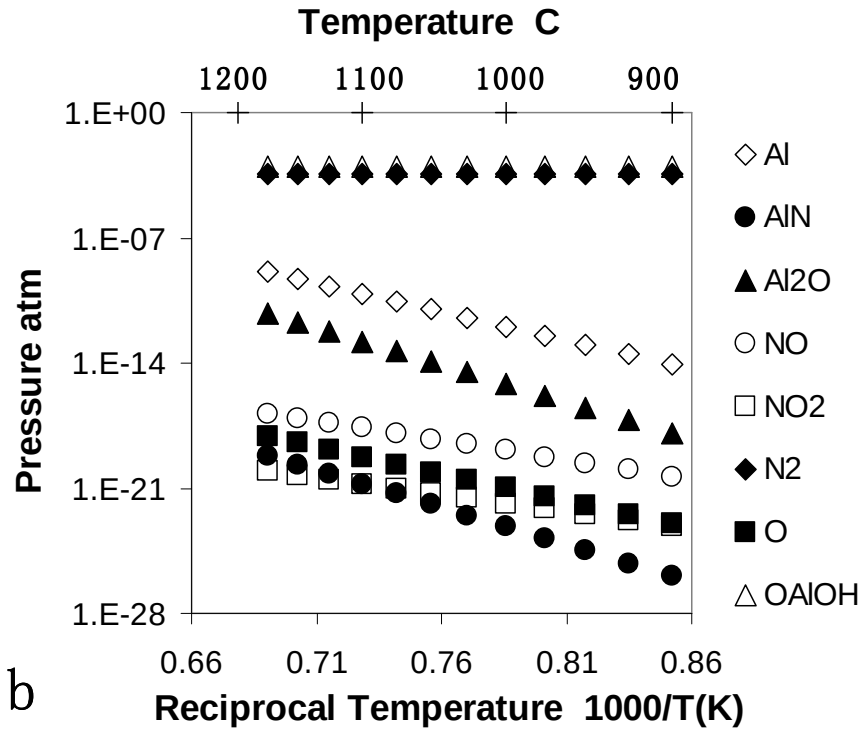

b

Figure 4.4 Partial pressure of the selected gas species in Al-O-H-N system a, total pressure is 500 torr (0.658 atm); b, total pressure is 1 torr (0.001atm).

4.1.3 Introduced impurities

In addition to impurities from the source powder, impurities can also originate from the environment and the substrates. For example, graphite is a common material for furnace, retort, and crucibles in the AlN sublimation crystal growth process, adding carbon impurities to the system. Without native substrates, various available foreign substrates such as silicon carbide may also introduce impurities.

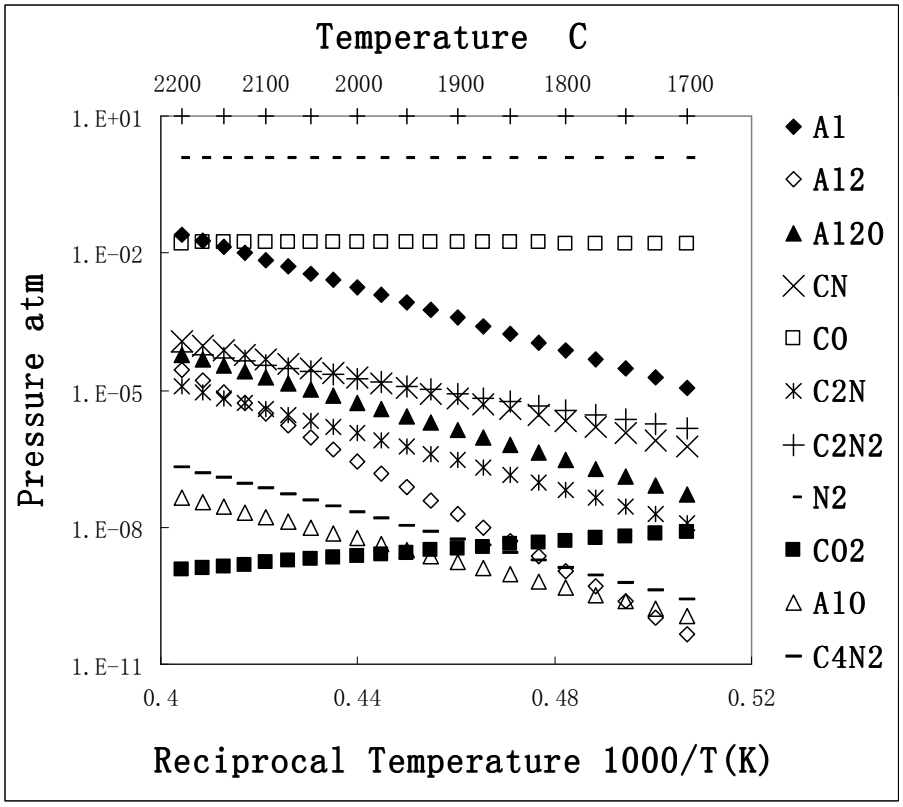

Figure 4.5 Partial pressure of the majority gas species in Al-O-C-N system.

4.1.3.1 Al-O-C-N

If a graphite furnace/components was considered for the above Al-O-N system, infinity carbon is available ($\alpha_{C_S} = 1$) during in the crystal growth process, therefore the three elements system become four elements system Al-O-C-N.

All the species whose concentrations are negligibly small in the Al-O-N system are not changed by the addition of carbon, and carbon species CNN, NCN, C, C_2, C_3, C_4, C_5, C_3O_2, C_2O, AlC, and NCO with pressure lower than 10^{-10} atm can be negligible too. N_2, CO, Al, CN, C_2N_2, Al_2O, Al_2, AlO, C_2N, C_4N_2 CO_2 are the majority species in vapor (Figure 4.5), among which CO is the main species containing carbon and oxygen with pressure even higher than Al gas. The presence of carbon changed the oxygen distribution in the gas phase; CO is easily formed and is much more stable than all other O containing species including Al_2O. Possible reactions forming CO include:

$$Al_2O_3(s) + 3C(s) \Leftrightarrow 2Al(g) + 3CO(g) \quad (4\text{-}4)$$

$$Al_2O_3(s) + 3C(s) \Leftrightarrow Al_2(g) + 3CO(g) \quad (4\text{-}5)$$

$$Al_2O_3(s) + C(s) \Leftrightarrow Al_2O(g) + 2CO(g) \quad (4\text{-}6)$$

$$Al_2O_3(s) + C(s) \Leftrightarrow 2AlO(g) + CO(g) \quad (4\text{-}7)$$

The Al species subsequently react to form AlN by carbothermal reduction in a nitrogen rich condition. 99.962% of oxygen impurity goes to vapor phase in the form CO as the AlN sublimates at 1700˚C, and only 0.001% of oxygen is left as AlN sublimates at 1900˚C. The CO partial pressure is almost unchanged in crystal growth zone, which implied most C and O impurities tend to stay in the gas phase during the crystal growth.

In the absence of oxygen, carbon can still be transported by cyanogen (CN) and dicyanogen (C_2N_2). The partial pressure of these species is significant, on the same order as that for aluminum. Besides being responsible for the transport of carbon in the vapor phase and potentially its incorporation into the growing AlN crystal, all graphite components are subject to erosion through the formation of CN and C_2N_2. The lifetime of graphite components in nitrogen is limited at high temperatures due to the formation of

these compounds. Thus, the use of graphite components should be avoided in the crystal growth of AlN.

4.1.3.2 SiC substrate

Silicon carbide is the most common single crystal employed in seeded growth of bulk AlN because of its large availability and orientation control of AlN. Here the Al-N-Si-N system is investigated with Ts range from 1700 ˚C to 2400 ˚C. SiC is not stable at high temperature; it decomposed at temperature much lower than that commonly required for AlN bulk crystal growth.

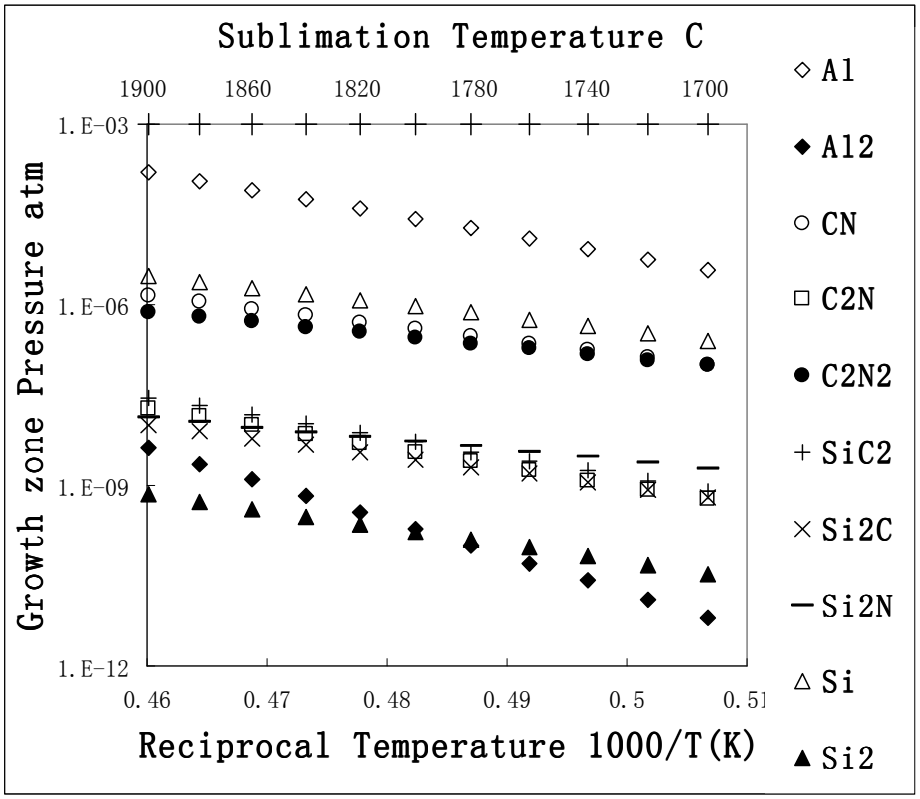

Figure 4.6 Partial pressure of the majority gas species in Al-C-Si-N system.

Although Al gas has the highest partial pressure, significant partial pressure of Si, CN and C_2N_2 were predict by the thermodynamic model, additional silicon and carbon gaseous species present in nitrogen ambient including Si_2N, Si_2C, SiC_2, Si_2 and C_2N.

Moreover, Al_2 has similar order of magnitude as Si_2. Partial pressure of all the other gaseous species are lower than 10^{-10} atm. Figure 4.6 shows the partial pressure of major gas species in crystal growth zone at temperature 50 ˚C lower than source sublimation zone. Possible reactions are in table II. The most probable volatile species originating from SiC seed are Si, Si_2C, SiC_2, Si_2, The presence of nitrogen accelerates the decomposition of the SiC through the formation of additional vapor phase species such as Si_2N, CN, C_2N_2 and C_2N.

Table 4.3 Reactions and equilibrium constant forming Si_2N and Si_2C

	Reaction	Log K at T		
		2100K	2200K	2300 K
(4-8)	$SiC(s) \Leftrightarrow Si(g) + C(g)$	**-13.787**	**-12.480**	**-11.287**
(4-9)	$2Si(g) + C(g) \Leftrightarrow Si_2C(g)$	**13.223**	**11.990**	**10.864**
(4-10)	$Si(g) + 2C(g) \Leftrightarrow SiC_2(g)$	**18.063**	**16.617**	**15.297**
(4-11)	$4Si(g) + N_2(g) \Leftrightarrow 2Si_2N(g)$	**6.544**	**5.410**	**4.374**
(4-12)	$2C(g) + N_2(g) \Leftrightarrow 2CN(g)$	**7.740**	**7.010**	**6.352**
(4-13)	$2C(g) + N_2(g) \Leftrightarrow C_2N_2(g)$	**15.761**	**14.193**	**12.782**

4.1.4 Complex System

Based on the analysis above, one can conclude that all the three impurities oxygen, hydrogen, and carbon have corresponding gas species stable at certain temperature range, which indicates the possibility of removing these impurities by heating process (annealing / sintering). It is highly possible to remove hydrogen impurity before the crystal growth process occurs. Although graphite components should be avoided for the crystal growth of AlN, carbonthermal reduction is effective in producing AlN from Al_2O_3. The removal process of hydrogen and carbon can also remove oxygen. Therefore, it is important to select the heating process temperature range for removing the maximum impurities possible before the crystal growth process. In order to optimize the

process, non-reacting furnace/components and substrate were selected for the following analysis. Carbon was considered as both residual impurity for as-received powder and introduced impurity for carbonthermal reduction.

For the system with carbon, thermodynamic analysis shows that the major gas-phase species present are still N_2 and OAlOH (with pressure of about 10^{-3}). Consider carbon as a residual impurity in the as-received powder; figure 4-7a represents the partial pressure for the gas species that has partial pressure higher than 10^{-13} at the calculated temperature range. Between 900 °C to 1200 °C, CO is a minor gas species (with a partial pressure between 10^{-6} -10^{-8}). The addition of carbon does not change the concentrations of those species which are negligibly small in the Al-O-H-N system. Carbon containing species C_2N_2, C_2N, C_4N_2, CNN, NCN, C, C_2, C_3, C_4, C_5, C_3O_2, C_2O, AlC, NCO, CH, CH_2, CH_3, CH_4, C_2H, C_2H_2, C_2H_4, CHN, CHNO, CHO, C_2H_4O and CHNO with pressure lower than 10^{-12} atm are also negligible. Between 1400 °C to 1600 °C (Figure 4.7a), CO gas with pressure between 10^{-4} -10^{-6} become the third most major gas species. Between 1900 °C to 2100 °C (Figure 4.7), both the Al and Al_2O partial pressures increased faster than that of CO gas as the temperature increased. The Al_2O partial pressure finally exceeds CO above 2050 °C. Since the partial pressure of cyanogen (CN) is lower than 10^{-10} at 1400 to 1600 °C and 10^{-8} at 1900 to 2100 °C, CO is the main carbon containing gas species in Al-O-C-H-N system in an inert reactor.

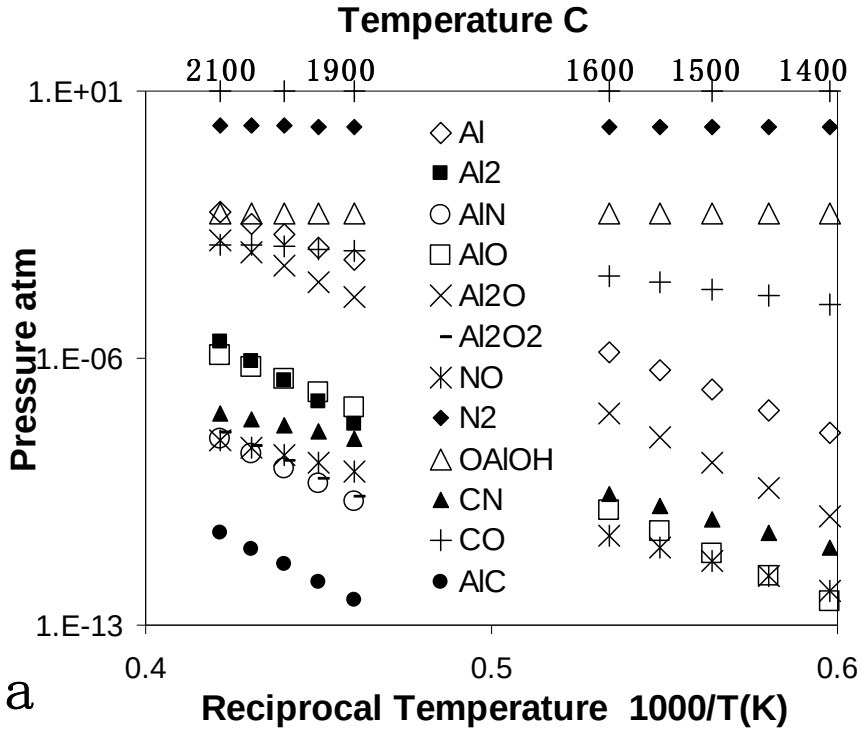

a

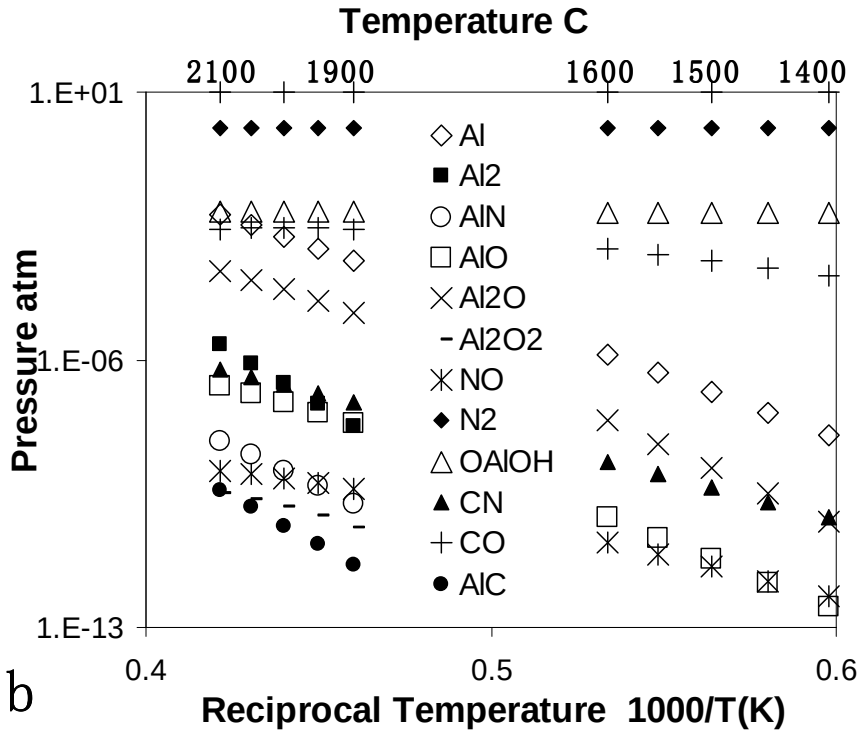

b

Figure 4.7 Partial pressure of the selected gas species in Al-O-C-H-N system. (a), as received AlN source; (b), AlN source with additional carbon

Aluminum oxides and hydroxide can be written as $(Al_2O_3)_x(H_2O)_y$ to emphasize the water they contain. By adding carbon, oxygen can be removed by transferring all the oxygen from Al_2O_3 to CO, thus the total moles of carbon are the same as that of oxygen in Al_2O_3. Then partial pressures for this new system were represented in Figure 4.7b. Compare Figure 4.7a and Figure 4.7b, N_2 and OAlOH are still the major gas species at all the calculated temperature range (900 °C to 2100 °C) for the system with added carbon (Figure 4.7b) . CO is become the third major gas and has significant pressure increasing since 1400 °C. At the same temperature, the partial pressure of CO is higher for the system with added carbon (fig.2b). The pressure of cyanogen is lower than 10^{-10} in this temperature range. Between 1900 °C to 2100 °C, the sharp increasing in the Al_2O partial pressure was constrained by additional CO, and was always lower than that of CO.

4.2 Source Purification of AlN

Based on the thermodynamic analysis, one step of high temperature treatment (>1900 °C) should remove most of the impurities in theory. In fact, one step high temperature sintering (>1900 °C) has been proved to be effective at reducing oxygen concentration[107] as surface area of the AlN source was reduced, hence much less surface oxides and hydroxides formed if the source was exposure to the air or water vapor in the air after the treatment. However, as the crystal growth process all occurs at this temperature, long time sintering at this temperature results in high source mass loss. Besides, the effect of high temperature sintering on impurities diffusion in the material has not been considered. The process can effectively reduce the impurities concentration before crystal growth process happening need take into consideration.

According to thermodynamic analysis, OAlOH, CO, and Al_2O are the major impurity-containing species when the AlN source is directly heated to temperature higher than 1900 °C. Their significant higher partial pressure compared to Al and stability in the vapor helped impurities removal from the solid phase. In contrast, OAlOH is the only impurity containing species if first annealing AlN source at about 1000 °C. The oxygen and hydrogen can be removed first through OAlOH volatilization and then by Al_2O forming when the temperature is increased to 1920°C. The low Al/O ratio of OAlOH over Al_2O indicates the source purification with low AlN source mass loss.

Three sets of experiments were run to remove oxygen from the AlN source and compared: 1，directly sintering at1950 °C, 2, a previous 1000 °C annealing followed by high temperature sintering, and carbothermal reduction at 1500°C after low temperature annealing before high temperature sintering. Figure 4-8 shows the O (a) and H (b) concentration in the AlN source vesus source mass loss. Comparing the two sets of experiments (triangle stands for the source only sintering at 1950°C; diamond stands for the source annealing at 960－1000 °C followed by sintering at 1920°C), for the same AlN source mass loss, the experiments with the low temperature annealing step have lower O and H concentration in general, indicating more effective source purification. Additional carbothermal reduction improved this result; with only 5.5% of mass loss, the purification produced a source with low O, H, and C concentrations of 0.018 wt%, 6 ppm, and 0.006wt%.

Thermodynamic analysis predicts that CO is the major oxygen containing species and only carbon containing vapor species between 1400 °C to 1600 °C, thus a carbothermal reduction at 1500°C after the 1000°C annealing can further reduce oxygen

with nearly zero source mass loss. Considering that as-received AlN powder has an impurity concentration of 0.9 wt% O, 0.024wt% H, and 0.06wt% C, the atomic ratio of C:H:O is 4:19:45. Since aluminum oxides and hydroxides can be written in the form of $(Al_2O_3)_x(H_2O)_y$, additional C is need to remove oxygen from the aluminum oxide while minimizing the mass source loss. After high temperature sintering, O and H concentration were tested (the circle in Figure 4.8). With only 5.5% of mass loss, More than 98% of O, 99.9% of H and 90% of C originally in the source was removed.

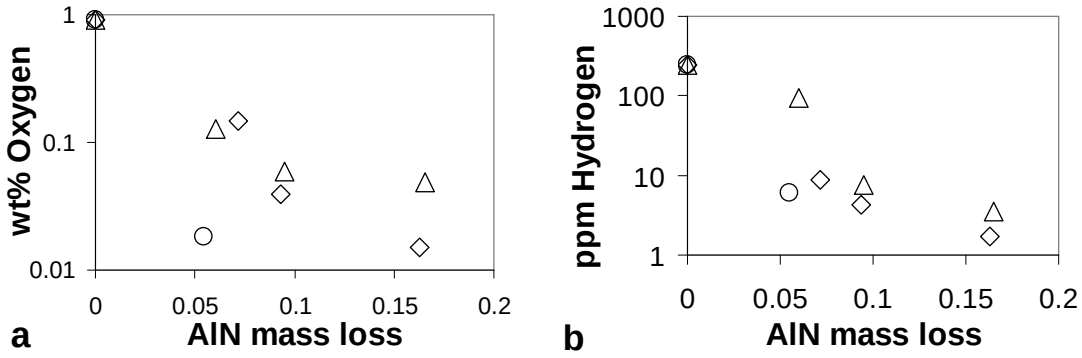

Figure 4.8 Impurities (wt%) in the AlN source as function of the source mass loss. Δ- source only sintering at 1950°C; ◊ - source annealing at 960–1000 °C followed by sintering at 1920°C; o **- source with added carbon for carbothermal reduction during the annealing process.**

However, the theoretical calculation may only refer to the oxygen and hydrogen that originates from surface aluminum oxides and hydroxides. If the impurities were trapped inside of the materials (or volume impurities), for example, the impurities dissolved in the bulk AlN or trapped at internal surfaces of voids, the impurity diffusion kinetics need take into consideration. Therefore there is a minimum impurity concentration that sintering can achieve, which has been addressed before[101] in our study from different point of view. Meanwhile, the stability of the major impurity containing species OAlOH, CO, and Al_2O in the gas phase suggest that impurities trapped inside of the materials (or volume impurities) may be removed by recrystallization of aluminum nitride by, for example, completely subliming and recondensing the source material.

4.3 References

[96] M. Bickermann, B.M. Epelbaum, A. Winnacker, *Characterization of bulk AlN with low oxygen content*, J. Crystal Growth, **269**, 432 (2004)

[97] V. Noveski, R. Schlesser, B. Raghothamachar, M. Dudley, S. Mahajan, S. Beaudoin, Z. Sitar, *Seeded growth of bulk AlN crystals and grain evolution in polycrystalline* AlN boules, J. Crystal Growth 279, 13 (2005)

[98] Wataru Nakao, Hiroyuki Fukuyama, and Kazuhiro Nagata, *Gibbs Energy Change of Carbothermal Nitridation Reaction of Al_2O_3 to Form AlN and Reassessment of Thermochemical Properties of AlN*, J. Am. Ceram. Soc., **85**, 889 (2002)

[99] K. Wafers, C. Misra, Oxides and hydroxides of aluminum, Alcoa Technical Paper no. 19, Revised Alcoa Laboratories, Pittsburgh, PA, (1987)

[100] J. Pasternak, L. Roskovcova, Phys. Status Solidi, 26, 591 (1968)

[101] G. A. Slack, L. J. Schowalter, D. Morelli, and J. A. Freitas Jr., *Some effects of oxygen impurities on AlN and GaN*, J. Cryst. Growth **246**, 287 (2002)

[102] M. Miyanaga, N. Mizuhara, S. Fujiwara, M. Shimazu, H. Nakahata, T. Kawase, J. Crystal Growth **300**, 45 (2007)

[103] W. Nakaoa, H. Fukuyama, K. Nagata, Thermodynamic Stability of γ-Aluminum Oxynitride, Journal of The Electrochemical Society, **150**, J1 (2003)

[104] H.Fukuyama, S.Kusunoki, A.Hakomori, and K.Hiraga, *Single crystalline aluminum nitride films fabricated by nitriding α-Al_2O_3*, J. Appl. Phys. **100**, 024905 (2006)

[105] S. Yu. Karpov, A. V. Kulik, I. N. Przhevalskii, M. S. Ramm, Yu. N. Makarov, *Role of oxygen in AlN sublimation growth*, phys. stat. sol. **7**, 1989 (2003)

[106] L. Du and J.H. Edgar, *Thermodynamic Analysis of Impurities in the Sublimation Growth of AlN Single Crystals*, Mater. Res. Soc. Symp. Proc. 955 I11-05 (2007).

[107] J.H. Edgar, L. Du, R.G. Lee, L. Nyakiti, J. Chaudhuri, *Native oxide and hydroxides and their implications for bulk AlN crystal*, Crystal Growth **310**, 4002 (2008)

[108] Li. Du, J.H. Edgar, Edward A. Kenik, Thermodynamic Analysis and purification for source materials in Sublimation Crystal Growth of Aluminum Nitride, Mater. Res. Soc. Symp. Proc. 1202-I05-08 (2010)

[109] M. W. Chase, Jr., NIST-JANAF Thermochemical Tables, 4th ed., Am. Chem. Soc., DC, (1998), Am. Inst. Phys., NY, (1998), the NIST, Gaithersburg, MD (1998)

[110] N. Saito, C. Ishizaki, K. Ishizaki, J. Ceram. Soc. Jan. **102**, 299 (1994)

[111] M.L. Panchula, J.Y. Ying, J. Am. Ceram. Soc. **86**, 1114 (2003)

CHAPTER 5 - Sublimation growth of AlN Crystals

5.1 Self-seeded growth of AlN Crystals

Self-seeded growth of AlN starts from spontaneous nucleation. AlN crystal growth process by PVT occurs in several steps: (1) sublimation of source material, (2) mass transport of gas phase species, (3) adsorption of gas phase species on the growth surface, (4) nucleation, including surface diffusion and incorporation, and (5) desorption. The decomposition of AlN in higher temperature zone (source zone) is commonly assumed to proceed by the forward reaction of:

$$2AlN(s) \Leftrightarrow 2Al(g) + N_2(g) \qquad \textbf{(5-1)}$$

The temperature gradient established between source and seed provides the driving force for mass transport of gas phase species, then the crystals condensed in the lower temperature zone (crystal zone), which can be described reverse reaction of (5-1). The PVT growth of AlN crystals is typically performed in nitrogen atmosphere (partial pressure of N_2 gas is higher than that of the Al gas by several orders of magnitude). Since vapor transport is the rate limited step,[71,72] the growth rate is proportional to the flux of Al gas transported in the gas phase, thus proportional to the Al gas equilibrium partial pressure difference between the source and seed surfaces.

Figure 5.1 AlN crystal boule (l) and wafer (r)

In this study, as-received AlN powder was purified according to the methods described in earlier chapters before being used as the source of AlN crystal growth. The growth rate was determined by dividing the crystal mass change that occurred during growth by the growth time. After hours of growth, polycrystalline AlN boules with preferential (0001) orientation were obtained (Figure 5.1l); then the AlN wafer (Figure 5.1r) was produced by slicing the ingot and preparing the surface by grinding/lapping, which gives good geometrical parameter; mechanical polishing, which reduce the surface roughness; and chemical mechanical polishing, which is the best way to produce a surface without any scratches or surface damage

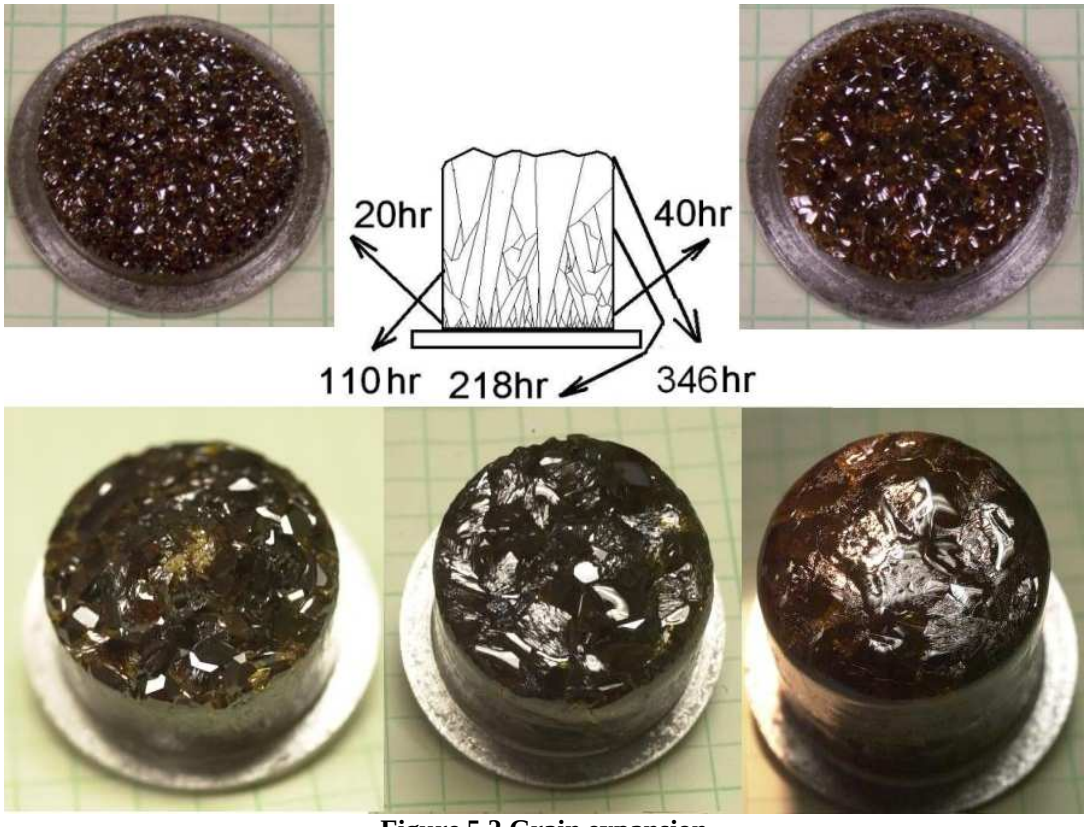

Figure 5.2 Grain expansion

Because of competition of neighboring grains during growth, some grains expanded, while other grains disappeared. Thus larger and larger grains were produced with growth (Figure 5.2). With only 20 hours of growth, the grains were tiny and their

density was high. With an additional 20 hours growth, the grain size increased, but were still small. After 110 hours, both the grain size and ingot height had obviously increased. With 218 hours of boule growth, grains 3mm x 5mm were apperent on the top of the ingot. With a total of 346 hour of growth, an AlN boule 27mm in height and 5mm x 8 mm in top size was obtained. By slicing the crystal boule along the *c*-axis, cross section of the crystal ingot can be studied. The top area of the boule had lighter color and fewer cracking compared to the bottom area of the boule.

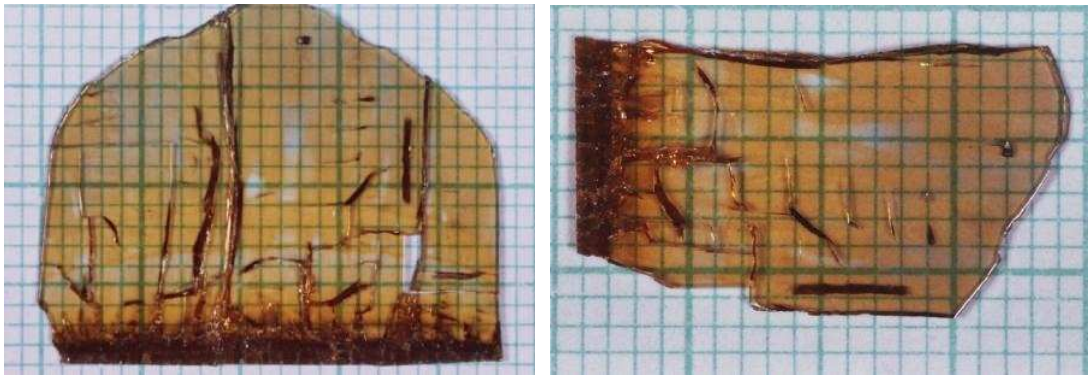

Figure 5.3 Cross section of AlN boule

The best condition for AlN bulk crystal growth by sublimation is the temperature and pressure that produces a growth rate approaching 100 micron/h. This requires a temperature above 2050 °C and a pressure of 400~500 torr. However, this condition always produces dark brown AlN crystals, presumably due to a high aluminum vacancy concentration. At a lower temperature and higher nitrogen pressure, the equilibrium nitrogen vacancy concentration may be much less. Therefore, annealing the crystals at a lower temperature (yet still high enough that solid state diffusion can take place) may reduce the alunimum vacancy concentration. Figure 5.4 shows the original source crystals (dark brown) and crystals after annealing at 1700°C and 960 torr for 24, 48, and 84 hours; the color changed from dark brown, toamber and light gold. After annealing 24 hours (Figure 5.4b), the bottom half of the AlN source changed color completely while

the top half of the AlN source retained its original dark brown color. There are new lighter color pyramid grains formed on the surface of the middle-up part of the AlN source, but not on the very bottom part. No prismatic single grains were observed but pyramid grains only. After annealing 48 hours, the source was lighter still in color (Figure 5.4c), but not obviously color change from the previous one. No single grains formed on the surface suggesting that the sources are all in the subliming zone where single grains are less likely to form. After annealing 84 hours (Figure 5.4d), the color was lighter than samples annealed for shorter times, but the change in color was not as pronounced. New pyramid shaped single crystal grains formed on the surface.

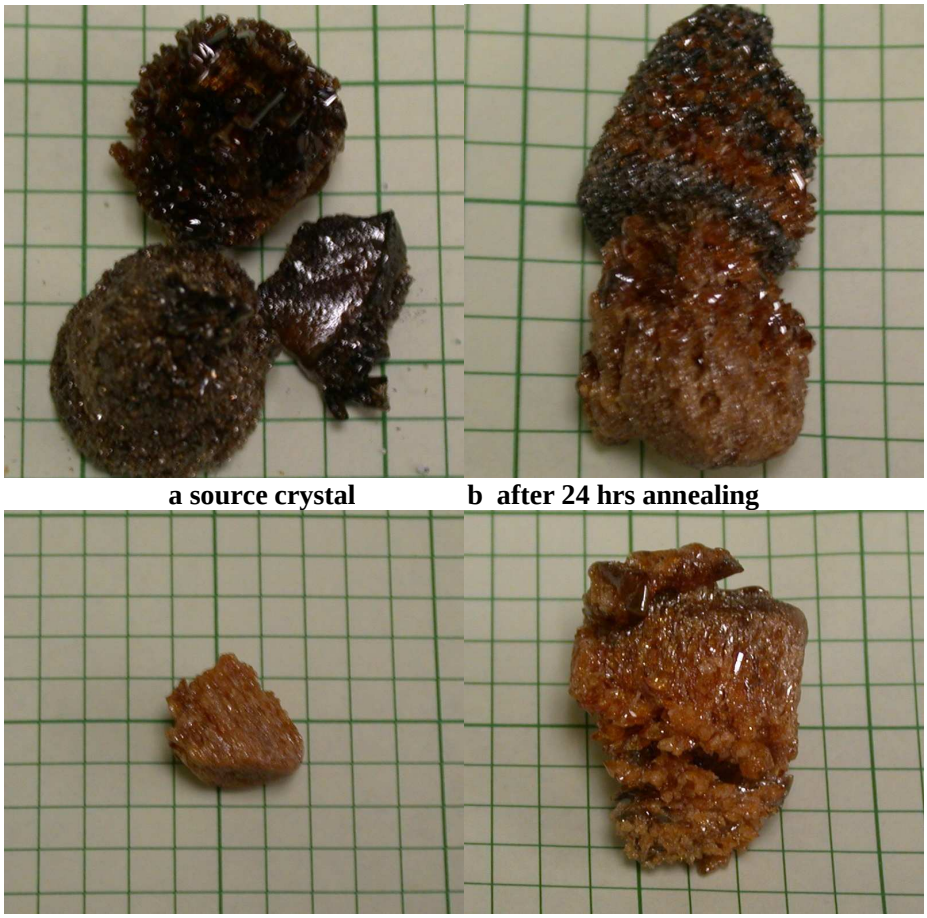

a source crystal **b after 24 hrs annealing**

c after 48 hrs annealing **d after 84 hrs annealing**

Figure 5.4 Source crystals and annealing after different time

5.2 Low Temperature AlN Crystal growth on SiC by PVT

L. Du[a], J.H. Edgar[a], J.K. Hite[b], J.D. Caldwell[b]

[a] *Department of Chemical Engineering, Kansas State University, Manhattan, KS 66506, USA*

b Electronics Science and Technology Division, Naval Research Lab, Washington, DC 20375

5.2.1 Introduction

Because of their superior properties[112], such as a wide direct bandgap (direct bandgap spanning from 0.8 to 6.1 eV), high breakdown voltage, high electron mobility, and high saturation velocity, group III nitride semiconducting compounds have become the basis for a multibillion dollar worldwide device market since 1990's. However AlGaInN device technology is limited by the lack of thermally and lattice matched substrates. Aluminum nitride is the most promising substrate for AlGaInN based device heterostructures, because it has small mismatches of physical properties with respect to AlGaInN materials, has a high resistivity, high thermal conductivity (is better at dissipating heat generated by devices), and is transparent in the UV range (does not absorb UV light generated by the device). It is especially well-suited for the UV optoelectronics including UV laser diodes (LDs) and RF power electronic applications which require aluminum-rich AlxGa1-xN layers.

AlN wafers/substrates are now produced from bulk AlN crystals that are grown by physical vapor transport (PVT) technique[113]. In recent years, several groups[112] have

independently developed processes and models for crystal growth of AlN by this technique. PVT can produce AlN bulk crystals of high quality and large sizes appropriate for use as substrates for Group III nitrides device technology. The process can be separated into self-seeded or seeded growth, depending on whether seed crystals are employed in the growth process. Further improvement of the PVT technique are needed, specifically concerning the perfection of the crystal quality (defects and impurities reduction, stoichiometry refinement) and enlargement of the crystal boule diameter.

The seeded PVT growth of AlN on SiC is a potential way to scale the process to large diameter crystals, since SiC substrates are available in diameter as large as 150 mm. and to control the polarity and orientation of AlN crystals. Balkas et al[114] reported the growth at temperature range of 1900 to 2250°C with Single-crystal 6H-SiC (0001) as substrates. The growth rate was 0.5 mm/h at 2150°C and 30–50 μm/hr at 1950 ~ 2050°C, but obviously SiC degradation and AlN crystal cracking were observed. Studies on 6H-SiC single crystal substrates were then reported by Edgar's group[115, 116, 117, 118, 119, 120, 121]. To avoid heavy degradation of SiC substrate, the growth temperature was typically around 1800°C. Both on-axis and 3.5° off-axis[115] 6H-SiC with silicon and carbon terminations were used. Crystal growth on as-received Si-terminated SiC were reported, while no growth was observed on C-terminated as-received SiC. AlN buffer layer was deposited by metal-organic chemical vapor deposition (MOCVD) prior to enhance the two-dimensional (2D) growth[115]. The method was modified to reduce the cracking in the following studies[116, 117], In addition to the AlN epilayer, an $(AlN)_x(SiC)_{1-x}$ alloy layer was introduced. The intermediate properties of the alloy layer helped reduce cracking in the overgrown AlN. The initial stages of AlN growth on SiC were studied[118]. AlN nucleated

as individual hexagonal hillocks and platelets, the grain size increased as the growth temperature was increased or growth temperature was decreased. The surface morphology and stress in AlN crystals grown on SiC substrates were also characterized[119, 120]. AFM images revealed scratches and steps on as-received 6H-SiC substrates, which served as nucleation sites for individual AlN grains grown in a three-dimensional mode sublimation from a source mixture of AlN-SiC powders. Surface morphology varied across the sample, from flat surfaces to regions with large steps (120 nm) separated by large terraces (up to 5 μm). For comparison[121], Self-seeding produces crystals of the highest perfection, lowest stress, and low Si and C impurity content, but the crystals grow in random crystallographic orientations; while AlN crystals seeded on 6H-SiC(0001) have a single crystallographic orientation and the largest dimensions are perpendicular to the c-axis, determined by the size of the substrate. Cracking and voids in the AlN layer produced by differences in thermal expansion coefficients of AlN and SiC and decomposition of the SiC were ameliorated by depositing an AlN–SiC alloy layer on the SiC before growing the AlN layer. Epelbaum et al.[122] studied AlN crystal growth on SiC with different orientations. At seed temperature of 2000°C in 350 mbar N2 pressure, AlN layers were obtained in the thickness of of 200–500 μm. Hexagonal hillocks were obtained from the growth on Si-face, c-plane SiC substrates; whereas, growth on a-plane substrates resulted in more stable growth showing a smooth morphology. Non-polar AlN single crystals growth on m-plane SiC was also reported[123]. Stacking faults initiated from the interface toward the growth surface in AlN/SiC (1−100), the dislocation density decreases up to $5 \times 10^4/cm^2$ at the thickness of 10 mm.

However, substrate stability and crystal cracking are still the major drawbacks for seeded AlN growth on SiC substrates. Although AlN bulk crystal growth can be achieved at temperatures as low as 1800 °C, obviously grain size expansion was reported at a growth temperature around 2000 °C.[124] As such a high process temperature, SiC substrates readily decomposed. Meanwhile, the difference in thermal expansion between AlN and SiC results in the cracking of the AlN layers. Recently, Chemekova *et al*[125] used a SiC substrate to scale the process of bulk single AlN crystals boule from 15 mm in diameter to 2-inch in diameter. Another study reported the fabrication of stress-free AlN single crystal wafers by the assistance of 2H-SiC pyramids on the 4H-SiC substrate[126]. First at about 1400 °C, asymmetric hexagonal pits formed on the SiC substrate due to thermal etching at the emergence of threading dislocations. Then at about 1800 °C, an AlN–SiC alloy nucleated inside the pits. As growth proceeds, hexagonal hillocks develop on the filled etch pits and later convert to hexagonal pillars. At 400 mbar, the AlN first expands in the direction perpendicular to the c-axis results in disklike tablet, and then form microrods. Finally, hexagonal microrods with six nonpolar {1-100} planes as side facets form on the pyramids with 30° rotation in respect to the pyramid facets in a plane parallel to the (0001) SiC substrate. For a longer growth time, the AlN microrods coalesce and yield an AlN layer, which can be easily separated from the underlying hexagonal pyramids.

This study addresses the challenging issues involved in PVT growth of AlN on SiC substrates including SiC degradation and the impacts of the SiC orientation and tilt direction on nucleation and orientation of the AlN. Based on former thermodynamics analysis, the AlN was grown at relatively low temperature (no higher than 1650 °C) on

SiC substrates with different orientation, tilt, and face, to limited SiC decomposition. Oxygen impact was also investigated. The as received AlN powder with oxygen concentration of 0.9wt% and bulk polycrystals with oxygen concentration of about ~10^{18} cm^{-3} were used as the sources.

5.2.2 Experimental

The aluminum nitride crystals were grown at low temperature on SiC substrates in a resistively-heated tungsten furnace with vertical temperature gradient of about 5 °C /cm. The source and substrates were placed in a covered tungsten crucible within a covered tungsten retort. The distance between the source zone and the crystal growth zone was maintained as 1 cm. As received AlN powders (about 1 wt% oxygen) and polycrystalline AlN crystals (<10^{-5} wt oxygen?) were used as sources. Substrates types include both Si-terminated and C-terminated c-plane 4H-SiC with on axis, 8^o off (11-20) and 7^o off (1-100) orientations, and m-plane 6H-SiC.

The sources were baked in a 5% hydrogen and 95% argon gas mixture at 1000°C for about 1 hour to reduce the surface oxide before the experiment. The growth temperature was measured by an optical pyrometer focused on the top of the retort. Ultra high purity nitrogen was used as ambient gas, and the growth time was varied from 2 to 30 hours. In order to minimize the thermal etching of the SiC substrate, the highest growth temperature in the study was 1650 °C. The lowest growth temperature was the minimum at which AlN crystals could be observed at a magnification of 1000x at desired pressure after 2 hours growth. Based on the results of this study, the grwoth temperature varied from 1432 °C to 1650 °C and the growth pressure varies from 125 torr to 888 torr.

Electron channeling contrast imaging (ECCI) was used to identify the dislocations types and density in the AlN crystal. This technique has demonstrated the ability to image screw or mixed dislocations in GaN and SiC[127]. This nondestructive approach can employ a commercial scanning electron microscope (SEM) coupled with diode detectors to collect electrons backscattered or forescattered from a crystalline specimen. When the crystal specimen is tilted near a Bragg angle, strong fluctuations in the backscattered forescattered electron yield are created due to the localized bending of lattice planes by the individual dislocations. These variations in electron yield are registered as dark/ bright intensity fluctuations in the resulting backscattered/ forescattered electron images. The sum of these fluctuations could provide a value for the total dislocation density, if in fact all dislocation types are imaged by ECCI.

5.2.3 Results and Discussion

AlN crystals growth through PVT can be enhanced by increasing temperature or decreasing pressure[118, 128]. With two hours growth, obviously AlN grains were observed under 1000x microscope with temperature as low as 1432 °C and pressure as high as 888 torr. Most AlN crystals appeared as individual platelets or coalesce with neighbor gains. At the investigated temperature range (1432 ~ 1650 °C), AlN crystals lateral expanding that perpendicular to the *c*-plane were promoted under growth enhancing condition or with longer growth time, and then form the continuous AlN film on the SiC substrate. SiC thermal etch pits can still be observed under 1000x microscope for the samples grown at temperature higher than 1520 °C. For the samples growth at temperature lower than 1480 °C with polycrystalline AlN as source, the thermal etch pits were scarcely observed under 16000x SEM.

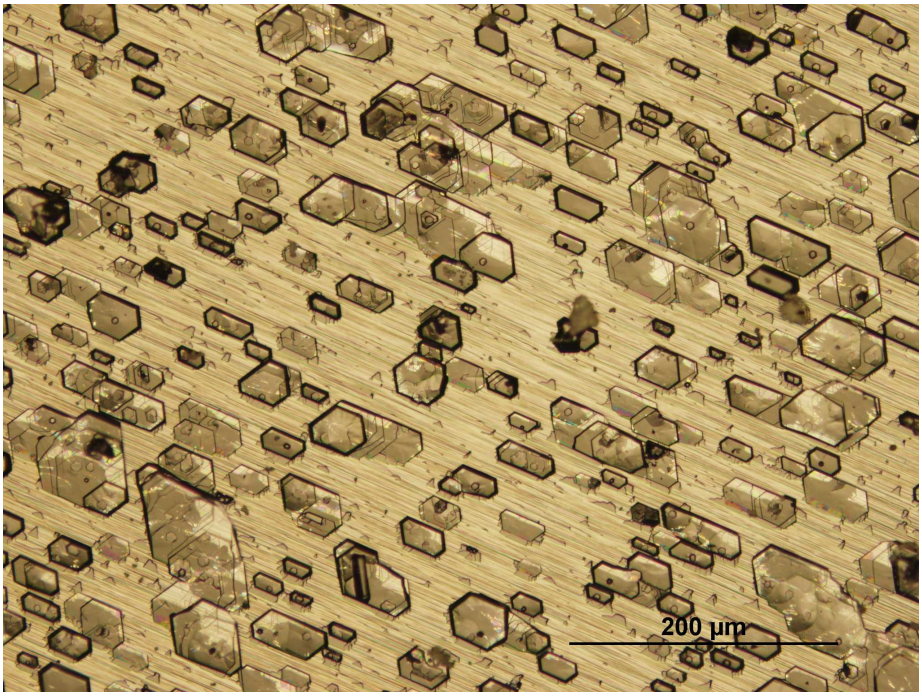

a, AlN crystals originated from polycrystalline source on SiC

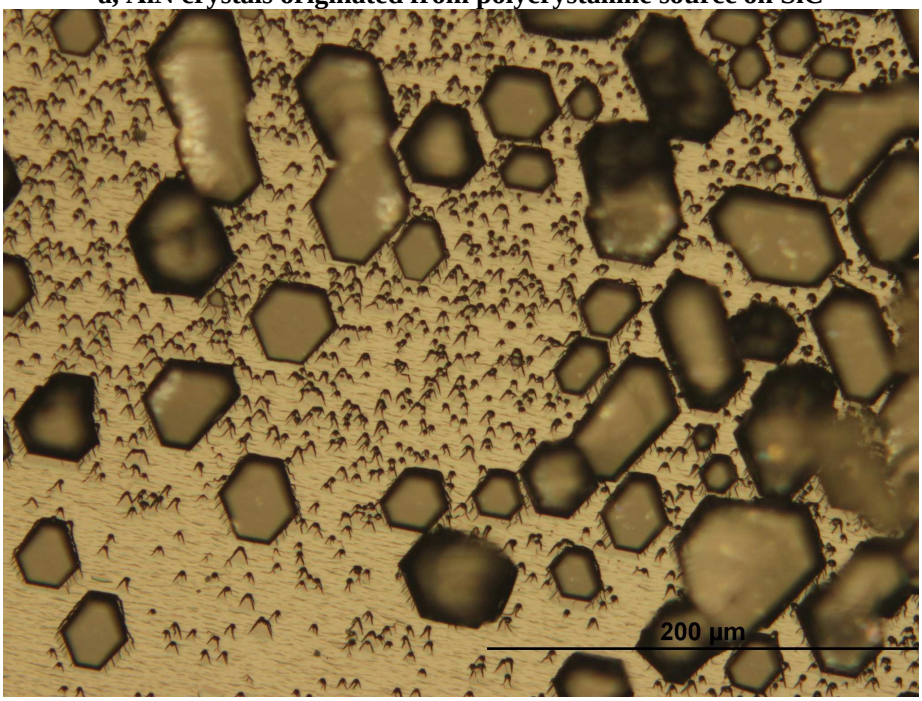

a, AlN crystals originated from powdersource on SiC

Figure 5.5 Optical photos of AlN crystal on Si-SiC seeds at 1620 °C

5.2.3.1 Source comparison

The different between two types of sources employed in the study are their morphology and oxygen content. Powder source is composed of small particles that are less than 1–2 mm in diameter. It has the highest oxygen concentration (~0.9 wt%) among all kind of AlN sources. The crystal source is bulk polycrystalline AlN ingot produced from previous study with oxygen concentration of about ~10^{18} cm^{-3}.

After 2hour's growth at 1620 °C and 780 torr on same SiC substrates, hexagonal shaped AlN tablets formed on substrates surface on both types of samples (Figure 5.5). Thermal etch pits and surface steps were observed on SiC under optical microscope. And their crystal grain size is similar from about 15 micron to about 50 micron. Samples originated from O-rich source had obviously much more thermal etch pits on substrate. When the growth temperature reduced to 1520 °C, after 2hour's growth at 780 torr on same SiC substrates, the samples from different source presented different morphology. With polycrystalline AlN as source, the obtained crystals were hexagonal tablets shaped with size varying from bigger than 20 micron to smaller than 1 micron. The grain distribution was uniform, and thermal etch pits can be found under most of the crystals. While the crystals nucleated from powder source were more localized. The sample surface was covered with massive tiny pyramids. The hexagonal shaped crystal density was much lower than the sample grew at same condition but from crystal source. And their substrates surface was great etched than that on crystal source samples. Figure 5.7 are the EDS studies on specific point and selected areas of these pyramids on O-rich source sample, indicating the composition of the pyramids were more like the mixture of SiC and AlN, which was similar to that Yazdi's report[126].

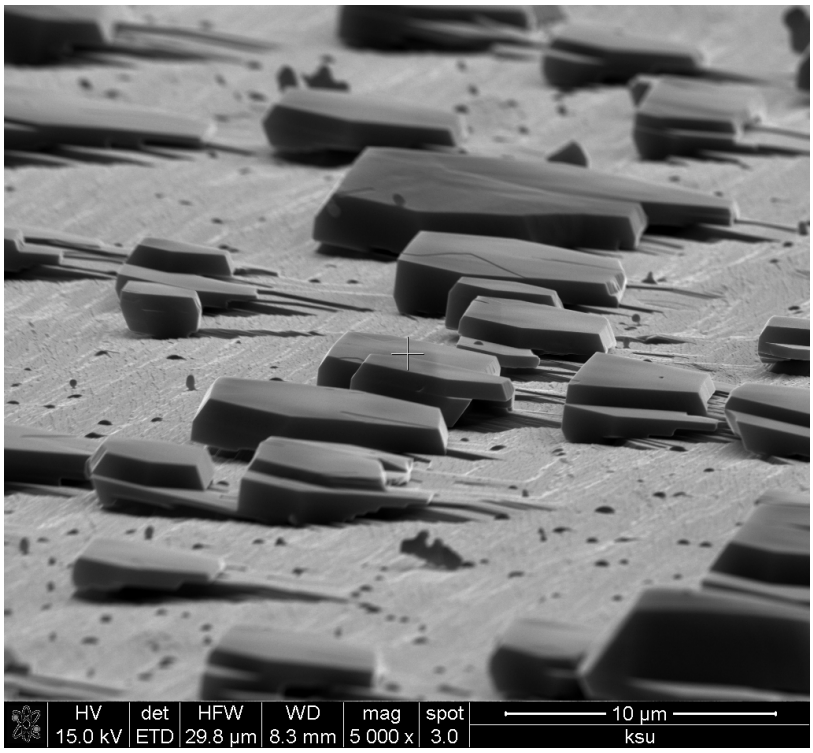

a, AlN crystals originated from polycrystalline source on SiC

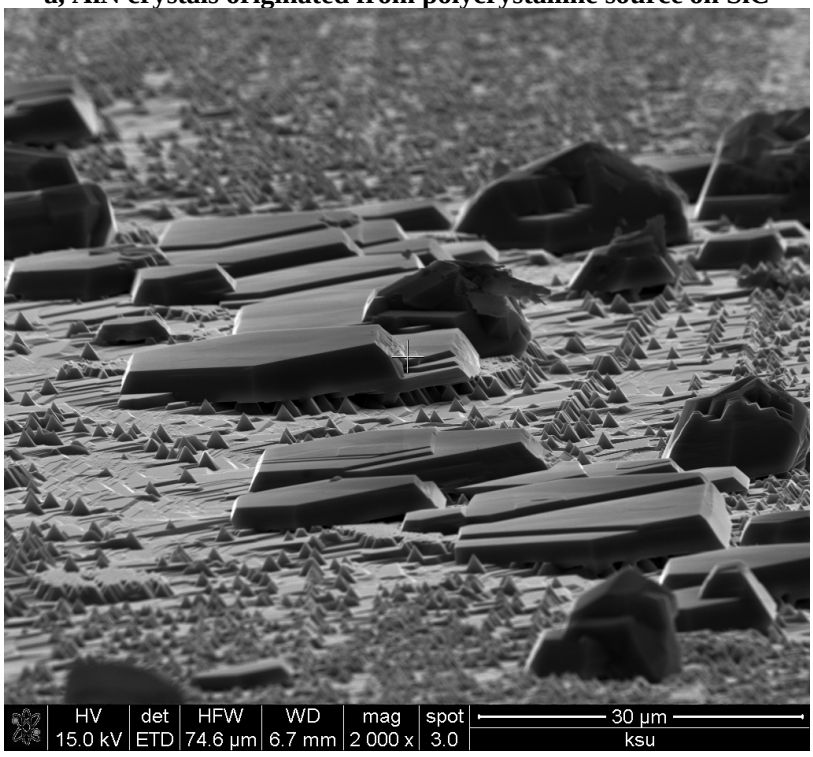

b, AlN crystals originated from powder source on SiC

Figure 5.6 SEM photos of AlN crystals on SiC with different sources at 1520 °C

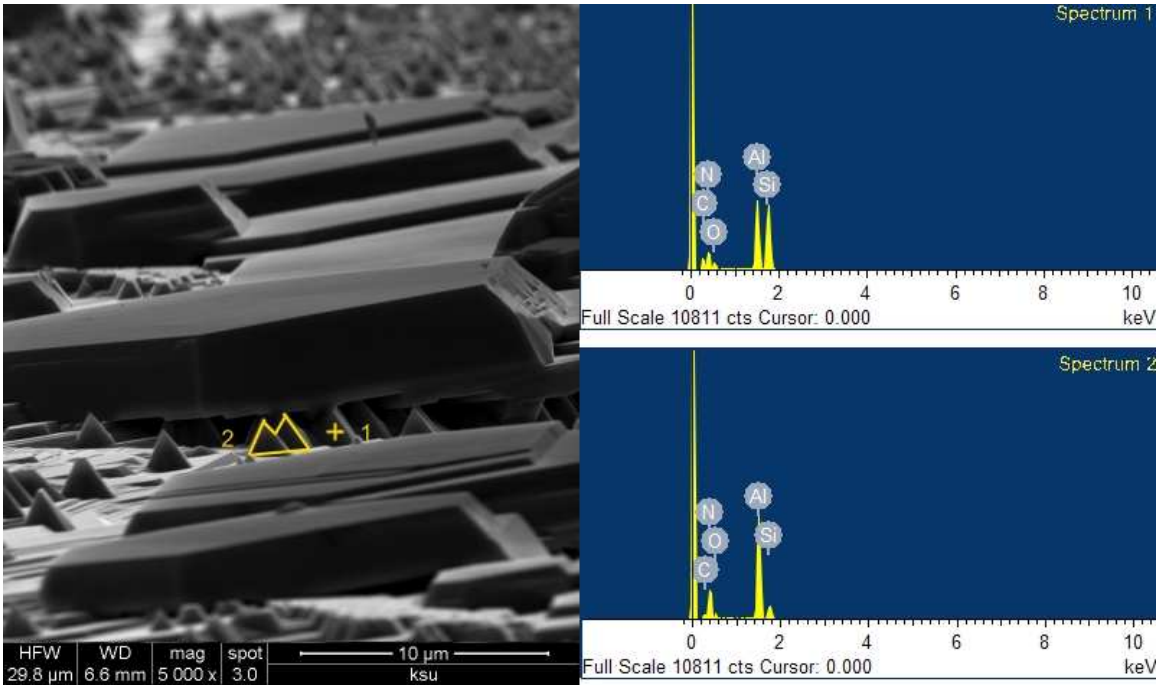

Figure 5.7 EDS on selected area of AlN on SiC grown from o-rich source

Then the growth temperature and growth pressure was reduced to about 1440 °C and 622 torr. The morphology of the samples originated from different sources is totally different. For AlN grown on Si-face of c-plane 8^{o} off (11-20) SiC for 24 hours, the crystals formed tilted thin hexagonal tablets with c-axis parallel to the substrates c-axis. No thermal etch pits were observed under 16000x SEM (Figure 5.8a). The SiC decomposition was greatly reduced. However, SiC substrates were for the sample from O-rich powder source were heavily etched (Figure 5.8b). Deep hexagonal thermal etch pits and holes were observed on the surface. The continuous film was formed and covered majority area of the O-rich source samples, and the thickness of the film was bigger than that of the tablets on crystal source samples, implying higher growth rate for samples originated from O-rich source. Even with a shorter growth of 4 hours at same condition for O-rich source, SiC substrates are still heavily etched (Figure 5.8c). Although there were single crystal grains, the continuous film was also formed and the

crystal surface coverage of this sample was still higher than sample from crystal source. EDS mapping for samples from O-rich source confirmed that both crystal tablets and continuous films are AlN. Hexagonal pyramids can only be found on the samples from O-rich source and EDS mapping on area covered with massive pyramids showed extremely high concentration with Si and C. However, most of the pyramids are symmetric in stead of unsymmetrical tilted shape[126]. On the area deposited with hexagonal pyramids, the crystal grains originated from these pyramids and covered them.

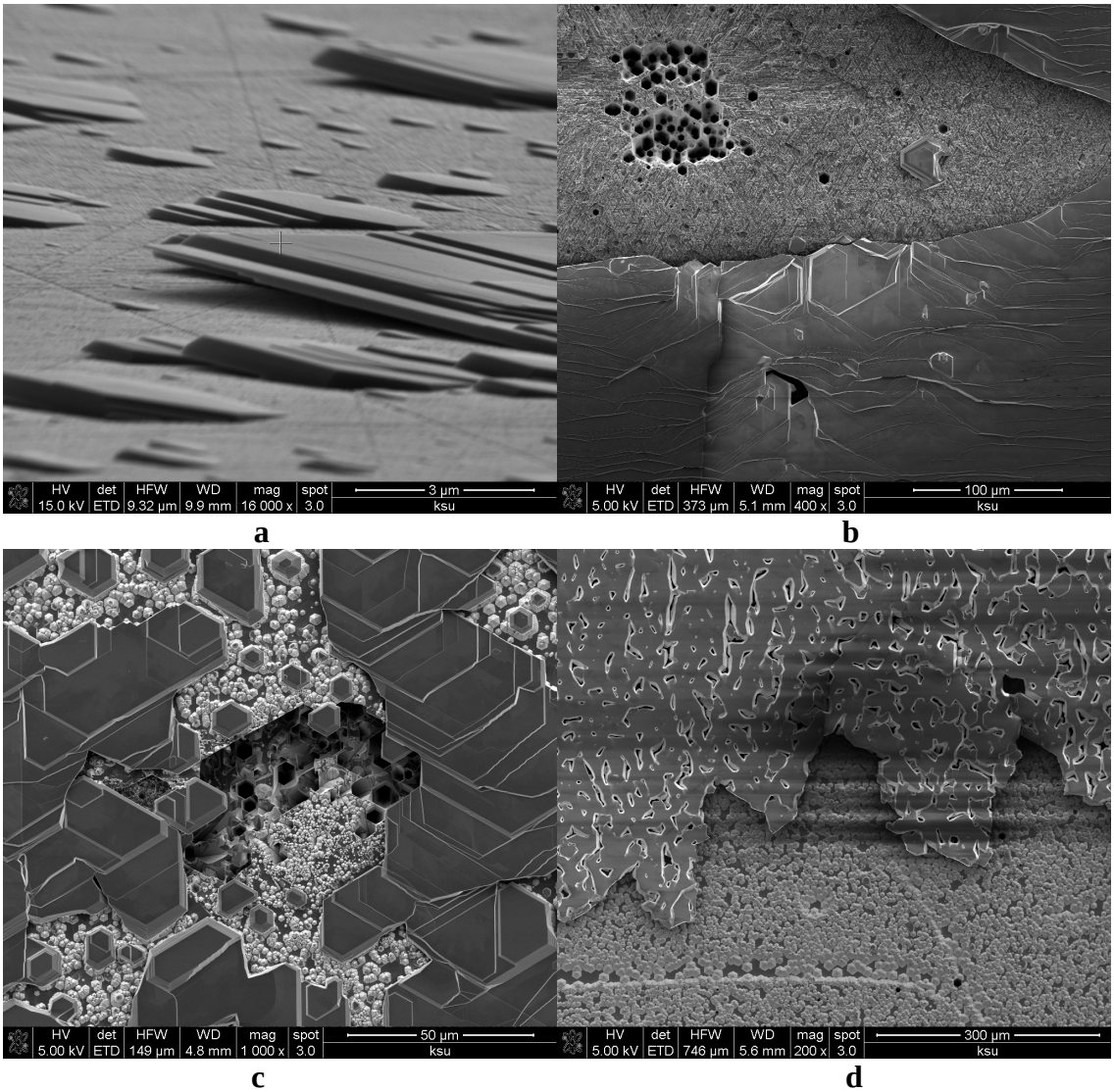

Figure 5.8 SEM photos of AlN crystals on SiC with different sources at 1440 °C
a, AlN crystals originated from polycrystalline source on SiC. b, c, d, AlN crystals originated from powder source on SiC. a, b, d, growth for 24 hours. c, growth for 4 hours.

Obviously, oxygen increases the SiC degradation. The source for AlN crystal growth on SiC substrates should be purified to minimize the oxygen in order to minimize the SiC decomposition. In addition, the present of oxygen enhances AlN crystal growth. It was agreed with our previous thermodynamic study and literature[105] that oxygen promotes Al transport to seed at temperature lower than ~2000 K.

5.2.3.2 Substrate face and tilt directions comparison

4H-SiC substrates were studied mainly on c-plane (0001) orientation both Si-terminated and C-terminated but different tilt directions, including 8^{o} off (11-20) SiC (titled to the corner of hexagon, Figure 5.9), 7^{o} off (1-100) SiC (titled to the edge of hexagon, Figure 5.10l), on -axis SiC (Figure 5.10r). The diagram of planes and directions can be found in Figure 2.5. As etch pits can still formed on the SiC at a growth temperature of 1520°C above or with O-rich source, the growth temperature in this section was reduced to 1432 °C ~ 1440°C, the growth pressure was 600 torr ~ 620 torr, the growth source was polycrystalline AlN and the growth time was 24 ~ 30 hours. Later growth of the AlN dominated from the crystal nucleation to the film formation.

The crystals were successfully deposited on both Si- face and C-face for the same substrate, but the nucleation coverage on the C-face is much lower than that on the Si-face (Figure 5.9). Nucleation preferentially occurs at scratches on the substrates, resulting in many crystals following the scratches on both Si- and C- terminated SiC substrates. The nucleated crystal grain tilt directions were clearly affected by the substrate tilt directions. Although the crystals were all deposited on c-plane SiC, the obtained crystal *c*-axis is always tilted to same direction with substrate *c*-axis; therefore the growth surface of the grains is always parallel to the *c*-plane. If the substrates are off axis, the

growth surface of the crystal then has angle with the substrate surface; crystal grains nucleated on 8^{o} off (11-20) interacted the growth substrates on the hexagon corner and crystal grains nucleated on 7^{o} off (1-100) interacted the growth substrates on the hexagon edge (Figure 5.11). If the substrate are on-axis, no angle was observed between growth surface and substrate surface (Figure 5.10r).

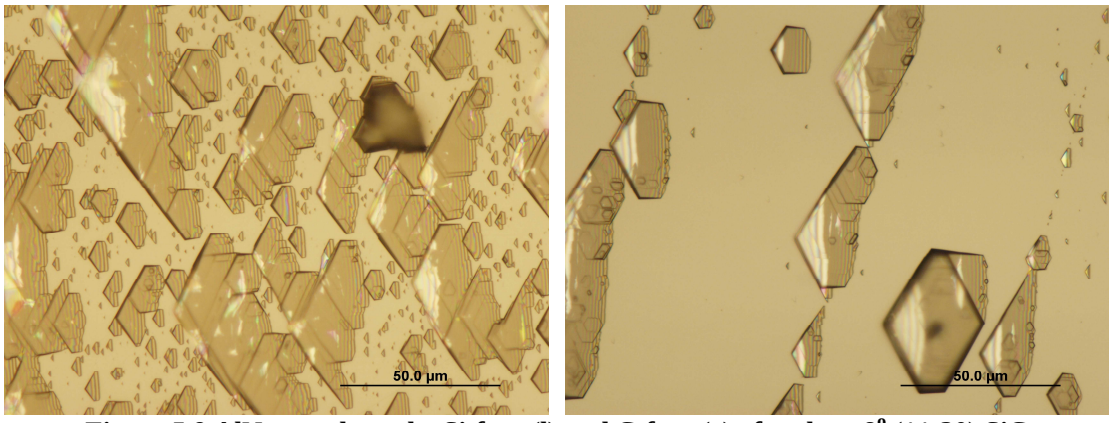

Figure 5.9 AlN growth on the Si-face (l) and C-face (r) of c-plane 8^{o} (11-20) SiC

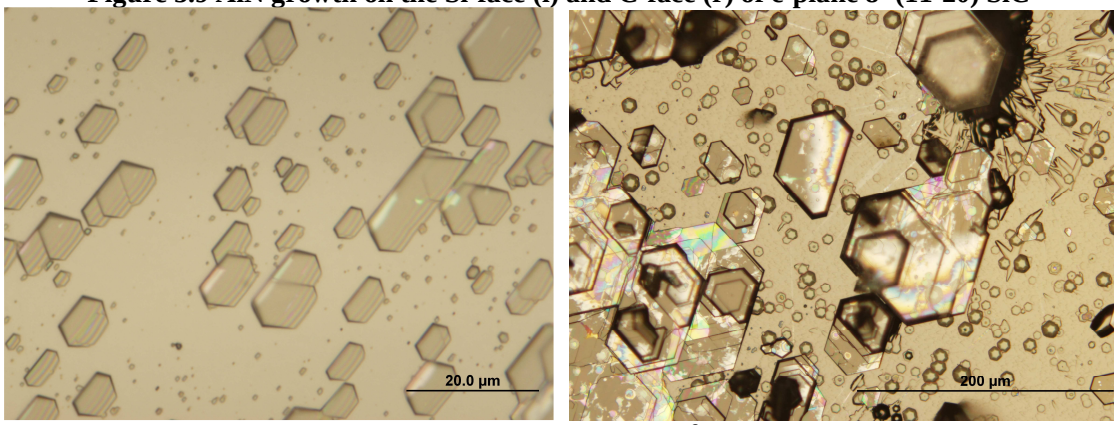

Figure 5.10 AlN growth on c-plane Si-face SiC 7^{o} (1-100) (l) and on-axis(r)

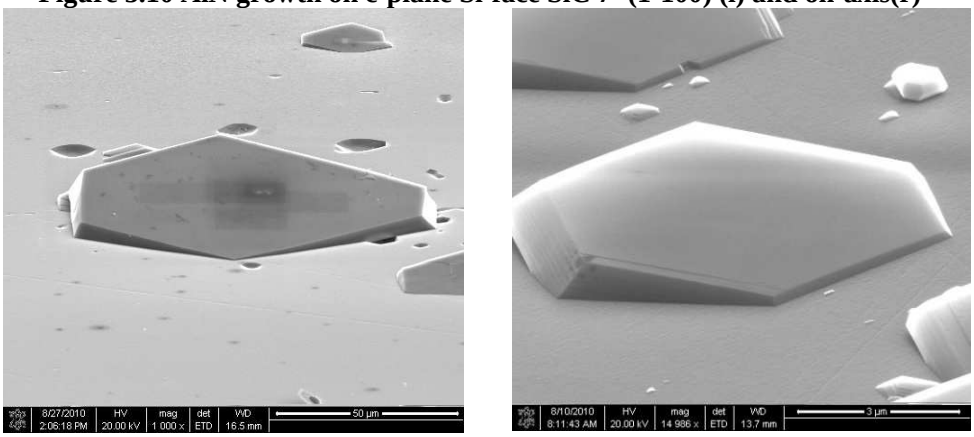

Figure 5.11 AlN on the c-plane Si-face SiC 8^{o} (11-20) (l) and 7^{o} (1-100) (r)

ECCI was used to identify the dislocations for the sample deposited on 8^{o} off (11-20) and 7^{o} off (1-100) 4H-SiC substrates. For the previous substrate, Flatter areas, far from the spiral are generally defect-free. Spiral areas show more dislocations. The edge growing off of the SiC substrate is highly defective. The etch pits density was in the range of $10^{6}cm^{-2}$. For the later substrate, the areas where dislocations were indicated were localized with etch pits density was in the range of $10^{8}cm^{-2}$

5.2.3.3 Substrate Orientation comparison

C-plane and *m*- plane orientation 6H-SiC was used as substrate in the experiment. Three growth temperatures of 1440 °C, 1520 °C, and 1620 °C were tested. At growth temperature of 1520 °C and 1620 °C, pressure of 780 torr, after 2 hours growth very few crystals but etch pits were found on the sample, and they didn't follow the orientation with the substrate. At growth temperature about 1436±12°C and a pressure of about 820 torr, after 24 hours growth, hexagonal AlN grains were obtained. The growth rate along the *a*-axis is higher than that along the *c*-axis, resulting hexagonal tablet shaped grains. The crystals have multiple orientations including *c*-axis parallel to the substrates, *c*-axis perpendicular to the substrates, and *c*-axis interacted with substrates (Figure 5.12). After 40 hours growth at similar temperature and pressure conditions, more and more crystals have orientation of c-axis parallel to the substrate. Figure 5.13 are the SEM photos on the top view (l) and cross section view (r) of the sample, and hexagonal tablets with diagonal size more than 100 micron were obtained. After 48 hours growth at 1448°C and 820 torr, *c*-axis parallel to the substrates became the major orientation of the sample (Figure 5.14). Crystals expanded with a higher growth rate along *a*-axis than that along the *c*-axis.

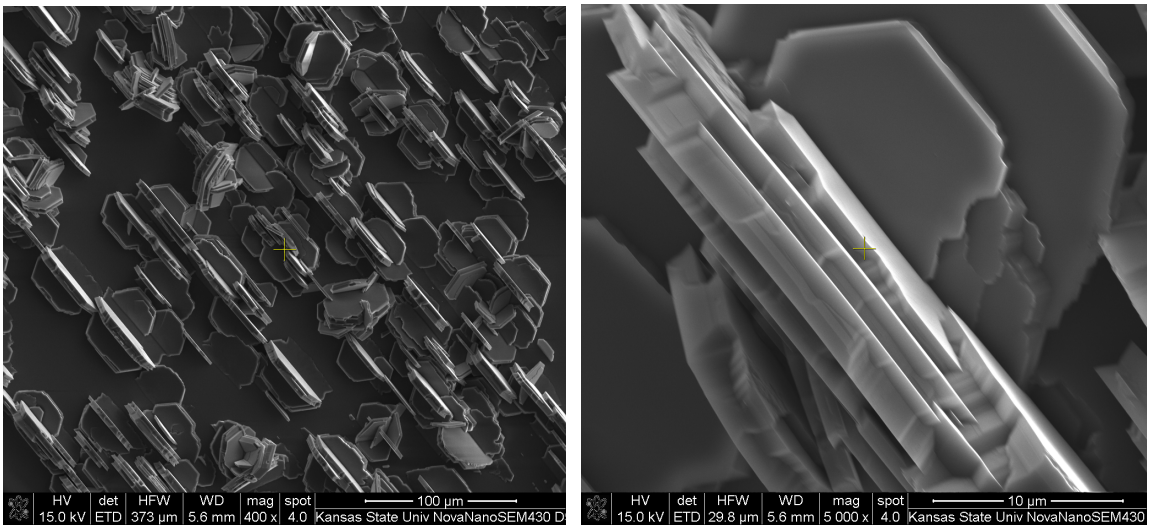

Figure 5.12 AlN growth on m- plane SiC 24 hours at about 1440 °C

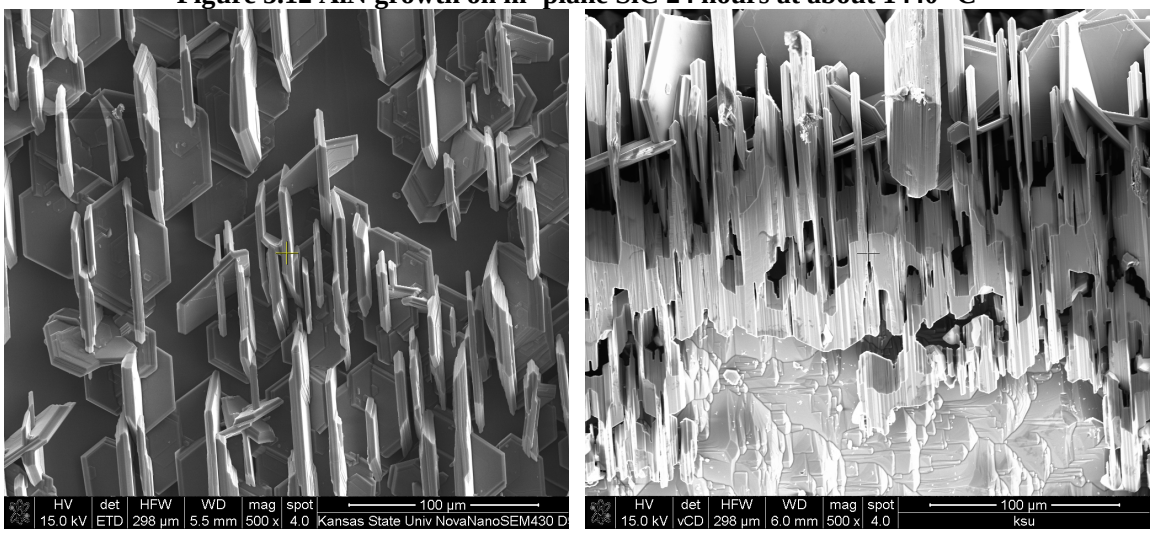

Figure 5.13 AlN on m-plane SiC 40 hrs; top view (l) and cross section (r) at 1440 °C

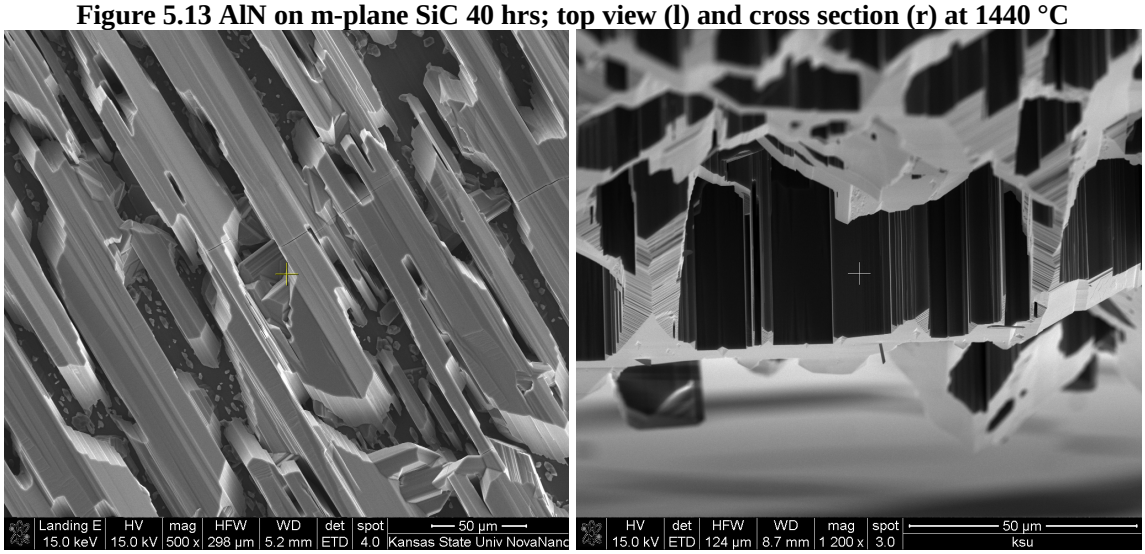

Figure 5.14 AlN on m-plane SiC 48 hrs; view (l) and cross section (r) at 1440 °C

5.2.4 Conclusion

SiC are thermally etched at temperature higher than 1520 °C, and the AlN grown at this temperature or above tend to crystallize from the etch pits At growth temperature of about 1440 °C (1432 ~1460°C), no etch pits were found for samples originated from polycrystalline AlN. The crystals had a relative uniform distribution over the substrates. The use of O-rich AlN powder source in the growth increases the SiC decomposition and promotes Al transport. The substrates were heavily etched even at conditions in which no thermal etching was found in the growth with very low oxygen-containing source. However if the substrate surface was scratched, crystals tend to nucleate from these scratches. As a result, low temperature growth with low oxygen concentration source is more effective to protect SiC substrate from thermal etching. The AlN crystals can be deposited on both Si-face and C-face of *c*-plane SiC, as well as *m*-plan SiC substrates. The growth surface of grains is always parallel to the c-plane. The grains tend to have same tilt with the substrate. However, the growth conditions for *m*-plan SiC is very critical. Continuous AlN crystals growth on *m*-plane SiC was achieved at 1428 ~1460 ˚C and 600 torr. Very few irregular crystals but etch pits was found at same pressure but temperature higher than 1520 ˚C; therefore, low temperature growth is more effective for m-plan SiC.

5.3 References

[112] Dirk Ehrentraut and Zlatko Sitar, Advances in bulk crystal growth of AlN and GaN, MRS Bulletin, , **34**, 259, (2009)

[113] Tomohisa Kato, Ichiro Nagai, Tomonori Miura, Hiroyuki Kamata, Kunihiro Naoe, Kazuo Sanada, and Hajime Okumura, AlN bulk crystal growth by sublimation method, Phys. Status Solidi C **7,** 1775, (2010)

[114] C. M. Balkas, Z. Sitar, T. Zheleva, L. Bergman, R. Nemanich, R. F. Davis, Sublimation growth and characterization of bulk aluminum nitride single crystals, J. Cryst. Growth 179, 363, (1997)

[115] Y. Shi, Z. Y. Xie, L. H. Liu, B. Liu, J. H. Edgar, M. Kuball: *Influence of buffer layer and 6H-SiC substrate polarity on the nucleation of AlN grown by the sublimation sandwich technique*, J. Cryst. Growth **233** (2001) 177-186

[116] Twigg, Picard, Caldwell, Eddy Jr., Mastro, Holm, Neudeck, Trunek, and Powell, Jour.of electro. Materi., **39**, 6, (2010)

[117] Y. Shi, B. Liu, L. Liu, J. H. Edgar, H. M. Meyer III, E. A. Payzant, L. R. Walker, N. D. Evans, J. G. Swadener, J. Chaudhuri , Joy Chaudhuri, *Initial nucleation study and new technique for sublimation growth of AlN on SiC substrate*, Phys. Stat. Sol. (a) **188**,757, (2001)

[118] B. Liu, Y. Shi, L. Liu, J. H. Edgar, D. N. Braski, *Surface morphology and composition characterization at the initial stages of AlN crystal growth*, Mat. Res. Soc. Symp. Proc. **639**, G3.13.1 (2001)

[119] L. Liu, B. Liu, Y. Shi, J. H. Edgar: Growth mode and defects in aluminum nitride sublimed on (0001) 6H-SiC substrates, MRS Internet J. Nitride Semicond. Res. **6** 7.1, (2001)

[120] L. Liu, D. Zhuang, B. Liu, Y. Shi, J. H. Edgar, S. Rajasingam, M. Kuball, Characterization of aluminum nitride crystals grown by sublimation, Phys. Stat. Sol. (a) **188**769, (2001)

[121] J. H. Edgar, L. Liu, B. Liu, D. Zhuang, J. Chaudhuri, M. Kuball, S. Rajasingam: Bulk AlN crystal growth: self-seeding and seeding on 6H-SiC substrates, J. Cryst. Growth **246**, 187, (2002)

[122] B. M. Epelbaum, M Bickermann, A Winnacker: Seeded PVT growth of aluminum nitride on silicon carbide, Mater. Sci. Forum 433-436, 983-986 (2003)

[123] Issei Satoh, Satoshi Arakawa, Keisuke Tanizaki, Michimasa Miyanaga, and Yoshiyuki Yamamoto, *Sublimation growth of nonpolar AlN single crystals and defect characterization*, Phys. Status Solidi C **7**, 1767, (2010)

[124] Z. Gu, L. Du, J. H. Edgar, N. Nepal, J.Y. Lin, H.X. Jiang, R. Witt, *Sublimation growth of aluminum nitride crystals*, J. Cryst. Growth **297**, 105–110 (2006)

[125] T. Yu. Chemekova, O. V. Avdeev, I. S. Barash, E. N. Mokhov, S. S. Nagalyuk, A. D. Roenkov, A. S. Segal, Yu. N. Makarov, M. G. Ramm, S. Davis, G. Huminic, and H. Helava, *Sublimation growth of 2 inch diameter bulk AlN crystals*, phys. stat. sol. (c), 1–3 (2008)

[126] G. R. Yazdi,a┌ M. Beckers, F. Giuliani, M. Syväjärvi, L. Hultman, and R. Yakimova, Freestanding AlN single crystals enabled by self-organization of 2H-SiC pyramids on 4H-SiC substrates, Appl. Phys. Lett. **94**, 082109 (2009)

[127] M.E. Twigg, Y.N. Picard, J.D. Caldwell, C.R. Eddy Jr., M.A. Mastro, R.T. Holm, P.G. Neudeck, A.J. Trunek and J.A. Powell, *Diffraction Contrast of Threading Dislocations in GaN and 4H-SiC Epitaxial Layers Using Electron Channeling Contrast Imaging*, J. Elect. Mater., **39**, 6, (2010)

[128] L. Liu and J. H. Edgar, Transport effects in the sublimation growth of aluminum nitride, J. Cryst. Growth **220**, 243, (2000)

CHAPTER 6 - Sublimation Growth of TiN Crystals

Published in J. Mater. Sci.: Mater. Electron, **21** (2009)78-87.

Li Du and J.H. Edgar, Department of Chemical Engineering, Kansas State University, Manhattan, KS 66506, USA

Edward A. Kenik and Harry Meyer III, High Temperature Materials Laboratory, Oak Ridge National Laboratory, Oak Ridge, TN 37831

Abstract

The sublimation-recondensation growth of titanium nitride crystals with N/Ti ratio of 0.99 on tungsten substrates is reported. The growth rate dependence on temperature and pressure was determined, and the calculated activation energy was 775.8±29.8kJ/mol. The lateral and vertical growth rates changed with the time of growth and the fraction of the tungsten substrate surface covered. The orientation relationship of TiN (001) || W (001) with TiN [100] || W [110], a 45^{o} angle between TiN [100] and W [100], occurs not only for TiN crystals deposited on (001) textured tungsten but also for TiN crystals deposited on randomly orientated tungsten. This study demonstrates that this preferred orientational relationship minimizes the lattice mismatch between the TiN and tungsten.

Keywords: TiN, sublimation growth, tungsten substrate, activation energy, orientation

6.1 Introduction

Transition metal nitrides such as ScN and TiN, are attractive candidates for combining as layered structures or alloys with gallium nitride and related group III nitride semiconductors, because they can have similar lattice constants, share a common element and exhibit dual properties characteristics of both covalent compounds and metals[129]. Usui *et al*[130] studied the role of a TiN layer in GaN epitaxial growth and crystal quality in a void-assisted separation method. The small GaN islands that formed on the TiN nano-net in the beginning of epitaxy have crystal facets that introduce dislocation bending and reduce the threading dislocation density in the GaN layer. Thus, the TiN layer separates the GaN layer from the substrate and improves the crystal quality. Chen *et al*[131] employed TiN as a reflective layer between the GaN device layer and its silicon substrate. This improved the efficiency of GaN light emitting diodes compared to those grown directly on silicon. More recently, Oliver *et al*[132] used a composite ZrN/AlN layer on silicon for similar purposes. The ZrN reduced the light lost by reflecting it away from the substrate and facilitated electrical contact formation. Moram *et al*[133] investigated nitride layers of zirconium, hafnium, niobium, chromium, and scandium on silicon to block the threading of dislocations in the epitaxial gallium nitride. Scandium nitride layers were the most effective at reducing the GaN dislocation density to a minimum value of 3×10^7 cm^{-2}. Bulk ScN crystals have also been proposed as a substrate for gallium nitride, due to its small lattice constant mismatch, -0.1%[134]. Furthermore, epitaxial growth of TiN was investigated on Si and GaAs substrate[135]. Both orientation relationships of TiN [001] || GaAs [110] and TiN $[1\bar{1}0]$ || GaAs $[\bar{1}10]$ have been found for TiN growth on GaAs (001).

In addition, titanium nitride is a major industrial material because of its excellent properties, including abrasive wear resistance, good lubricating characteristics and low diffusivity. This latter characteristic makes it a good diffusion barrier between Si and Al, Si and Ag, and Ti and Pt[136] . Titanium nitride belongs to the Fm3m space group and has a rock salt structure (lattice constant 4.240 Å), which is an FCC crystal structure with all octahedral interstitial positions occupied. TiN_x is stable in the composition range of $TiN_{0.6}$ to $TiN_{1.1}$, with nitrogen atom vacancy concentrations up to 50 atomic %[136]. The high melting point (2930˚C)[137], extreme hardness (2000kg/mm^2)[138], good resistance to wear and corrosion, as well as the high phase stability (thermodynamic, metallurgical and chemical), of TiN results from the covalent nature of the Ti-N bonds, and its rock salt crystal structure[139], while its relatively low thermal conductivity (19.2 W/m·˚C)[136], compared to Cu (401 W/m·˚C)[140], AlN (285 W/m·˚C) or GaN (130 W/m·˚C)[141], and low electrical resistivity (20±10 μΩ·cm)[136] are from its metallic characteristics.

Although physical vapor deposition methods are typically employed to prepare TiN thin films to ensure a low thermal budget[142], many other methods have also been used including chemical vapor deposition with $TiCl_4$ and NH_3 [143] or $TiCl_4$-N_2-H_2 mixtures[144] , reactive sputtering Ti metal in an Ar/N_2 gas mixture[145] , evaporation and laser physical vapor deposition. To produce bulk crystals, sublimation growth, one of the physical vapor transport growth methods, is an attractive approach, as it has higher growth rates, morphological stability and is an easily implemented process, and produces crystals with lower defect density compared with CVD growth. Sublimation growth has been most successfully employed to grow SiC[146] and AlN[147] bulk single crystals.

In our previous study[148], we investigated the morphology and crystallographic orientation of TiN crystals grown by sublimation at temperatures of 1820˚C ~ 1920˚C, and pressures of 0.2 atm ~ 1.2 atm. The TiN crystals deposited on W (001) exhibited a preferred orientation of TiN (001) || W (001) and TiN [100] || W [110], which resulted in a 45° angle between TiN [100] and W [100]. Therefore, the orientation of TiN crystal growth is easily controlled since W [100] is a common orientation of rolled tungsten sheet, providing an additional advantage for TiN crystal growth compare to other materials grown by sublimation.

In this study, the sublimation growth of titanium nitride crystals on tungsten substrates is reported in more detail. The TiN crystals orientation is further studied not only on (001) textured tungsten substrates, but also on non-(001) orientated (random) tungsten substrates. The dependence of the growth rate on temperature and pressure was established and compared with AlN sublimation growth under similar conditions. The activation energy was also calculated based on the change in the TiN growth rate with temperature. The elemental composition and the N/Ti ratio before and after crystal growth of the source materials were measured to see if there were any significant variations in the TiN composition with growth conditions. The morphology of the TiN crystals during different stages of growth was studied to determine how their characteristics changed with time. The overall growth rate was divided into two parts, the vertical rate (perpendicular to the surface) and lateral rate (parallel to the surface), and their relationship with the overall growth rate, dependence on the length of growth, and function on crystal morphology were investigated and discussed.

6.2 Experimental

The TiN crystals were grown in a resistively-heated tungsten furnace using a tungsten crucible within a tungsten retort to contain the titanium vapor. TiN crystals were deposited on a tungsten foil (25 mm diameter) placed on the top of the crucible. The source, TiN powder with oxygen as the main impurity, was sintered before crystal growth, to reduce the oxygen concentration. The TiN powder source was sintered by first baking in a 5% hydrogen and 95% argon gas mixture at 1000°C for about 2 hours, then heating in ultra pure nitrogen gas to 1900°C for another 4 hours. Chemical analysis was performed of some of the nonmetallic elements (C,N, and O) in the TiN source to determine how their concentrations were changed by sintering. The elements' concentrations in the TiN source before and after this process were measured by the gas fusion method. Before each growth, the source was again baked in 5% hydrogen and 95% argon gas mixture at 1000 °C for about 1 hour to reduce the surface oxide. The growth temperature was measured by an optical pyrometer focused on the top of the retort, and a temperature difference of approximately 50°C was maintained between the source zone and the crystal growth zone. All the experiments were performed in pure nitrogen, and the growth time was varied from 30 minutes to 15 hours. The growth rate was investigated as a function of a number of temperature (1980 - 2110 °C) and pressure (0.06 - 1.25 atm) combinations

The overall growth rate, defined as mass change per unit time, was determined by dividing the TiN crystal weight increase by the time at the growth conditions. The film thickness of each sample was estimated by $h = m/(S\rho)$, knowing the total weight increase-m, density-ρ, and the area-S of the deposited material. The grain sizes (the

projected area of individual crystals) and the grain heights were measured using scanning electron microscopy (SEM – FEI Philips XL-30, Eindhoven, The Netherlands) and averaged from a number of condensed TiN crystals at each growth condition. The average crystal dimensions were determined by measuring twenty four crystals selected at random from different regions of each sample, then eliminating the two largest and smallest crystals from the calculation, and averaging the remaining twenty.

The orientation of the TiN crystals and the underlying tungsten substrate were determined independently by both X-ray diffraction (XRD) and electron backscatter diffraction (EBSD) in a SEM. Pole figures from individual TiN crystals and their underlying tungsten substrate grains were collected by EBSD to determine their relative orientation relationships. Families of (001) planes were used to reveal the orientation relationship between the TiN and W lattices. The elemental composition for TiN powders and crystals were measured by Auger electron spectroscopy. Auger analysis was done using a Phi-680 scanning Auger nanoprobe (Physical Electronics, Inc. Chanhassen, MN) with a field emission electron gun, cylindrical mirror electron energy analyzer, and Ar-ion sputter gun. The energy and current of the probe electron beam was 20 kV and 10 nA, respectively and give a spot size for the probe beam of ~15 nm. The beam was held at fixed points to yield spectral information (i.e. surface composition) for that feature or was rastered over a given area to give either secondary electron images or Auger elemental maps. Depth profiling was performed in selected areas by monitoring the Auger signal of selected elements while alternately sputtering for a given amount of time. The sputter rate that was used (calibrated for a standard SiO2 film) was 150nm/min. The base pressure of the analysis chamber was ~5x10-10 torr and was maintained by

introducing samples through a turbo-pumped load-lock. Data was acquired and analyzed using Phi PC-Access and Phi Matlab software, respectively.

6.3 Results and Discussion

Though several solid and vapor phase species that may form in the Ti-N system according to the available thermal data in JANAF table[137], the most probable gas phase products of TiN decomposition are those species with the lowest Gibbs free energy of formation: Ti(g) and N_2(g). Thus the crystal growth process begins with source decomposition and the reaction:

$$2TiN(s) \leftrightarrow 2Ti(g) + N_2(g) \tag{6-1}$$

which has a Gibbs free energy of 273.96 kJ/mol at 2300 K (2027 °C) and 251.96 kJ/mol at 2400 K (2127 °C)[137]) . Because the reverse reaction has a large negative Gibbs free energy change, the crystals readily condense in the cooler region of the furnace.

It is useful to compare the sublimation of TiN to another material, aluminum nitride, since sublimation growth has been successfully employed to produce AlN with decomposition and the reaction:

$$2AlN(s) \leftrightarrow 2Al(g) + N_2(g) \tag{6-2}$$

Titanium nitride has a higher melting point (2930˚C)[147] than aluminum nitride (m.p. = 2200˚C and b.p. = 2517˚C[149]). Although the standard formation enthalpy of titanium nitride and aluminum nitride are similar (TiN, -337.649 kJ/mol; AlN, -317.98 kJ/mol at 298.15˚C), the standard formation enthalpy of titanium gas is about 100 kJ/mol larger than that of aluminum gas at the temperature below their boiling point. Hence, titanium's vapor pressure over TiN (for stoichiometric decomposition) is significantly lower than aluminum's vapor pressure over AlN under the same conditions. For pure

material sublimation under the ideal case of equations (6-1) and (6-2), assuming a constant inert gas pressure of 0.1 MPa, the calculated Ti vapor pressure over TiN ranges from 2.6 Pa at 1927 °C to 78.8 Pa at 2227 °C[137], while the calculated Al vapor pressure over AlN ranges from 980 Pa to 15,000 Pa[137] at the same conditions. With nitrogen as the ambient gas, which is typical in sublimation growth of metal nitrides, both the Ti vapor pressure over TiN and Al vapor pressure over AlN are lower than the calculated values, since the extra nitrogen will drive reactions (6-1) and (6-2) to the left side. In short, because of the much lower vapor pressure of Ti, its growth rate will be much lower than that of AlN for the same conditions, which was also confirmed by the experiment results.

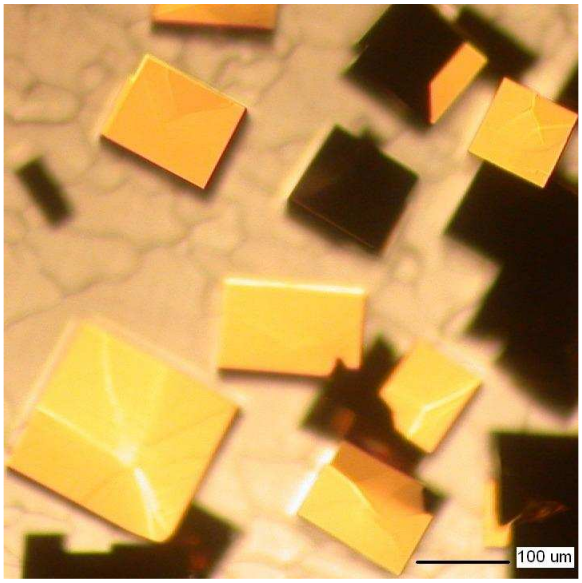

Figure 6.1 Optical microscope images of TiN crystals grown on W.

6.3.1 Composition and morphology

The measured weight percents of nitrogen, oxygen, and carbon in the original TiN powder were 22.0%, 0.51%, and 0.049%, respectively. After using the same TiN source for several crystal growth experiments, the concentration of these elements were 22.0%, 0.32%, and 0.26%, respectively. Thus, the oxygen concentration was reduced while the carbon concentration was increased. Assuming the impurities formed compounds with

stoichiometries of TiC and TiO_2, then the N/Ti ratio in the original powder is similar to that found in the remaining source, $TiN_{0.984}$ and $TiN_{0.989}$, respectively. For the crystals, Auger analysis showed that the N/Ti ratio was the same regardless of the temperature and pressure under which they were grown. Auger analysis also confirmed that the oxygen concentration in the crystals was lower than in the original powder and the N/Ti atomic ratio in the crystal was similar to the powder.

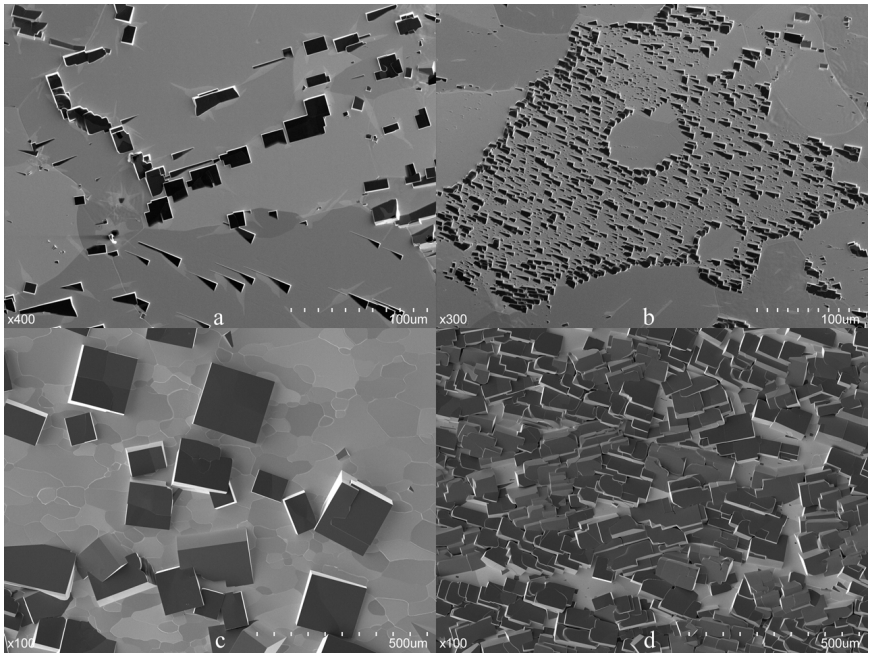

Figure 6.2 SEM top view of TiN crystals.
TiN crystals grown for 30 mins at 2100 ˚C, 1.25 atm (a), 2000 ˚C, 0.8 atm (b), 15 hrs at 2000 ˚C, 0.2 atm (c, d). After 30 mins growth, some preferential crystal nucleation takes place along the tungsten grain boundaries (a), the crystals within the same tungsten grain have similar shapes and orientions (b). After 15 hours growth, the top surfaces of single TiN crystals are square or rectangular (c), grains merged together display more irregular shapes (d).

The TiN crystals were a bright golden color and most of the large single grains have an orthorhombic shape, as shown in Figure 6.1. Figure 6.2shows SEM images (parallel to the growth direction) for TiN crystals grown for 30 mins at 2100 ˚C, 1.25 atm (a), 2000 ˚C, 0.8 atm (b), and 15 hours at 2000 ˚C, 0.2 atm (c, d). The crystals that formed within 30 minutes were square, rectangular, or triangular in morphology/shape. The crystals tended to nucleate along the grain boundaries of the tungsten substrate

(Figure 6.2a). Within the same tungsten grain, many of the individual TiN crystals had similar shapes and were oriented in the same direction (Figure 6.2b). These TiN crystals continued to grow with the same orientation as it nucleated. After several hours of growth, some single grains still maintained square or rectangular surfaces (Figure 6.2c), but the majority of grains merged together to display less regular shapes (Figure 6.2d). The side view (perpendicular to the growth direction) SEM images of TiN crystals provide more details about their morphology, as shown in Figure 6.3 and Figure 6.4. The lateral dimensions of the crystals are generally larger than their vertical dimension for samples grown for short times, less than 30 minutes. The TiN crystal grains are thin, flat tablet-shaped. Those crystals with square or rectangular top areas exhibited different shapes, either thin orthorhombic (Figure 6.3a) or wedge (Figure 6.3b), while those with triangular surfaces exhibited shapes of either truncated cubes (Figure 6.3c) or titled wedges (Figure 6.3d). For growth times of 12 hours and longer, though most crystals retain an orthorhombic shape (Figure 6.4a), the majority of the TiN crystals form a continuous film (Figure 6.4b) that were separated from the tungsten substrate in some regions. This separation initiates at voids formed between merged TiN grains and expands by the thermal expansion coefficient mismatch between TiN and tungsten during cooling from the growth temperature. Furthermore, for samples grown for 30 mins, the majority of the crystals had similar size and shape within the same sample, which suggested that most crystals nucleated at roughly same time. For samples grown more than 12 hours, the majority of crystals that merged together had a smaller size than individual crystals, which suggests that lateral growth was limited by proximity to neighboring crystals.

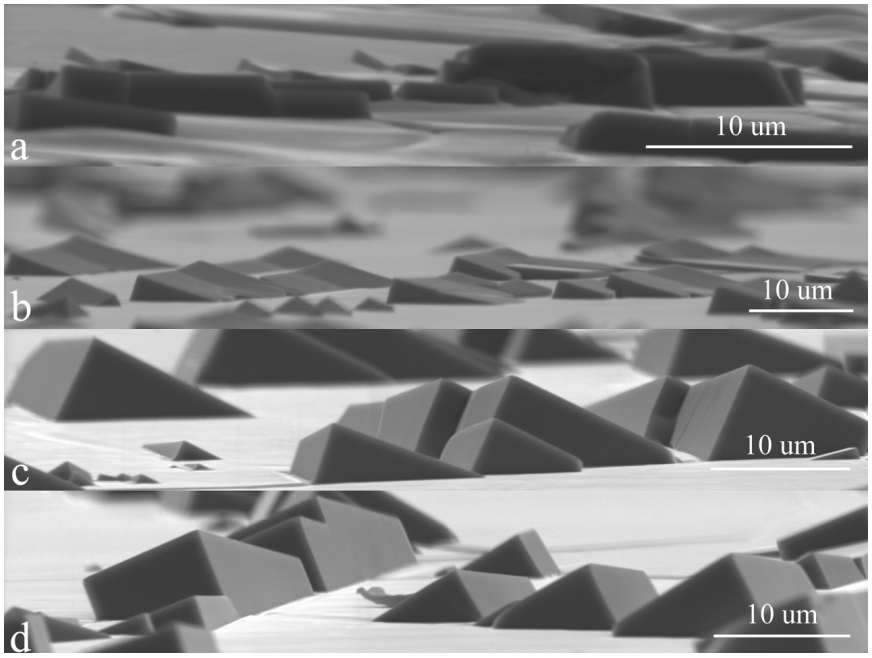

Figure 6.3 SEM side-view images of TiN crystals.
TiN crystals grown for 30 mins at 2000 ˚C, 1.25 atm (a and b) and 2100 ˚C, 1.25 atm (c and d). Crystals with square or rectangular surfaces were orthorhombic (a) or wedge (b) shaped, and crystals with triangular surfaces were titled wedges (c) or truncated cubes (d).

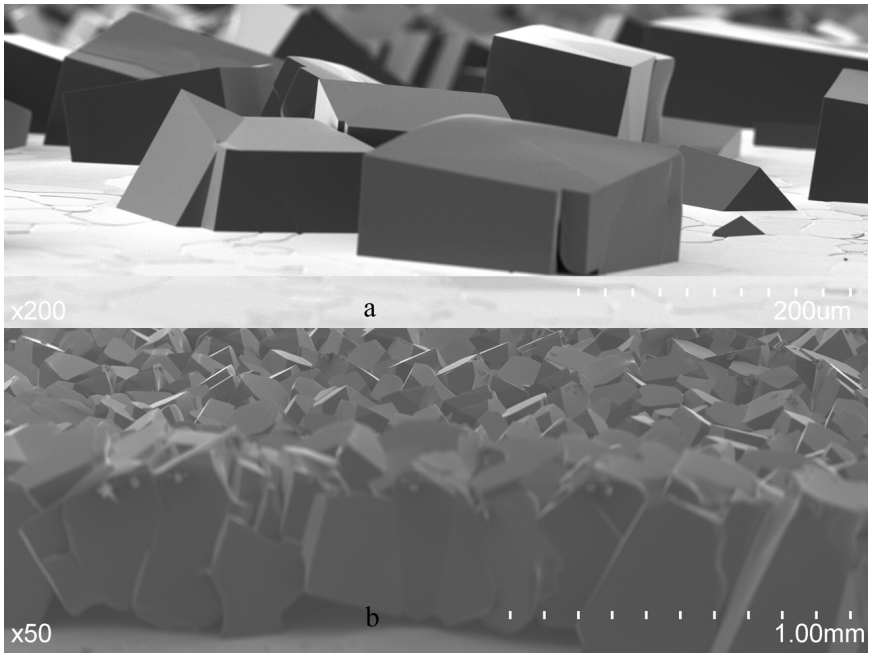

Figure 6.4 SEM side-view images of TiN crystals.
TiN crystals grown for 15 hrs at (a) 0.2 atm, 2000 ˚C, where most individual crystals maintain an orthorhombic shape, and (b) 2100 ˚C, where TiN crystals have merged to form a continuous film, the TiN separates from the tungsten substrate in places (shown by arrow).

6.3.2 Orientation

EBSD analysis on the tungsten substrate and condensed TiN crystals revealed the orientational relationship TiN (001) || W (001) with normal direction TiN [100] || W [110], a 45^{o} rotation between the TiN and W lattices, as defined by their primary unit cell directions [100]. If the tungsten substrate (001) plane was parallel to the growth surface, the TiN crystal (001) planes were also parallel to the surface, producing an orthorhombic crystal shape. If the tungsten substrate (001) plane was slightly offset (tilted) from the surface, the TiN crystal (001) planes were also slightly offset from the surface, but were still parallel with the underling W (001) plane with normal direction TiN [100] || W [110], producing either a truncated cube or tilted wedge crystal shape. Figure 6.5 and Figure 6.6 are the EBSD results for a group of TiN crystals grown on the tungsten substrate that were aligned in two linear arrays near the grain boundaries. The 12 randomly selected TiN grains were all oriented with a TiN [001] plane normal at the center of the pole figure (perpendicular to the substrate) and their other [010] and [100] plane normals lying in the plane of the substrate (Figure 6.5). Five different points (1, 5, 6, 7 and 8) for the underling tungsten grain and 3 different points (2, 3 and 4) for nearby tungsten grains (corresponding to the solid and hollow symbols, respectively) were selected for EBSD analysis (Figure 6.6). The tungsten grain underlying the selected TiN crystals clearly is oriented with W [001] perpendicular to the substrate and that there is a 45^{o} angle between TiN [100] and W [100] (see respective pole figures in Figure 6.5 and Figure 6.6). The three adjacent tungsten grains exhibit significantly different orientations from the center grain. Figure 6.7 and Figure 6.8 are the EBSD results for TiN crystals grown on three adjacent tungsten grains having different orientations, i.e., both the W (001) plane for

these three different tungsten grains and the TiN (001) plane for the TiN crystals grown on these grains are tilted with respect to the surface normal. Nevertheless, their (001) planes are parallel, with a 45^o angle between the perpendicular TiN [100] and W [100] directions. For example, the TiN crystals labeled 3 and 4 in Figure 6.7 are grown on the tungsten grain at point 3 in Figure 6.8, and the normal TiN [001] lies at the same position with normal W [001]; though there is 180^o angle between two crystals' TiN [010] normals, they still have same orientation as the <100> of rock salt crystal structure is a C_4 rotation axis; obviously there is a 45^o angle between TiN [100] and W [100]. Similar orientations are seen between the TiN crystals at points 1 and 2 in Figure 6.7 and tungsten grain at point 1 in Figure 6.8; between TiN crystals at points 5 and 6 in Figure 6.7 and tungsten grain at point 2 in Figure 6.8. This orientation relationship was confirmed by XRD for samples grown for more than 12 hours. The XRD analysis of the original polycrystalline tungsten foil substrate along the growth direction displayed a highly oriented (200) texture. Small (111), (220), and (311) diffraction peaks were also observed, but had negligible intensity relative to the (200) diffraction peak. The XRD pattern from a 6 mm TiN crystal sample grown on the highly-oriented W (200) foil also displayed highly oriented (200) texture (Figure 6.9).

This orientation preference between TiN crystals and tungsten substrates minimizes the lattice constant mismatch. Since the lattice constant of TiN (4.240 Å) is much larger than tungsten (3.165Å), their cube-on-cube lattice mismatch is quite large, 33.96% (based on tungsten). However, rotating the unit cell by 45^o and considering the square that is formed by the nearest 4 titanium atoms or nitrogen atoms as a unit (Figure 6.10), the nearest atom distance in this new square is 2.998 Å which give a cube-on-cube

atom distance mismatch of 5.28% (based on tungsten). Thus, the TiN crystals orient on tungsten to minimize the lattice mismatch. Therefore a 45^{o} angle exist between the tungsten unit cell and TiN unit cell, and result in orientational relationship TiN (001) || W (001) with normal direction TiN [100] || W [110]. Even if the surface W {001} planes are slightly tilted off-axis, the above orientational relationship is still followed as it offers the minimum lattice mismatch, with TiN(001) parallel to W(001), slightly offset from the growth surface.

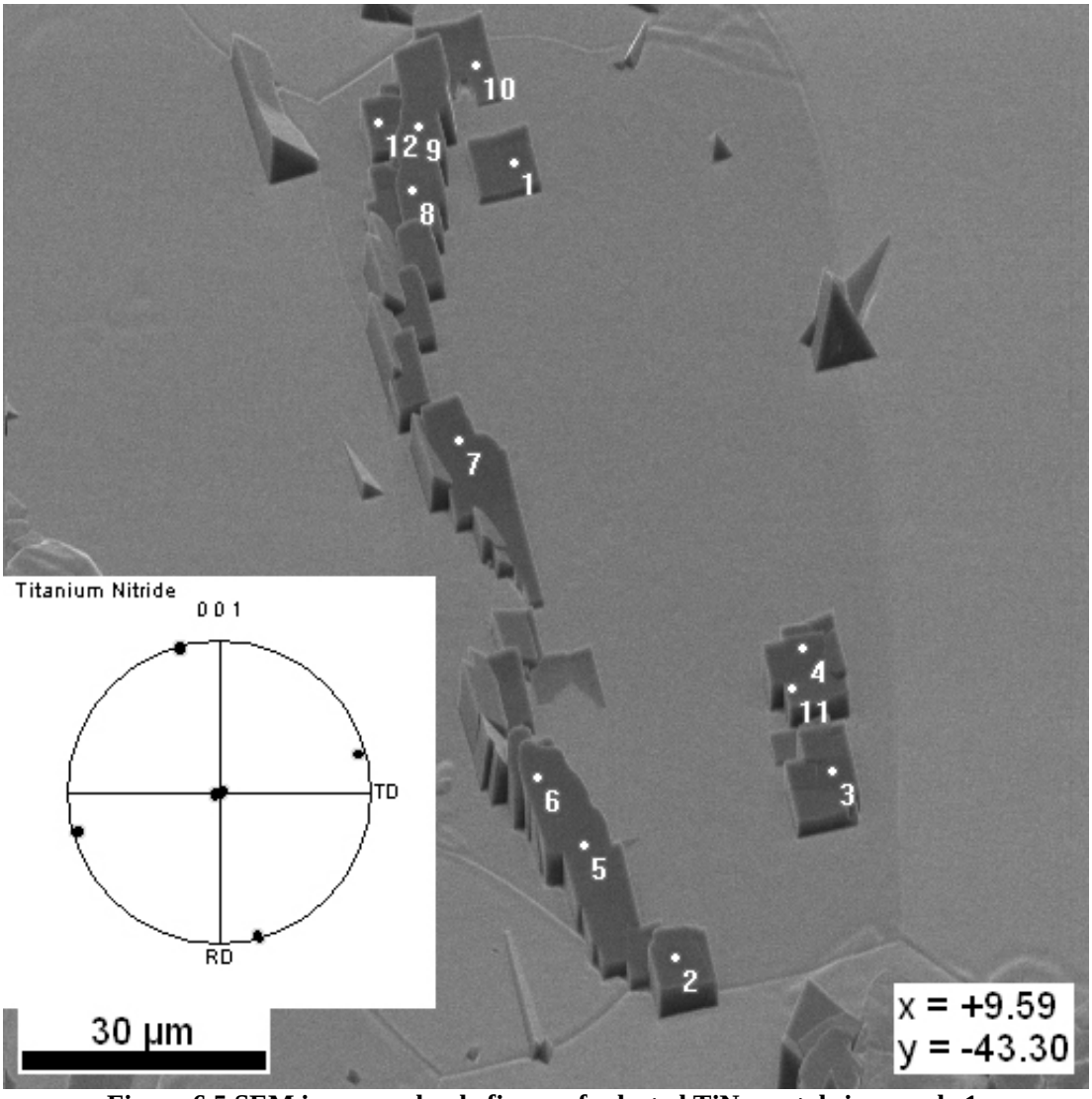

Figure 6.5 SEM image and pole figure of selected TiN crystals in sample 1. All TiN grains were oriented with [001] normal to the substrate (center of the pole figure)

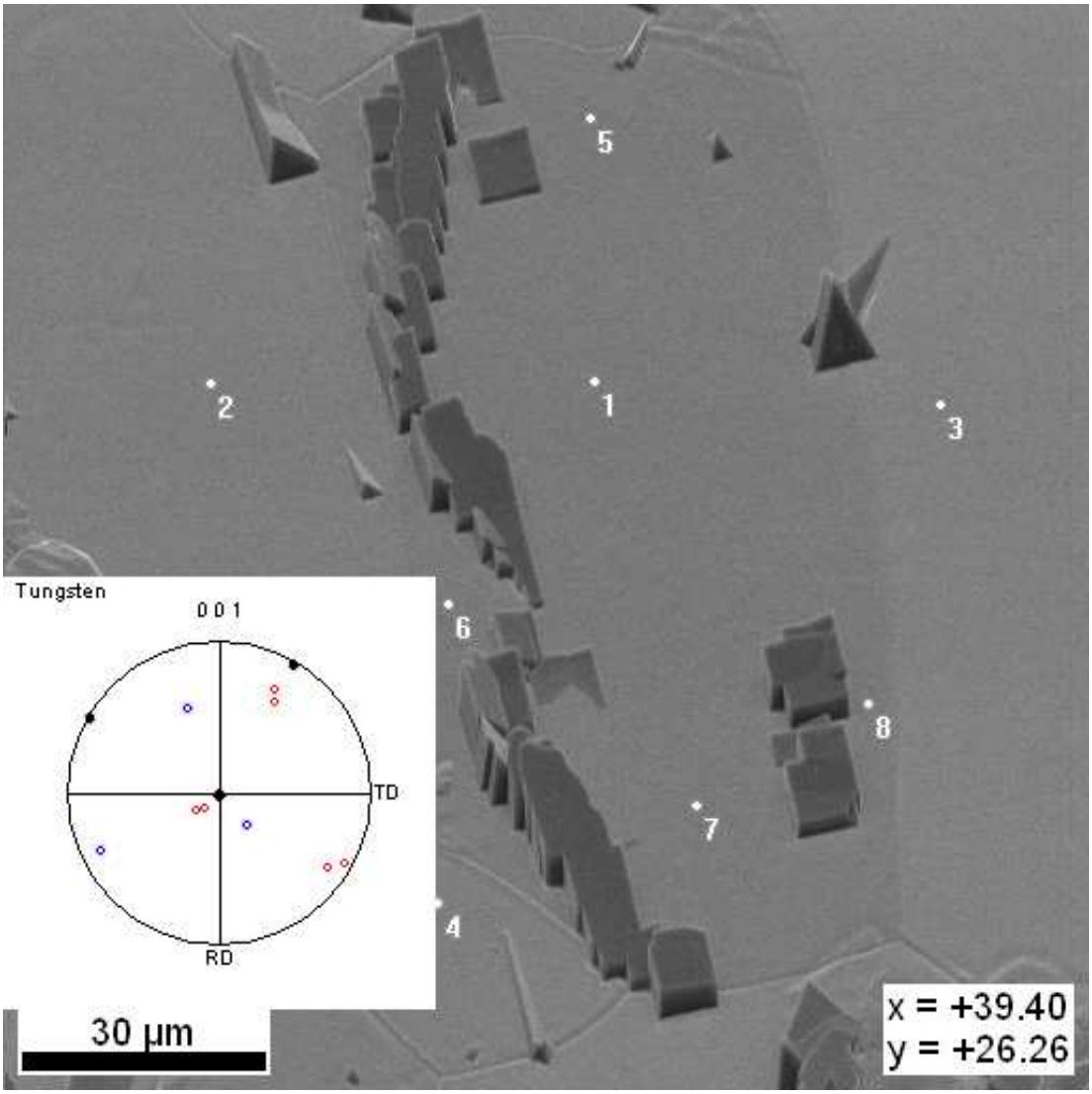

Figure 6.6 SEM images and pole figure of tungsten grains in sample 1.
Tungsten grain (points 1, 5, 6, 7, 8) underlying the selected TiN crystals in Fig. 5a were oriented with (001) surface normal (solid symbols in the pole figure); Adjacent tungsten grains (points 2, 3, 4) showed orientations with (001) offset from the substrate normal (hollow symbols in the pole figure)

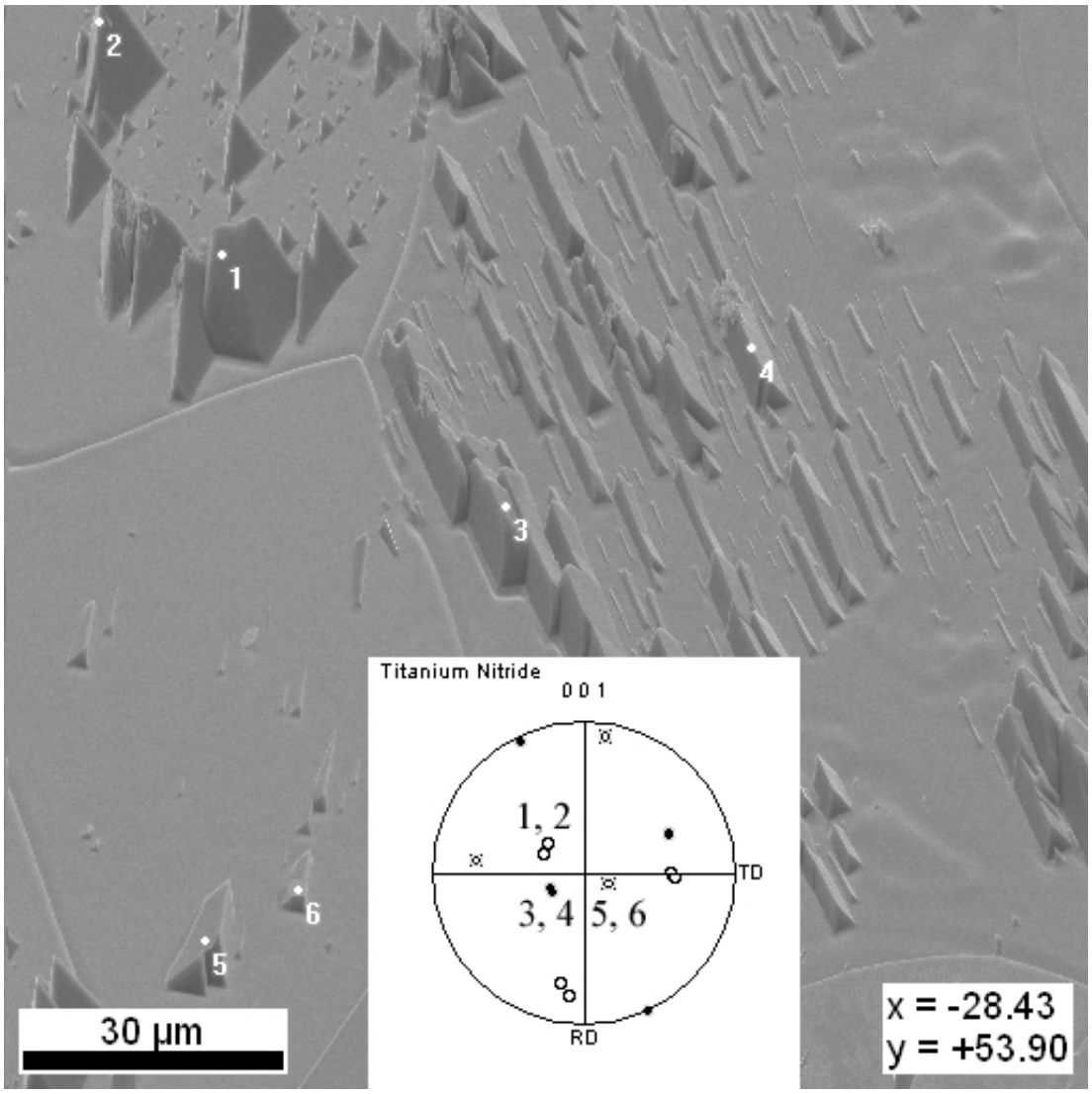

Figure 6.7 SEM images and pole figure of TiN crystal in sample 2.
TiN crystals grown on same tungsten grain (1 and 2, 3 and 4, 5 and 6) were oriented in the same way (one symbol pattern in the pole figure represents one orientation, symbols for different TiN grains with the same orientation overlap).

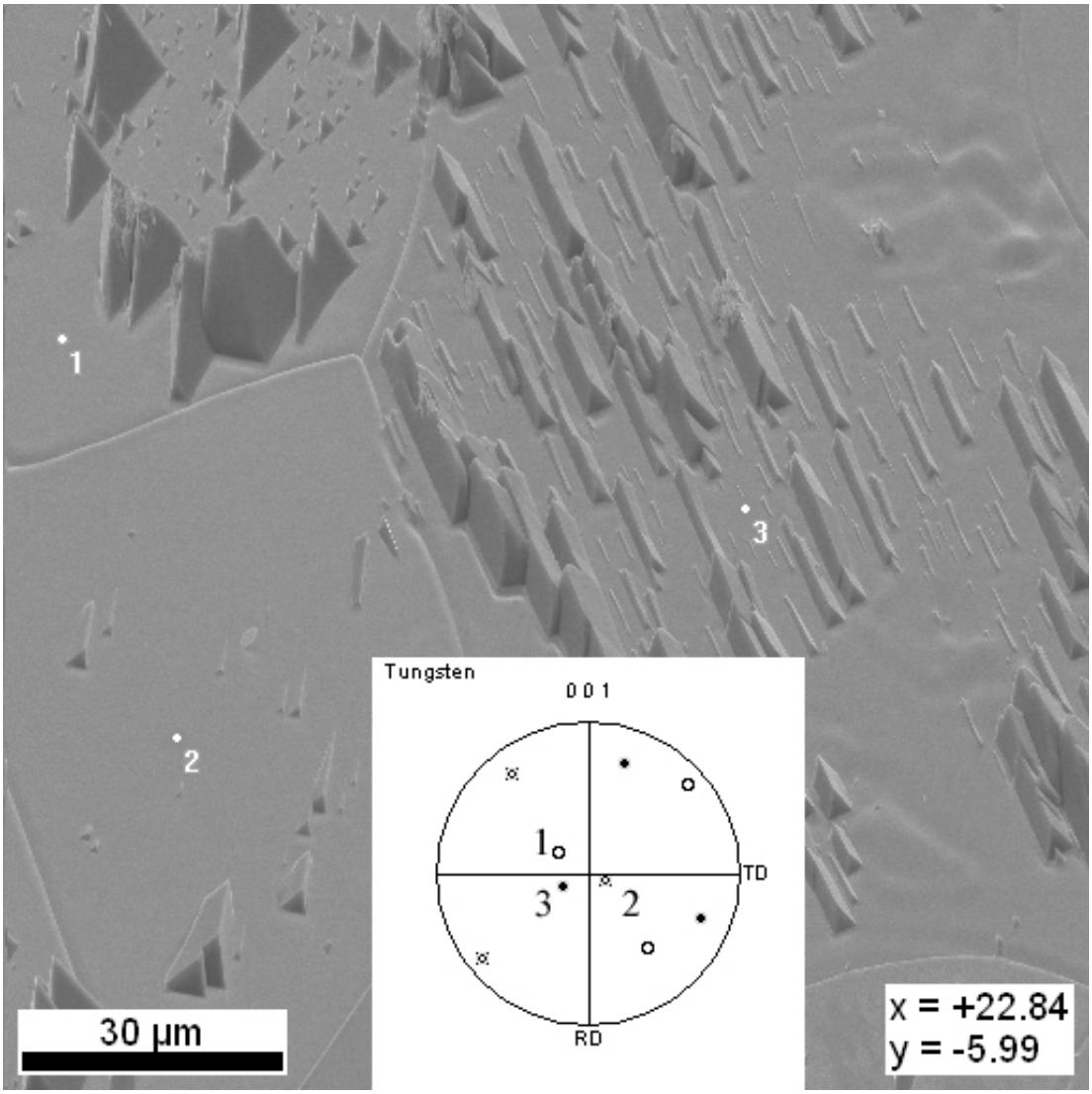

Figure 6.8 SEM images and pole figure of the tungsten grains in sample 2.
The adjacent tungsten grains underling the TiN crystals (1, 2 and 3) were oriented with (001) offset from the substrate normal ; all selected TiN were oriented with (001) parallel to the underling tungsten (001) with a 45^{o} angle between TiN (100) and W (100).

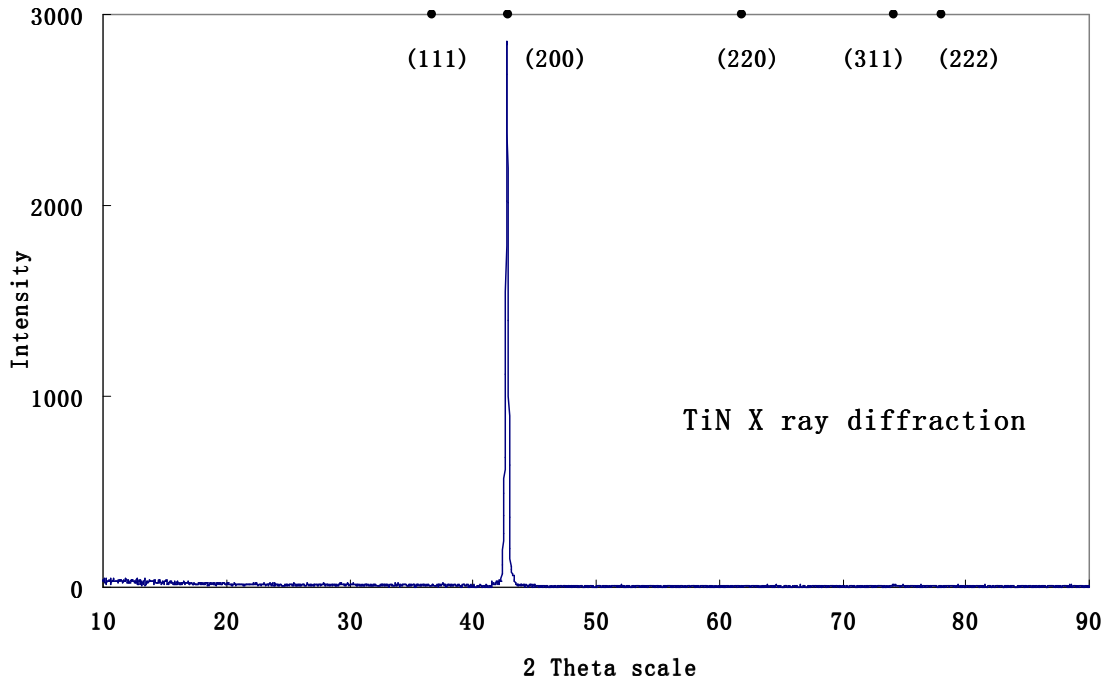

Figure 6.9 XRD on TiN layer (6mm, 2000 ^{o}C, 0.2 atm) with strong (200) texture

6.3.3 Overall growth rate

The sublimation growth rate for TiN crystals on W is much lower than that for AlN under similar growth conditions. For instance, the AlN sublimation growth rate is 1950 mg/hr(unpublished work by Li Du and J.H.Edgar) while the TiN crystal growth rate is only 6 mg/hr at 2100 °C, 0.8 atm (measured in this study). Increasing the temperature or decreasing the pressure enhances the TiN growth rate; the highest growth rate in this study was 98.89 mg/hr at 2100 °C and 0.06 atm. Figure 6.11 and Figure 6.12 show the dependence of the growth rate on temperature and pressure: the logarithmic growth rate is first order dependent on reciprocal temperature, while growth rate itself varies with reciprocal pressure to the 1.5 power.

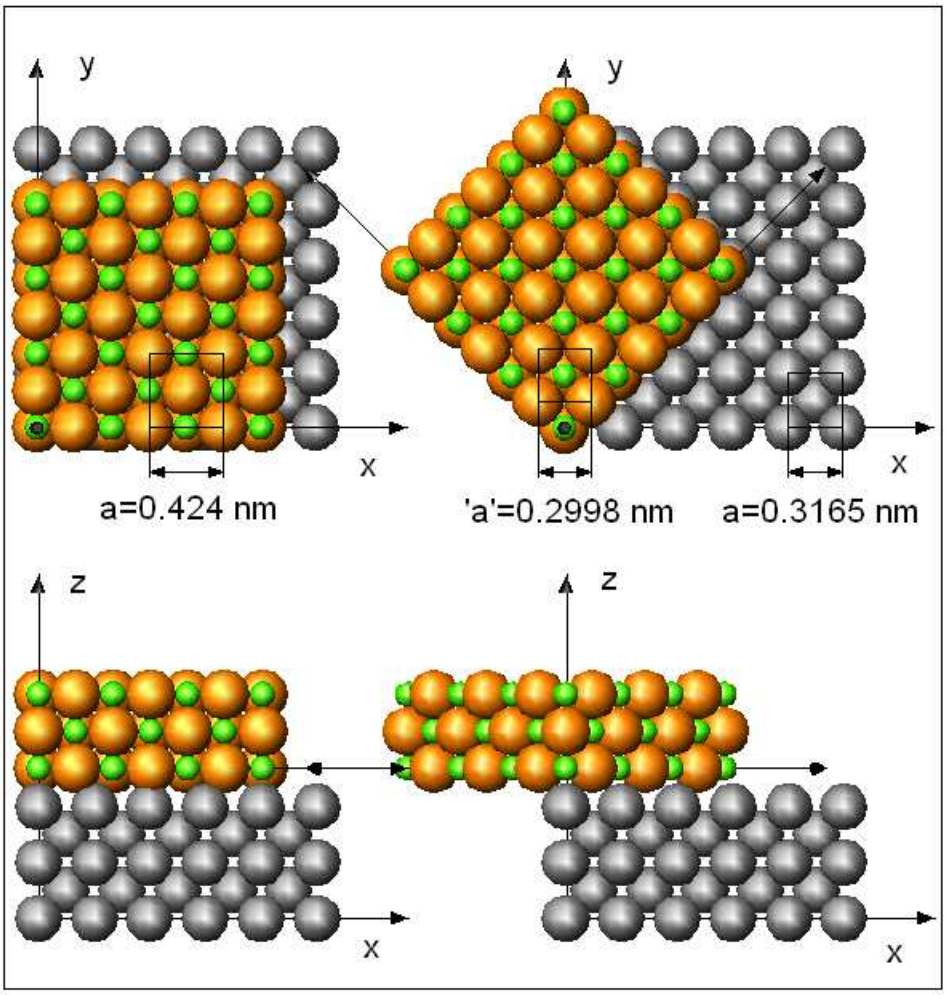

Figure 6.10 Schematic diagram of TiN and W lattice
Gray spheres are tungsten, orange spheres and green spheres are Ti and N, respectively. Top: top view, bottom: side view, left: TiN [100] // W [100], right: TiN [100] ∩W [100]= 45°. The orientation of TiN (001) || W (001) with 45° angle of their in-plane [100] can minimize the lattice constant mismatch.

By combining the Arrhenius equation with sublimation-recondensation kinetics, a general expression can be obtained to determine the activation energy of TiN sublimation growth:

$$\left.\begin{aligned} r = d\alpha/dt = kf(\alpha) \\ \ln r = (-\frac{Ea}{RT}) + \ln A \end{aligned}\right\} \Rightarrow \ln\frac{d\alpha}{dt} = (-\frac{Ea}{RT}) + \ln A + \ln f[\alpha] \qquad (6\text{-}3)$$

where *Ea* is the activation energy, *A* is the pre-exponential factor or frequency factor, *R* is the ideal gas constant, *r* is the growth rate, α is the degree of conversion, and

$f(\alpha)$ is a mathematical function whose form depends on the reaction type. For the Ti+N system, the relationship between the rate constant *k* and the growth rate above——$(d\alpha/dt) = kf(\alpha)$——has not yet been determined. However, as the transport of growth species from source to growing surface is often the rate limiting step in vapor crystal growth[150], equilibrium can be assumed at the surfaces of the source and seed. So for reaction (5-1):

$$K^{eq} = \frac{[Ti]^2[N_2]}{[TiN]^2} = \frac{(f_{Ti}{}^{eq})^2(f_{N_2}{}^{eq})}{(a_{TiN}{}^{eq})^2} \tag{6-4}$$

Since the growth pressures used in this study were not high (<1.25 atm), solid species activity is close to unity and gas fugacity can be represent by gas species partial pressure, that is:

$$K^{eq} = (P_{Ti}{}^{eq})^2(P_{N_2}{}^{eq}) \tag{6-5}$$

For a fixed growth temperature and pressure, the local gas phase species concentration at the growth surface remains the same and $f(\alpha)$ is approximately constant. Therefore, the sublimation growth rate is proportional to the rate constant and yields a first order dependence of logarithmic growth rate on reciprocal temperature at same pressure (confirmed in Fig. 8):

$$\frac{d\ln r}{dT} = \frac{Ea}{RT^2}\left(r = \frac{d\alpha}{dt}\right) \tag{6-6}$$

The calculated activation energy is 775.8±29.8kJ/mol (from Figure 6.11), which is very close to enthalpy of TiN sublimation from available thermodynamic data[137] with 781.6 kJ/mol at 2300K (2027°C) and 779.7 kJ/mol at 2400K (2127°C) in the growth temperature range.

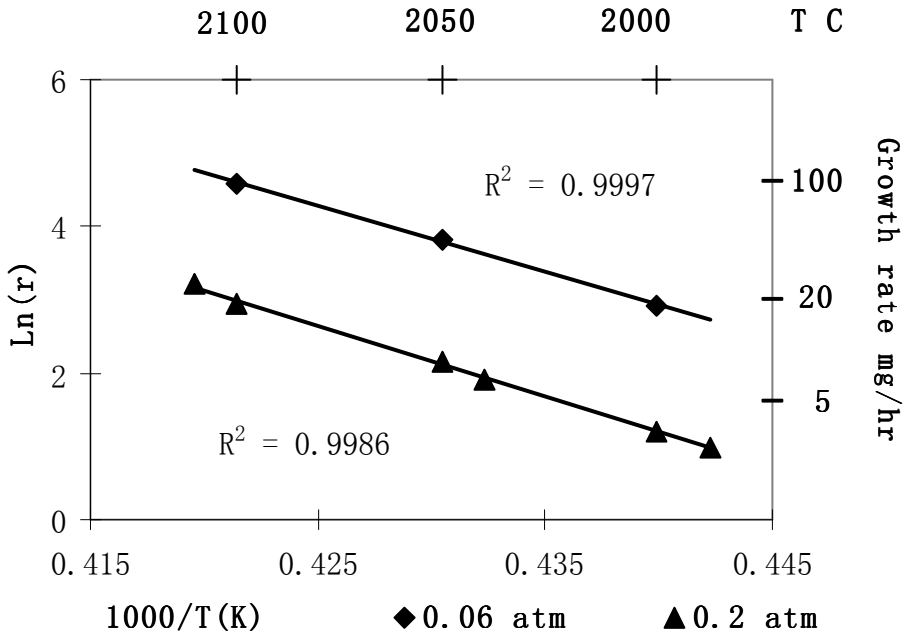

Figure 6.11 Growth rate and growth temperature
The variation of the logarithmic growth rate on reciprocal temperature at constant pressure.

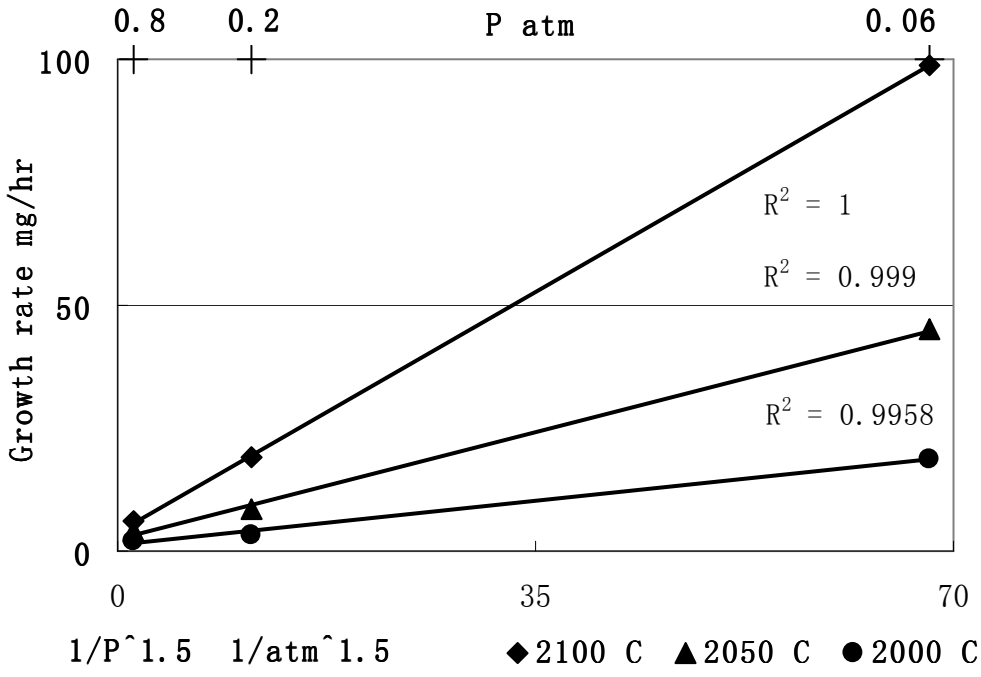

Figure 6.12 Growth rate and growth pressure
The growth rate variation with reciprocal growth pressure at constant growth temperature.

6.3.4 Lateral and vertical growth rates

The average size and height of the condensed TiN crystals changed with growth temperature, pressure and time. Generally, at the same temperature and pressure, longer growth time resulted in larger crystals, and after the same growth time, crystals were larger at a higher temperature or a lower pressure because of a higher growth rate. For example, after 30 mins growth at 1.25 atm, when the temperature was increased from 2000 °C to 2100 °C, the average size of the crystals increased from about 110 μm^2 to 594 μm^2 (a factor of 5.4), while after 30 mins growth at 0.8 atm, when the temperature was increased from 2000 °C to 2100 °C, the average size of the crystal increased from about 215 μm^2 to 1150 μm^2 (a factor of 5.4). For crystals grown over several hours, with varied temperature and pressure, the average size change was not as clear as the size changes observed after 30 mins growth, since most TiN crystals merged together after longer times. Two examples are two sets of experiments for size change after 15 hours growth at 0.2 atm and 12 hour growth at 0.06 atm (see Figure 6.2 and Figure 6.4). When the temperature was increased from 2000 °C to 2100 °C, the average size of the TiN crystals grown at 0.2 atm increased from about 1.75×10^4 μm^2 to 5.83×10^4 μm^2 (a factor of 3.3), while the average size of the crystals grown at 0.06 atm increased from about 5.06×10^4 μm^2 to $1.37 \times 10^5 \mu m^2$ (a factor of 2.7); these two factors are smaller than the size change factors for samples grown in 30 mins. However, the average TiN crystal heights changed with the growth temperature; when the temperature was increased from 2000 °C to 2100 °C, the average height increased from about 77μm to 392μm (a factor of 5.1) for crystals grown at 0.2 atm (see Figure 6.4) and from about 169μm to 954μm (a factor of 5.7) for crystals grown 0.06 atm.

Although the overall growth rate depends on temperature and pressure in general, the lateral and vertical growth rates also changed with time. The lateral growth rate is much higher initially (30 mins for example) for individual crystals and decreases after many of the grains have merged together. The vertical growth rate follows an opposite trend. To investigate the lateral and vertical growth rates of the TiN crystals, we define the lateral rate as the projected area (or size) change of the crystal per time with units of μm^2/hr, and vertical rate as thickness (or height) change of the crystal per time with the unit of μm/hr. Since the lateral rate has different units (μm^2/h) than the vertical rate, (μm/hr), a basic arithmetic comparison may not be effective, hence we will compare each with the overall growth rate at different growth stages. As the crystal structure of TiN is rock salt, if we consider the volume of each grain to be equal (prism) or proportional (pyramid) to the product of the grain size (s) and grain height (h), and the majority of the crystals nucleated at same time (changes in crystal quantity can be neglected), the growth rate *r* yields:

$$r = n\rho C\frac{dV}{dt} = n\rho C(s\frac{dh}{dt} + h\frac{ds}{dt}) \qquad (6\text{-}7)$$

where *C* is a constant, ρ is density, *n* is the crystal quantity and V is average volume of a crystal.

At the initial growth stage, the majority of TiN crystals form as individual crystals, therefore competitive growth between neighboring crystals can be neglected. Thus, the logarithmic value for one of the two variables on the right side of equation (5-7), *s* and *h*, shows first-order dependence on reciprocal temperature only if the other is constant or nearly constant. This leads to the following deduction:

$$\left.\begin{aligned} &\frac{d\ln r}{dT} = d\ln(s\frac{dh}{dt} + h\frac{ds}{dt}) \Big/ dT = \frac{Ea}{RT^2} \\ &\text{lateral rate } l = \frac{ds}{dt},\ \text{vertical rate } v = \frac{dh}{dt} \end{aligned}\right\} \Rightarrow \begin{cases} \dfrac{d\ln v}{dT} = \dfrac{Ea}{RT^2}; & \text{s is constant} \\ \dfrac{d\ln l}{dT} = \dfrac{Ea}{RT^2}; & \text{h is constant} \end{cases} \quad (6\text{-}8)$$

Two sets of experiments were conducted, for 30 min growth times to guarantee that a majority of crystals are present as individual crystals, to investigate the lateral and vertical growth rates at the initial growth stage; (1) 0.8 atm with temperature range from 2000 °C to 2100 °C and (2) 1.25 atm with temperature range from 2000 °C to 2100 °C. The logarithmic lateral growth rates versus reciprocal temperature for each are plotted in Figure 6.13. Each shows a first order dependence on the reciprocal temperature. The products of the two slopes and the general gas constant give activation energies of about 752.0 and 757.3, which are in the range of the calculated activation energy 775.8±29.8kJ/mol. This implies that the lateral growth rate for each experiment is proportional to the overall growth rate, and their vertical rates can be neglected.

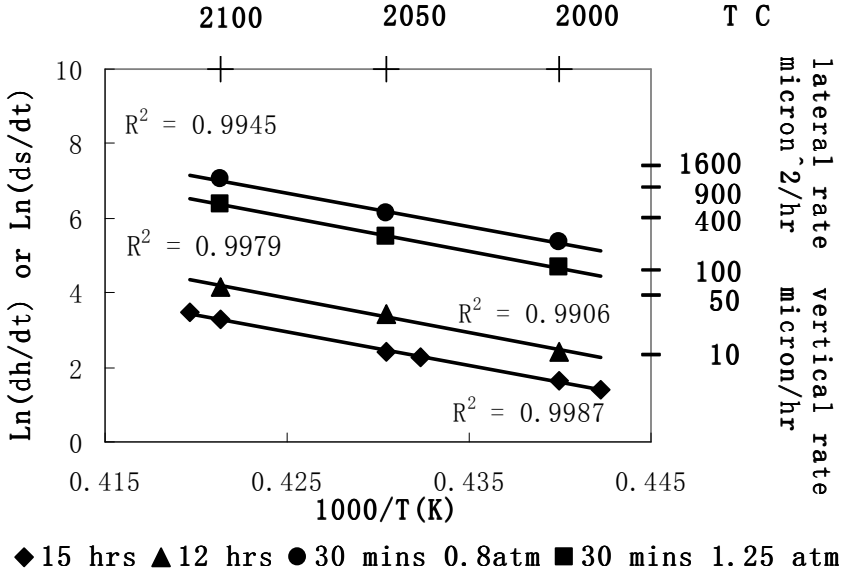

Figure 6.13 Lateral growth rate and logarithmic vertical rate vs temperature
Logarithmic lateral growth rate vs reciprocal temperature for two 30 mins growths and logarithmic vertical rate vs reciprocal temperature for 12 hrs and 15 hrs growth

After the TiN crystals merge together, the TiN crystals grew vertically as the height increased and laterally by competitive growth with neighboring crystals. Fast-growing crystals will increase in lateral size as slow-growing grains will be blocked and eventually disappear from top view. Two sets of experiments with growth time longer than 12 hours were conducted to compare lateral and vertical growth rates after many TiN crystals had merged together; (1) 12 hours growth at 0.06 atm with temperature range from 2000 °C to 2100 °C and (2) 15 hours growth at 0.2 atm with temperature range from 1980 °C to 2110 °C. The logarithmic vertical growth rates show a first order dependence on the reciprocal temperature and are also plotted in Figure 10. The products of the four slopes and the gas constant give values that are all in the range of the calculated activation energy 775.8±29.8kJ/mol (777.5 and 746.9, respectively), indicating the vertical growth rates for these two sets of experiments are proportional to their overall growth rates and are significantly higher than those observed at the initial stage of growth. Regarding the lateral growth rates for these two experiments, both the crystal morphology (SEM images) and size statistics described previously showed that they are limited by interaction between the neighboring crystals and lower than at the initial stage.

These results show that lateral growth predominates initially, while vertical growth becomes more important after the crystals have merged together and the surface of the tungsten becomes covered with TiN. Growth is more likely to be 2D growth initially. The length of the initial stage may vary depending on the growth temperature and pressure. In this study, growth for 30 mins was within the initial growth stage at 1.25 atm and 0.8 atm between 2000°C to 2100°C. As a result of the much higher overall growth rate, the initial growth stage at 0.2 atm and 0.06 atm between 2000 °C to 2100 °C

(TiN grains merged together much quicker) are much less than 30 mins and negligible compare to 12 hours, so that the 'zero' vertical rate in this stage does not affect the overall vertical rate in the calculation.

6.4 Conclusions

The sublimation-recondensation technique is a viable method to produce TiN bulk crystals on tungsten substrates. The stoichiometry of the crystals (N/Ti ratio) is 0.99. Lateral growth predominates initially and vertical growth becomes more important after TiN crystals merge together. The crystal growth rate increases exponentially with temperature, inversely with the total pressure to the 1.5 power, and the calculated activation energy is 775.8±29.8kJ/mol. The XRD and EBSD analysis revealed that the TiN crystals and underlying tungsten substrate grains have an orientation relationship of TiN (001) || W (001) with TiN [100] || W [110], which leads a 45° angle between the TiN and W lattice. For tungsten substrate grains with W (001) planes offset from the surface, the TiN (001) planes are still parallel to W (001) planes to minimize the lattice mismatch.

ACKNOWLEDGEMENTS

The support of the NSF through the grants DMR 0408874 is greatly appreciated. EBSD analysis was conducted at the Oak Ridge National Laboratory SHaRE User Facility, which is sponsored by the Division of Scientific User Facilities, Office of Science, U.S. Department of Energy. Auger Electron Spectroscopy was sponsored by the Assistant Secretary for Energy Efficiency and Renewable Energy, Office of FreedomCAR and Vehicle Technologies, as part of the Oak Ridge National Laboratory High Temperature Materials Laboratory User Program, managed by UT-Battelle, LLC, for the U.S. Department of Energy under contract number DE-AC05-00OR22725.

6.5 References

[129] L.E. Toth, Transition Metal Carbides and Nitrides, Academic Press, New York, 156, (1971)

[130] A.Usui, T. Ichihashi, K.Kobayashi, H, Sunakawa, Y. Oshima, T. Eri, and M. Shibata, Phys. Stat. sol. 194, 572 (2002)

[131] N.C. Chen, W.C. Lien, C.F. Shih, P.H. Chang, T.W. Wang, and M.C. Wu, Appl. Phys. Lett. **88**, 191110, (2006)

[132] M.H. Oliver, J.L. Schroeder, D.A. Ewoldt, I.H. Wildeson, V. Rawat, R. Colby, P.R. Cantwell, E.A. Stach, and T.D. Sands, Appl. Phys. Lett. 93 023109 (2008)

[133] M.A. Moram, M.J. Kappers, Y. Zhang, Z.H. Barber, and C.J. Humphreys, Phys. Stat. Sol. A **205**, 1064 (2008)

[134] Z. Gu, J.H. Edgar, J. Pomeroy, M. Kuball, and D.W. Coffey, J. Mater. Sci.: Mater. Electron., **15**,155, (2004)

[135] T. Zheleva, K. Jagannadham, and J. Narayan, J. Appl. Phys. **75**, 860, (1994)

[136] Pierson, H.O. Handbook of Refractory Carbides and Nitrides, (William Andrew Publishing/Noyes, (1996)

[137] M.W. Chase, Jr., 4th ed. American Chemical Society and American Institute of Physics, Washington D.C., (1998).

[138] Il-seok Kim and Prashant N.Kumta, J. Mater. Chem. **13**, 2003. (2003)

[139] P. Patsalas and S. Logothetidis, J. Appl. Phys. 90, 4725, (2001)

[140] Wikipedia, http://en.wikipedia.org/wiki/Copper

[141] James H. Edgar, Properties of Group III Nitrides, The Institution of Electrical Enginners, London UK, 26-32, (1994)

[142] K. Wasa, S. Hayakawa, Handbook of Sputter Deposition Technology: Principles, Technology and application, Noyes Publications, Park Ridge NJ, 228, (1992)

[143] N. Yokoyama, K. Hinode, and Y. Homma, J. Electrochem. Soc., **136**,882, (1989)

[144] S. Motojima, K. Baba, K. Kitatani, Y. Takahashi, and K. Sugiyama, J. Cryst. Growth, **32**,141, (1976)

[145] Naresh C. Saha and Hadand G. Tompkins, J. Appl. Phys. **72** 3072,(1992)

[146] D. Chaussende, P.J. Wellmann, and M. Pons, J. Phys. **40**, 6150, (2007)

[147] B.M. Epelbaum, M. Bickermann, S. Nagata, P. Heimann, O. Filip, and A. Winnacker, J. Cryst. Growth **305**, 317, (2007)

[148] L. Mercurio, L. Du, J.H. Edgar, and E.A. Kenik, Mater. Res. Soc. Symp. Proc., Pittsburgh, PA 955, (2007)

[149] Material Safety Data Sheet, Electronic Space Products International

[150] D.W. Greenwell, B.L. Markham, F. Rosenberger, J. Crystal Growth **51**, 413, (1981)

CHAPTER 7 - Sublimation Growth of YN Crystals

Published in J. Cryst. Growth, **312**, (2010) 2896-2903

Li Du and J.H. Edgar, Kansas State University, Department of Chemical Engineering, Durland Hall, Manhattan, KS 66506-5102

Roberta A. Peascoe-Meisner, Department of Materials Science and Engineering, University of Tennessee /High Temperature Materials Laboratory, Oak Ridge National Laboratory, Oak Ridge, TN 37831

Yinyan Gong, Silvia Bakalova, Martin Kuball, H.H. Wills Physics Laboratory, University of Bristol, Bristol BS8 1TL United Kingdom

Abstract

The sublimation-recombination crystal growth of bulk yttrium nitride crystals is reported. The YN source material was prepared by reacting yttrium metal with nitrogen at 1200 °C and 800 torr total pressure. Crystals were produced by subliming this YN from the source zone, and recondensing it from the vapor as crystals at a lower temperature (by 50 °C). Crystals were grown from 2000 °C to 2100 °C and with a nitrogen pressure from 125 torr to 960 torr. The highest rate was 9.64 x 10^{-5} mol/hr (9.92 mg/hr). The YN sublimation rate activation energy was 467.1±21.7kJ/mol. Individual crystals up to 200 microns in dimension were prepared. X-ray diffraction confirmed that the crystals were rock-salt YN, with a lattice constant of 4.88Å. The YN crystals were unstable in air; they spontaneously converted to yttria (Y_2O_3) in 2 to 4 hours. A small fraction of cubic yttria was detected in the XRD of a sample exposed to air for a limited time, while non-cubic yttria was detected in the Raman spectra for a sample exposed to air for more than one hour.

Key words: A1: Crystal morphology, Crystal structure, X-ray diffraction, Characterization **A2**: Growth from vapor, **B1**: Yttrium compounds, Nitrides, **PACS code**: **61**. Structure of solids and liquids; crystallography

7.1 Introduction

The transition metal nitrides exhibit a wide range of physical (electrical, magnetic, and optical) and chemical properties that are of technological interest and have commercial applications. Examples include TiN[151] and HfN[152] diffusion barriers for integrated circuits[153]; CrN for hard, wear resistant coatings; ScN for high temperature Ohmic contacts to IIIA nitride semiconductors[154]; and VN which is being investigated as a catalyst[155]. The transition metal nitrides also form alloys, which can be exploited to control their lattice constants and electrical properties, as has been demonstrated with $Ti_{1-x}Sc_xN$[156] and $Y_{1-x}Sc_xN$[157].

Many researchers are investigating the possibility of combining transition metal nitrides with the IIIA nitride semiconductors (aluminum nitride, gallium nitride, and indium nitride) either as layered structures or as alloys, to realize new functional properties. The similar lattice constants and the shared common element (N) have inspired efforts to combine layers as epitaxial films. Scandium nitride[158] and zirconium nitride[159] have been employed as buffer layers between silicon substrates and GaN epitaxial films, to block the initiation and propagation of defects. Additions of chromium, magnesium, and iron to AlN and GaN have all been studied in attempts to create a ferromagnetic semiconductor [160, 161].

Yttrium nitride is particularly intriguing because it is one of the few transition metal nitrides that is also a semiconductor (as is scandium nitride). Several groups reported the rocksalt crystal structure for YN with lattice constants between 4.8 Å and 4.9 Å [162, 163, 164, 165]. No other crystal structure has been experimentally reported for YN, but a recent first principle calculation compared the wurtzite and bcc structures to the rocksalt

structure (the latter was the most stable)[166]. Although no measurement has been reported, studies predicted an indirect bandgap for YN of 0.8eV[166], 0.85eV[167], and 0.544eV[168]. Yttrium nitride is also predicted to exhibit a high Mn solubility, which could impart it will good magnetic properties while retaining its semiconductor properties[169].

In the past, only a few studies have reported the synthesis of YN. In the 1950's, a group produced YN powder by first converting yttrium metal to YH_2 by reacting with hydrogen at 550°C in a quartz tube, then heating this gas to 900°C in the presence of nitrogen[162]. Later in the 1960's, YN powders were obtained by reacting yttrium metal with nitrogen at 1400°C[163] and arc-melting under 0.3 MPa nitrogen[164]. Recently, YN thin films were grown on both silicon and sapphire substrates by laser ablation deposition [170] and reactive magnetron sputtering[171] respectively. Although the lattice constants reported from these different material preparation methods are very close, there are still variations.

In the present study, the sublimation recondensation growth method was employed to produce YN bulk crystals. This technique is attractive for its ability to produce bulk crystals with much low dislocation densities than in thin films on foreign substrates. In addition, its growth rate can be orders of magnitude higher than thin film techniques, ie greater than 10 microns/h. Previously, our group showed ScN[172] and TiN[173] crystals produced by this technique have defect selective etch-pit densities on the order of 10^6 cm^{-2}. The YN growth process was analyzed and the materials produced were thoroughly characterized. The YN crystal morphology was studied by optical and scanning electron microscopy, while its crystal structure and lattice constants were evaluated by x-ray diffraction. The dependence of the YN growth rate on temperature and pressure was established and compared with ScN and TiN sublimation growth under

similar conditions. Lastly, the stability of the YN crystals in air was examined, and the resulting oxidation products reported.

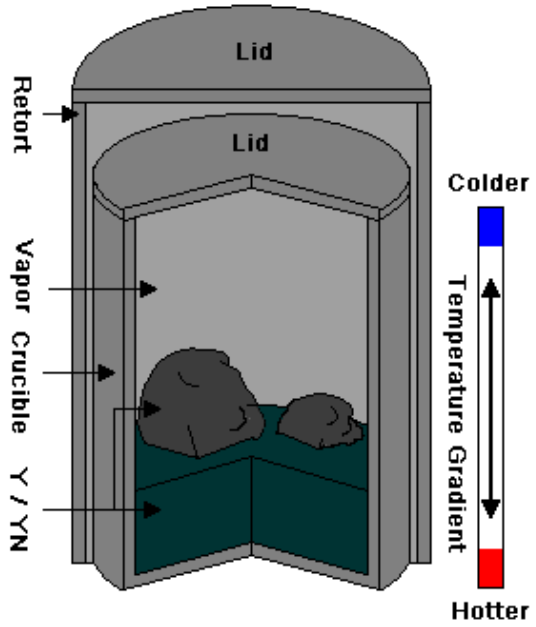

Figure 7.1 The sketch of Y metal nitridizing setup.
The metal chunks turned into nearly black lump one hour later and were ground before continuing nitridizing. The color of Y/YN changed to blue-green as the nitridizing time was increased

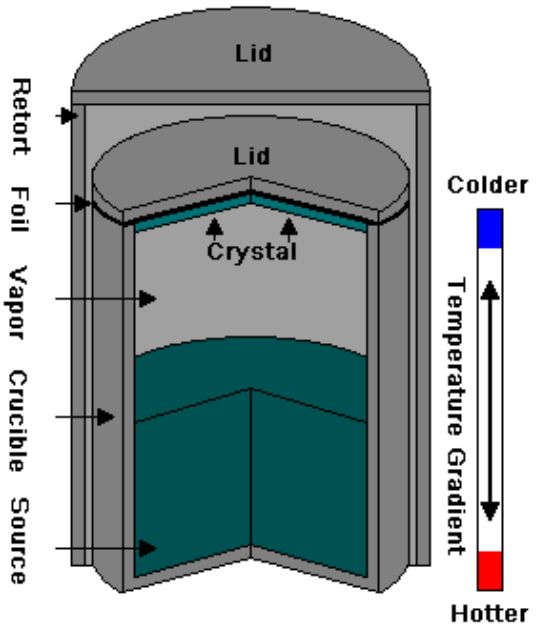

Figure 7.2 Schematic sketch of YN crystal growth.

Tungsten foil was added and served as substrate

7.2 Experimental

The experiments started with YN source synthesis, which was used for the YN crystals growth. Both YN synthesis and crystal growth were conducted in a resistively-heated tungsten furnace with tungsten wire mesh heating elements that provided an axial temperature drop between the source and crystal growth zones. A covered tungsten crucible within a covered tungsten retort was used as the reactor/crystal growth chamber, and the growth temperature was measured by an optical pyrometer focused on the top of the retort.

The YN source was produced by nitridizing the yttrium metal (99.9%) in ultra pure nitrogen atmosphere of 800 torr at 1200°C (Figure 7.1). The conversion of the yttrium metal to YN was monitored by measuring the mass change of Y/YN solid mixture in the crucible to determine its Y/N ratio. The Y/YN mixture was ground into small pieces after the weight measurement, to ensure good contact of nitrogen gas with the mixture in the subsequent nitridizing step.

In the YN crystal growth process, tungsten foil (25 mm diameter) served as the substrate for the deposited YN crystals (Figure 7.2). The YN source was annealed before each growth to reduce the surface oxide as YN crystal easily reacts with oxygen and moisture in ambient air. First, the YN source was baked in a 5% hydrogen and 95% argon gas mixture at 900 torr and 1200°C for about 4 hours. Then it was heated in ultra pure nitrogen gas at 250 torr and 1900°C for another 8 hours. A similar process has proven effective in reducing the surface oxide in our AlN[174] and TiN[173] crystal growths. The YN growth rate was investigated as function of growth temperature (2000 - 2100 °C) pressure

(125 - 960 torr) and time (16 to 48 hours). A temperature difference of approximately 50°C was maintained between the source and crystal growth zones. The overall growth rate was determined by dividing the YN crystal mass increase by the growth time. After the YN crystals were synthesized, some were sealed into glass tubes at high vacuum (2 x 10^{-5} torr) to prevent oxidation during storage.

Characterization of the YN crystals included Raman spectroscopy and x-ray diffraction. Raman measurements were performed with a Renishaw InVia micro-Raman system using a 488 nm Ar ion (60mW) laser as excitation source. To identify the phases presented by x-ray diffraction, both the source materials and grown crystals were ground into fine powders and stored in an air sensitive sample holder (to prevent oxidation). . The XRD data were collected on a PANalytical X'Pert Pro diffractometer with Cu Ka radiation (45 kV / 40 mA) using parabolic mirrors with parallel plate collimator (0.09°) and miniprop point detector. Continuous scans were taken between 20° to 100° (2-theta). Diffraction patterns were analyzed using the ICDD powder diffraction files and JADE or High Score software packages to identify crystalline materials. The grain sizes (the projected area of individual crystals) were measured using scanning electron microscopy (SEM, S-3500N, Hitachi Science Systems, Ltd, Japan) and averaged from a number of condensed YN crystals

7.3 Results and Discussion

Yttrium metal has a melting point of 1509 °C and boiling point of 3030 °C[175] , and it is easily nitridized at 1200 °C in a pure nitrogen atmosphere with the possible reaction of:

$$Y(s) + 0.5N_2(g) \leftrightarrow YN(s) \qquad (7\text{-}1)$$

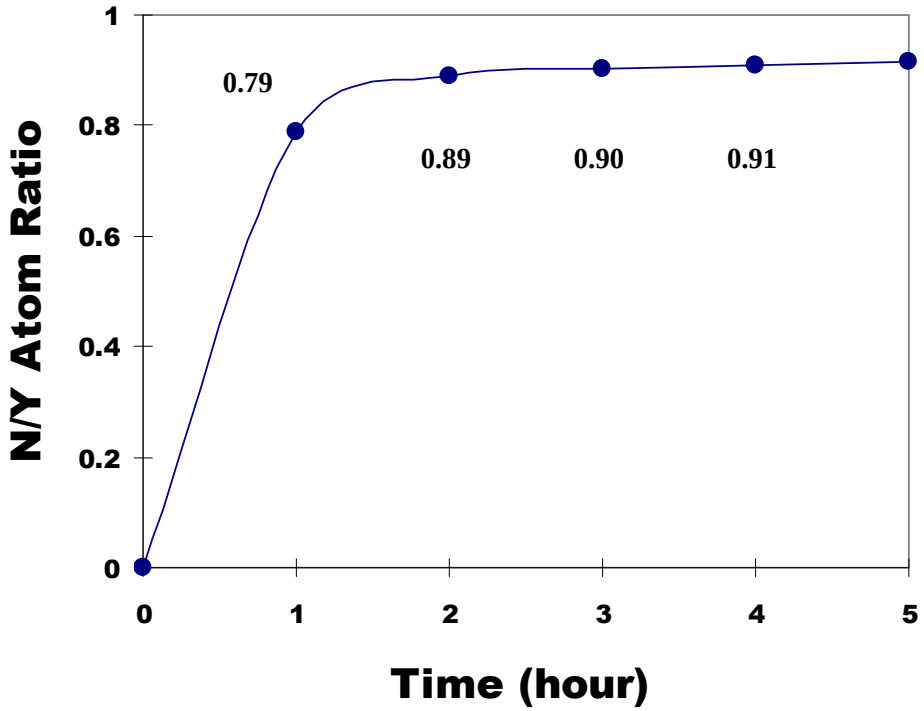

Figure 7.3 The calculated nitrogen to yttrium atom ratio versus nitridizing time In ultra pure nitrogen atmosphere of 800 torr at 1200°C.

In analyzing yttrium nitridation, the loss of yttrium by vapor transport to the furnace chamber was negligible; it is prevented by employing double containers (crucible and retort). Thus, the mass increase is due primarily to the addition of nitrogen to the solid. From the change in mass, the nitrogen to yttrium atom ratio can be calculated. Figure 7.3 showed the calculated nitrogen to yttrium atom ratio versus nitridizing time. After only one hour of nitridizing, the nitrogen to yttrium atomic ratio increased rapidly from 0 to 0.79. Subsequently, the rate slowed, increasing to 0.89 and 0.90 after the second and third hours. This ratio stayed nearly constant around 0.91 with longer nitridation times. Although the Y/YN solid mixture was ground into powder every time before the next nitridizing step, heating still caused it to sinter together. This sintering and reduction of exposed surface area may slow down nitridation, preventing its completion. After nitridizing for more than 90 hours, the source materials were metallic gray blue-

green, with the cubic crystal grains formed on the source surface. X-ray diffraction confirmed that there was no un-reacted yttrium metal left in the source material.

Thus the reactions involved in the crystal growth process were yttrium nitride sublimation in the source zone at a relatively high temperature and recondensation in the crystal growth zone at a relatively low temperature:

$$2YN(s) \leftrightarrow 2Y(g) + N_2(g) \qquad (7\text{-}2)$$

7.3.1 Morphology

The as-received yttrium was hard silvery metal chunks. After one hour nitridizing, the chunks turned black and were easily fractured. As the nitridizing time was increased, the color of the Y/YN mixture changed towards the blue-green. In the end, the YN produced by sublimation crystal growth is a gray blue-green crystal as shown in Figure 7.4

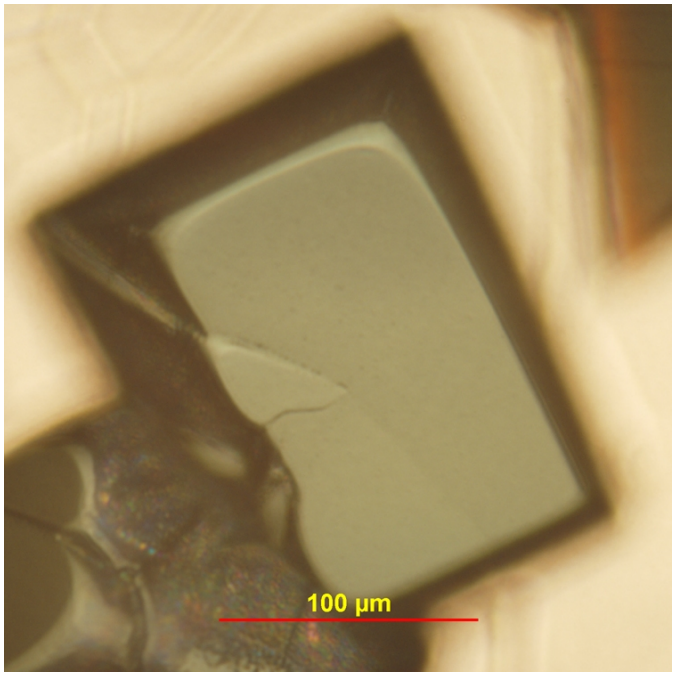

Figure 7.4 Optical microscope image of YN crystals on tungsten
As-produced the YN is gray green and cube or cubiod is the regular shape of the crystals

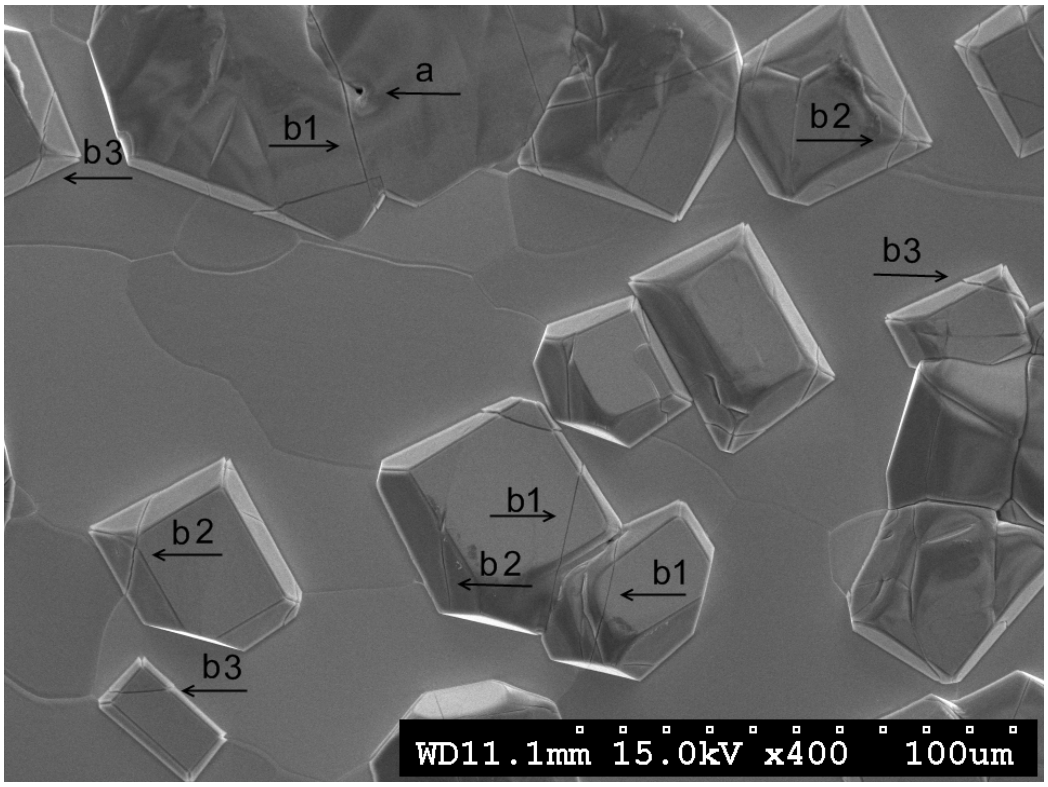

Figure 7.5 SEM top view of YN crystals grown for 16 hours at 960 torr, 2000 ˚C Most individual grains were regular shaped, while merged grains were less regular, and had rough surfaces. Lines (b) on the surface and micro hollows (a) with size about 2 ~ 3 micron on the grain boundaries were observed.

Figure 7.5 shows the SEM image for YN crystals grown 16 hours at 960 torr, 2000 ˚C. After 16 hours growth, although most grains were regularly shaped cubes or cuboids, wedge, tetrahedron, pyramid, frustum, truncated octahedrons, and truncated tetrahedrons were also observed. As the grains merged together, they displayed less regular shapes, and the surfaces became rough. Straight lines on the parameters of the crystals and micro hollows (upper-left in Fig. 5) with size about 2 ~ 3 micron on the grain boundary were observed. The straight lines were seen on all the samples while micro hollows were found mostly on samples grown at higher temperature or longer time. The line features were found on the merged grains (Fig.5b1), on the grains grown on substrate grain boundary (Fig.5b2), and also on single grain grown on single substrate grain (Fig.5b3). If the lines occurred at regular shaped grains (cubes or cuboids), they usually

were at an angle of 45 ° to the square edges. For the same growth time and pressure, the average crystal size for higher growth temperature was larger, increasing from 1.5 x $10^{-3}mm^2$ at 2000 ˚C to 2.5 x $10^{-3}mm^2$ at 2050 ˚C (Fig. 6a) and 5.0 x $10^{-3}mm^2$ at 2100 ˚C(Fig. 6b,c,d). This result was the same for other transition metal nitride ScN[172] and TiN[173] crystal growth in our previous studies. However, the lines and micro hollows became more evident at higher temperature as more crystal grains merged together. Fig. 6b shows the nearby micro hollows on the crystal boundary 16 hours at 960 torr, 2100 ˚C. Whereas single crystal grains on the sample still maintained cube, pyramid (Fig. 6c), or frustum (Fig.6d) shapes.

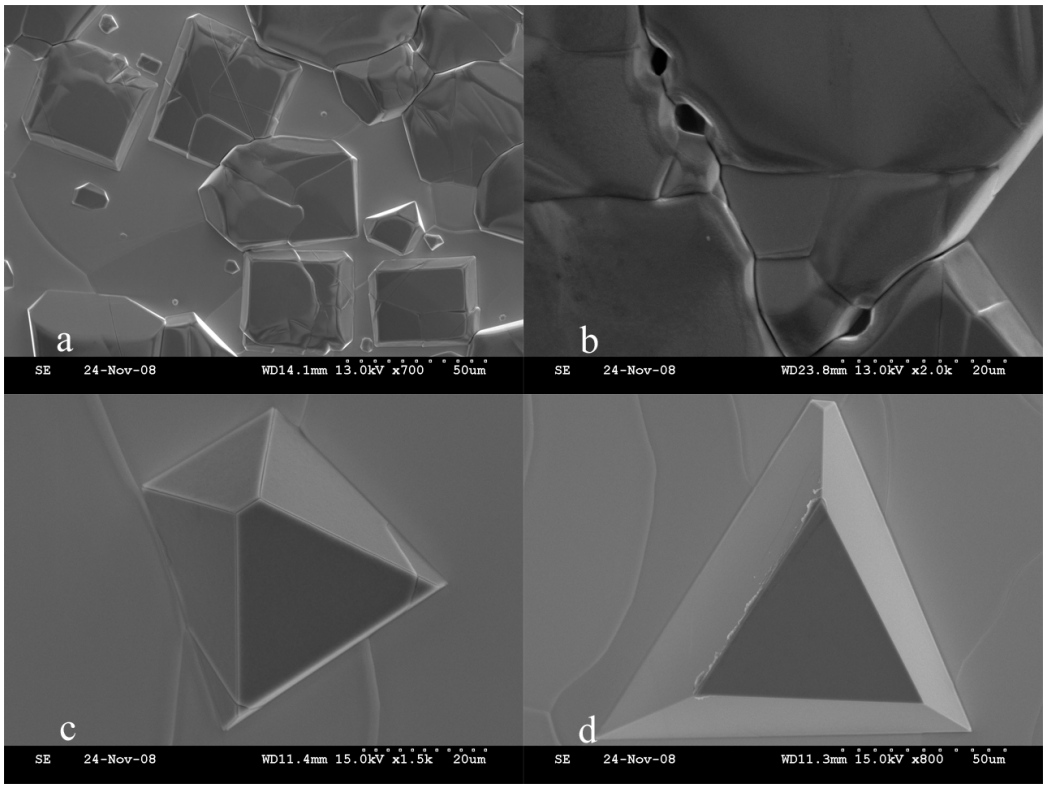

Figure 7.6 SEM imagines of YN crystals

YN crystals grown for 16 hours at 2050 ˚C, 960 torr(a) and 2100 ˚C, 960 torr (b, c, d) Most grains were cubes and cuboids(a), other shapes like wedge(c) and fustum(d)were also observed; micro hollows became more evident at higher temperature as more crystal grains merged together(b)

Reducing the pressure also has a significant effect on growth rate. Growing crystals for the same amount of time and temperature but at a lower pressure produced

larger crystals. For a YN sample grown 16 hours at 740 torr, 2000 ˚C, the estimated average grain size of crystals was 10 x 10^{-3} mm^2 - much larger than one grown at 16 hours at 960 torr, 2100 ˚C. This result is also confirmed for ScN [22] and TiN [23] crystal growth in our previous studies.

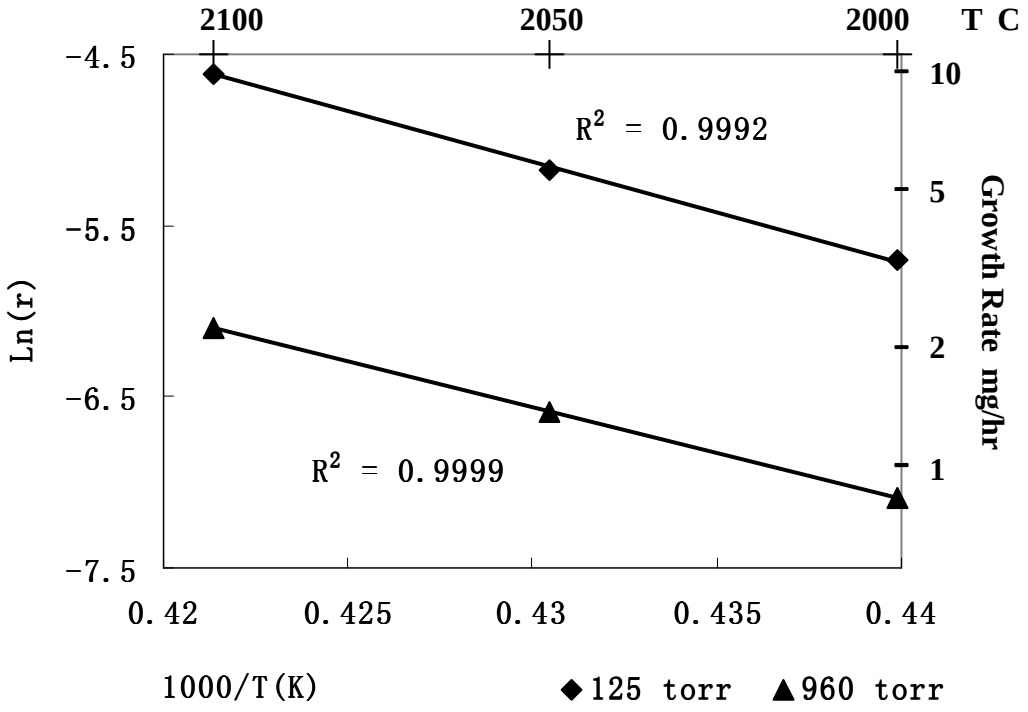

Figure 7 The variation of the logarithmic growth rate on reciprocal growth temperature at constant growth pressure.

7.3.2 Overall Growth Rate

The temperature and pressure effects on the sublimation growth of YN is the same as the other transition metal nitrides, ScN and TiN; increasing the temperature or decreasing the pressure enhances its crystal growth rate. However, the growth rate of YN is lower than either ScN or TiN. The YN sublimation growth rate was 3.24 x 10^{-5} mol/hr (3.33mg/hr) at 2000 °C, 125 torr, while the ScN sublimation growth rate from our unpublished work was 9.65 x 10^{-5} mol/h (5.69 mg/hr) at same temperature but higher

pressure of 150 torr. The highest growth rate for YN in this study was 9.64 x 10^{-5} mol/hr (9.92 mg/hr) at 2100 °C and 125 torr, while the TiN had a growth rate of 3.22 x 10^{-4} mol/h (19.92mg/hr) at same temperature but higher pressure of 150 torr from our previous study[176]. Decreasing the pressure has a more significant effect on overall growth rate than increasing the temperature Figures 7 and 8 shows the dependence of the growth rate on temperature and pressure: the logarithmic growth rate is first order dependent on reciprocal temperature, while growth rate itself varies approximately linearly with reciprocal pressure.

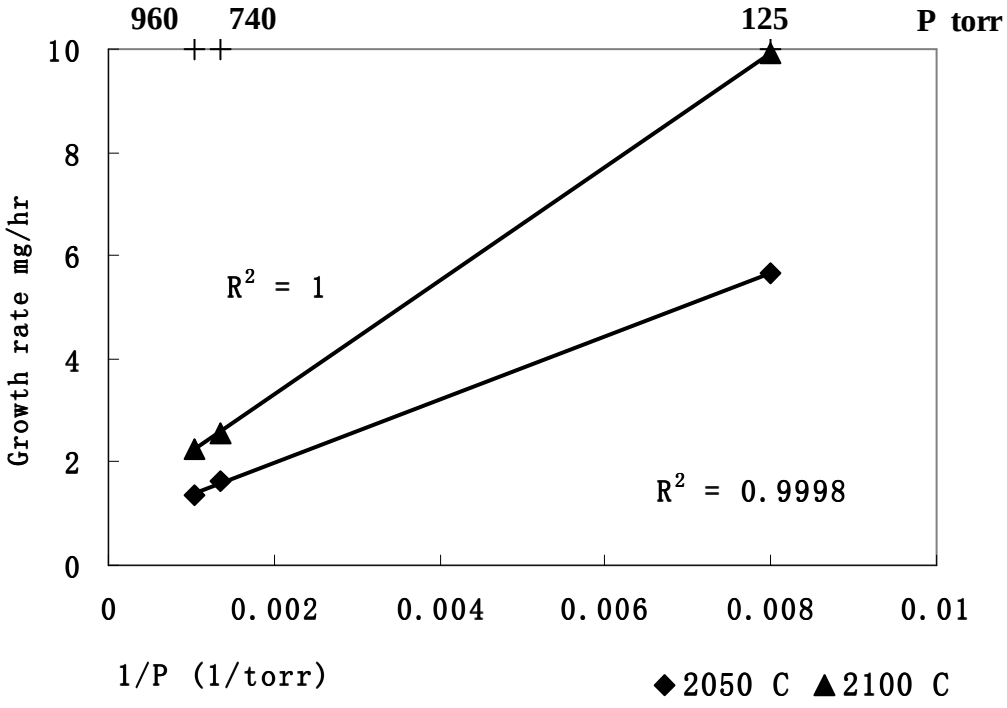

Figure 8 The growth rate variation with reciprocal pressure at constant growth temperature.

The activation energy of the growth was determined by combining the Arrhenius equation with sublimation-recondensation kinetics:

$$\left.\begin{array}{l} r = d\alpha / dt = kf(\alpha) \\ \ln r = (-\dfrac{Ea}{RT}) + \ln A \end{array}\right\} \Rightarrow \ln \frac{d\alpha}{dt} = (-\frac{Ea}{RT}) + \ln A + \ln f[\alpha] \qquad (7\text{-}3)$$

where *Ea* is the activation energy, *A* is the pre-exponential factor or frequency factor, *R* is the ideal gas constant, *r* is the growth rate, α is the degree of conversion, and $f(\alpha)$ is a mathematical function whose form depends on the reaction type.

In equation 3, although the relationship between the rate constant *k* and the growth rate ($(d\alpha / dt) = kf(\alpha)$) has not been determined for Y+N system, we previously showed that if the equilibrium can be assumed at the surfaces of the source and seed, $f(\alpha)$ is approximately constant [25]. The demonstration is as following:

Since the transport of growth species from source to growing surface is often the rate limiting step in vapor crystal growth [20], equilibrium can be assumed at the surfaces of the source and seed. For reaction (4):

$$K^{eq} = \frac{[Y]^2[N_2]}{[YN]^2} = \frac{(f_Y{}^{eq})^2 (f_{N_2}{}^{eq})}{(a_{YN}{}^{eq})^2} \qquad (7\text{-}4)$$

The growth pressures used in this study were not high (<1.25 atm), so solid species activity is close to unity and gas fugacity can be represent by gas species partial pressure, that is:

$$K^{eq} = (P_Y{}^{eq})^2 (P_{N_2}{}^{eq}) \qquad (7\text{-}5)$$

For a fixed growth temperature and pressure, the local gas phase species concentration at the growth surface remains the same and $f(\alpha)$ is approximately constant. Therefore, the sublimation growth rate is proportional to the rate constant and yields a first order dependence of logarithmic growth rate on reciprocal temperature at same pressure (confirmed in Fig. 7):

$$\frac{d\ln r}{dT} = \frac{Ea}{RT^2}\left(r = \frac{d\alpha}{dt}\right) \tag{7-6}$$

The deduced YN sublimation activation energy is 467.1±21.7kJ/mol (from Fig. 7), which is similar with activation energy of ScN (456.0 kJ/mol[172]), and lower than that of TiN (775.8±29.8kJ/mol[176]).

7.3.3 Composition and structure

The YN crystals grown for 48 hours at 2000 °C and 740 torr were ground into a fine powder and examined by x-ray diffraction (Figure 7.7). Table 1 lists the peak position, peak intensity, d-spacing and corresponding crystal planes of the eight strongest peaks. The space group of the sample was identified as Fm-3m and the crystal structure was confirmed as rocksalt (NaCl), with 4 YN per unit cell. The calculated lattice parameters were 4.88Å (a=b=c) and 90^o (α=β=γ) with a cell volume of 116.27x10^5 pm^3. The calculated density for produced YN crystals was 5.87g/cm^3 at 25 °C. YN structure information from literatures was listed in Table 2 and their calculated lattice constants bracketed our refined value. Since these YN crystals were produced at different conditions, it is possible that variations in the stoichiometry and residucal impurity concentrations may have caused the small fluctuation lattice constant values.

Figure 7.8 shows the Raman spectrum of YN crystals grown for 48 hours at 2000°C and 760 torr. First order Raman scattering is symmetry forbidden for the rock salt crystal structure. The apparent features in the Raman spectrum are disorder-induced first-order Raman scattering and corresponds to the density of phonon states. Three crystals were selected for analysis (inset) and they all have similar spectra. Note photoluminescence was superimposed on the Raman spectra in the spectral range of the

Raman spectra, i.e., as using 488nm laser excitation, around this wavelength. There is no literature data on Raman spectra of YN, thus, we compared our results with that of other transition metal nitrides, e.g. ZrN (same rock salt structure without greatly changing the mass of the metallic ion; due to different electronic structure an effect of the free carriers on the phonon modes however may be expected)[177] and ScN (same rock salt structure, close electronic structure, but the atomic mass ratio is $M_{Sc}/M_Y \approx 0.5$, implying that the Raman peaks are shifted in first approximation as $\omega_{YN}/\omega_{ScN} \approx (M_{Sc}/M_Y)^{1/2}=0.711$)[178]. Hence, the broad Raman peaks at ~318 cm^{-1} and 360-400 cm^{-1} could be attributed to acoustic phonons in cubic YN. The broad peak with lower intensity at ~500 cm^{-1} most probably originated from optical phonons.

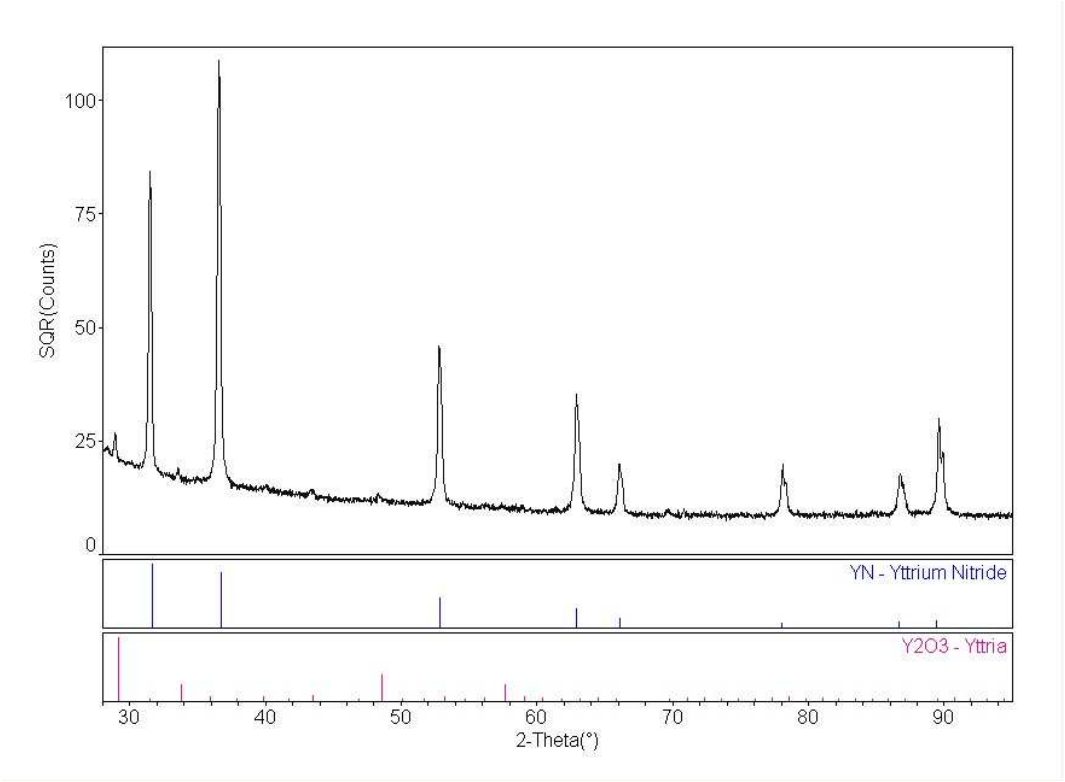

Figure 7.7 X-ray diffraction for YN crystals grown 48 hours at 2000°C, 740torr

Peak No.	(h k l)	2-Theta	d-spacing(Å)	Intensity[%]
1	(1 1 1)	31.7285	2.81790	100.00
2	(2 0 0)	36.7998	2.44038	89.54
3	(2 2 0)	53.0250	1.72561	51.05
4	(3 1 1)	63.1269	1.47160	34.11
5	(2 2 2)	66.2843	1.40895	15.23
6	(4 0 0)	78.2915	1.22019	6.58
7	(3 3 1)	86.9343	1.11972	13.24
8	(4 2 0)	89.7900	1.09137	18.49

Table 7.1 X-ray powder diffraction data for YN

Reference Code	Lattice Constant	Sample Preparation
This study	4.88075 Å	Gray green color, prepared by sublimation at 2000 °C, 960 torr
162	4.877 Å	obtained by converting yttrium metal to YH_2 then to YN (powder diffraction)
163	4.8699 Å	Blue violet color, prepared by reaction of metal at 1673 K (powder diffraction)
164	4.8920 Å	Arc-melted under 0.3 MPa nitrogen (powder diffraction)
165	4.8935 Å	Annealed at 1673K under argon or nitrogen (powder diffraction)
171	0.491(3)nm	Reactive magnetron sputtering

Table 7.2 Literature information for previous synthesis studies of YN
Structure reference from [12] to [15]; calculated from LPF using POWD-12++

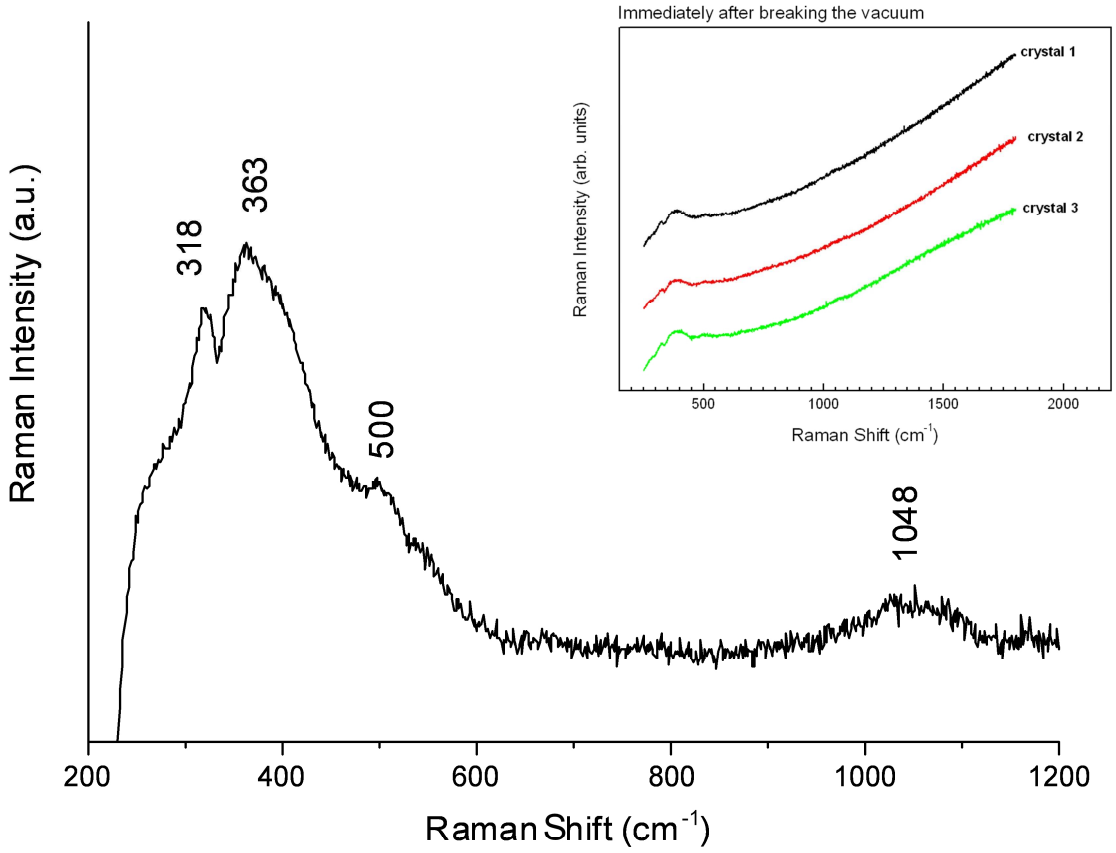

Figure 7.8 Raman spectrum of YN crystals grown for 48 hours at 2000°C, 760 torr. Photoluminescence background is subtracted. Inset shows Raman spectrum (background not subtracted) from three different crystals, showing consistent Raman spectra over different crystals measured.

7.3.4 Oxidation

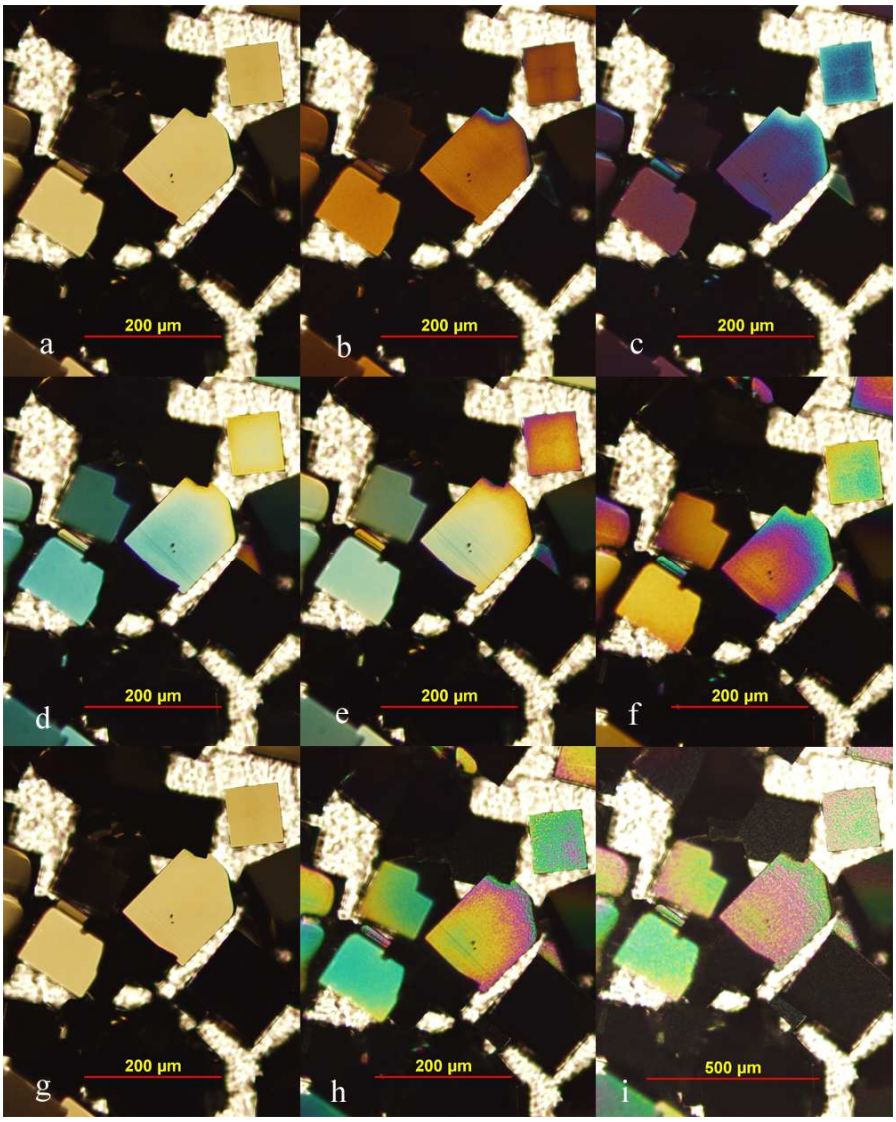

Figure 7.9 Optical micrographs of YN crystals upon exposure time to air
The apparent color of YN crystals changed with time upon exposure time to ambient air. The time interval between each image is 5 minutes

The yttrium nitride crystals readily oxidized in air at room temperature. After exposure to air for twenty minutes, the gray green color turned into blue violet, and two hours later it changed to black. The colors observed under microscope with strong reflection light (Figure 7.9) included red, orange, yellow, green, blue, indigo, violet and mauve. Photos were taken every 20 minutes. Sample crystals showed a yellow color 5

minutes after initial air exposure (Fig. 5.19a), and turned to orange 20 minutes later (Fig. 5.19b). The sample then looked blue-violet 40 minutes after the first photo was taken (Fig. 11c) and changed to green-yellow 20 minutes later (Fig. 5.19d). These colors were repeated as the thickness of the oxidation layer increases, and the surface roughness increased.

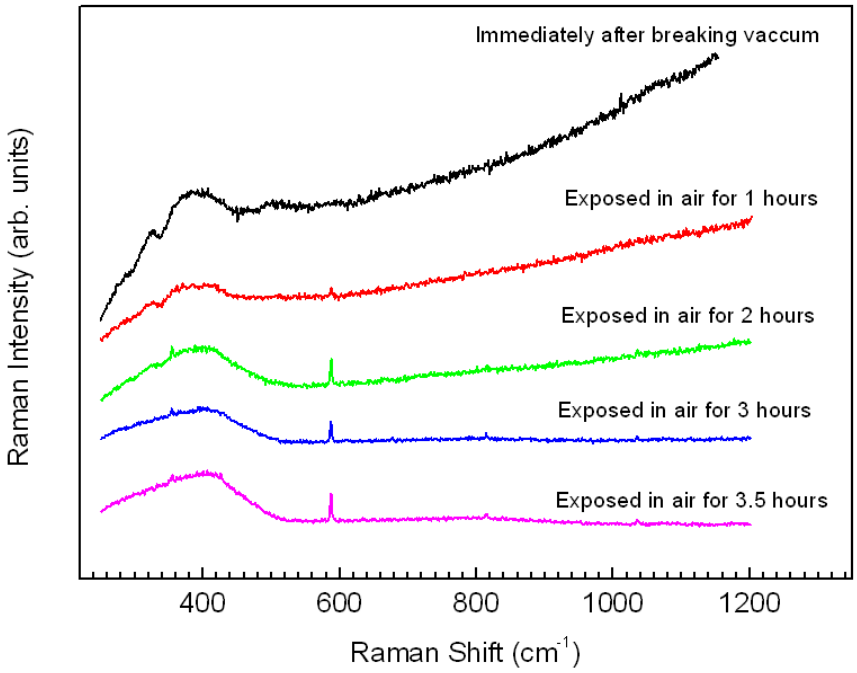

Figure 7.10 Raman spectra for YN after exposed to air for different duration of time

Even for YN samples sealed under a high vacuum in a glass tube and ground to powder in a air-free glove box before x-ray diffraction, oxidation products were still observed. The tiny peak (3.86% intensity) appearing at 29.1665 (2-Theta) in Figure 9 did not originate from YN. Rietveld refinement for the XRD pattern of YN in an air sensitive sample holder indicated that roughly 96 wt% of the examined sample was yttrium nitride; the remaining 4 wt% was crystalline yttrium oxide. The space group of this yttrium oxide is Ia-3, the calculated O and Y ratio in its unit cell is 3:2, and the lattice parameters are

10.598Å (a=b=c) and 90^{o} (α=β=γ), which suggested the formation of c-type yttrium oxide after limited air exposure.

Figure 12 is the Raman spectra from an YN crystal sample after exposed to air for different time durations. A sharp peak at ~587cm^{-1} was observed after the sample was exposed to air for 1 hour; it becames more pronounced with time. This peak position is close to that reported for yttrium oxide [177] but not the cubic (c-type) structure. This result implies the formation of non-cubic yttrium oxide, monoclinic (β-type) and rhombohedral (α-type) after exposure to air for more than one hour.

7.4 Conclusions

With fully nitridized yttrium as the source, the sublimation-recondensation technique proved viable for producing YN bulk crystals on tungsten substrates. The growth temperature and pressure are the major factors that impact the morphology and growth rate of YN crystals. Experiments proved that the growth rate increases exponentially with temperature, inversely with the total pressure, and this trend is the same with ScN and TiN crystal growth under sublimation recondensation technique. The highest growth rate was 9.64 x 10^{-5} mol/hr after 24 hours of growth at 2100 °C and 125 torr. Combining the Arrhenius equation with growth kinetics, the deducted activation energy was 467.1±21.7kJ/mol. Crystal structure of YN was confirmed as rocksalt (NaCl) with 4 YN in the unit cell by x-ray diffraction. The calculated lattice constant was 4.88Å, which is bracketed by values reported in the literature. YN has a poor stability in the air. XRD patterns indicated present of cubic yttrium oxide in YN sample after exposure to air for limited time, while the Raman spectra implied the present possibility of none-cubic yttrium oxide in samples that exposure to air for more than one hour.

ACKNOWLEDGEMENTS

The support of II-VI Foundation is greatly appreciated. X-ray diffraction analysis at the Oak Ridge National Laboratory's High Temperature Materials Laboratory was sponsored by the U.S. Department of Energy, Office of Energy Efficiency and Renewable Energy, Vehicle Technologies Program. We would like to thank Ms. Yi Zhang and Mr. Clinton Whiteley for sample preparation.

7.5 References

[151] M.Y. Kwak, D.H. Shin, T.W. Kang, and K.N. Kim, *Characteristics of TiN barrier layer against Cu diffusion*, Thin Solid Films **339**, 290, (1999)

[152] R.A. Araujo, X. Zhang, and H. Wang, *Cubic HfN thin films with low resistivity on Si (001) and MgO (001) substrates*, J. Electron. Mater. **37**, 1828 (2008)

[153] B. Navinsek, P. Panjan, I. Milosev, *Industrial applications of CrN (PVD) coatings*, deposited at high and low temperatures, Surf. Coat.Technol. **97**,182, (1997)

[154] X.W. Bai and M.E. Kordesch, Structure and optical properties of ScN thin films, Appl. Surf. Sci., 175-176, 499, (2001)

[155] H. Kwon, S. Choi, and L.T. Tompson, *Vanadium nitride catalysts: synthesis and evaluation for n-butane dehydrogenation*, J. Catal. **184**, 236, (1999)

[156] J.M. Gregoire, S.D. Kirby, M.E. Turk, and R.B. Van Dover, Structural, electronic and optical properties of (Sc,Y)N solid solutions, Thin Solid Films **517**, 1607 (2009)

[157] D. Gall, M. Stoehr, and J. E. Greene, *Vibrational modes in epitaxial Ti1-xScxN(001) layers: An ab initio calculation and Raman spectroscopy study*, Physical Review B, **64**, 174302,

[158] M.H. Oliver, J.L. Schroeder, D.A. Ewoldt, I.H. Wildeson, V. Rawar, R. Colby, P.R. Cantwell, E.A. Stach, and S.D. Sands, *Organometallic vapor phase epitaxial growth of GaN on ZrN/AlN/Si substrates*, Appl. Phys. Lett. **93**, 023109 (2008)

[159] C.F. Johnston, M.A. Moram, M.J. Kappers, and C.J. Humphreys, Defect reduction in (1122) semipolar GaN on m-plane sapphire using ScN interlayers, Appl. Phys. Lett. **94**, 161109 (2009)

[160] S.G. Yang, A.B. Pakhomov, S.T. Hung, and C.Y. Wong, *Room-temperature magnetism in Cr-doped AlN semiconductor films*, Appl. Phys. Lett. **81**, 2418 (2002)

[161] M. Zajac, J. Gosk, E. Grzanka, M. Kaminska, A. Twardowski, B. Strojek, T. Szyzko, and S. Podsiadlo, *Possible origin of ferromagnetism in (Ga, Mn)N*, J. Appl. Phys. **93**, 4715, (2003)

[162] Charles P. Kempter, N.H. Krikorian, Joseph C. McGuire, *The crystal structure of yttium nitride*, J. Phys. Chem. **61**, 1237, (1957)

[163] F. Anselin, C.r. Hebd Seances Acad. Sci., **256**, 2616, (1963)

[164] H. Holleck, Smailose E., Thummler., J. Nucl. Mater., **32**, 281, (1969)

[165] H.P. Klesnal, P.Rogl, High Temp. High Pres.**22**,453, (1990)

[166] S. Zerroug, F. Ali Sahraoui ,N. Bouarissa, Ab initio calculations of yttrium nitride:structural and electronic properties, Appl Phys A **97**, 345, (2009)

[167] C. Stampfl, W. Mannstadt, R. Asahi, and A. J. Freeman, *Electronic structure and physical properties of early transition metal mononitrides: Density-functional theory LDA, GGA, and screened-exchange LDA FLAPW calculations*, Phys. Rev. B **63**, 155106, (2001)

[168] T. Lü and M. Huang, *Electronic structure of ScN and YN: density-functional theory LDA and GW approximation calculations,* Chinese Physics **16**, 62, (2007)

[169] X. Jia, W. Yang, and M. Qin, *Magnetism in Mn doped yttrium nitride: first-principles calculations*, Appl. Phys. Lett. **93**, 222501, (2008)

[170] W.De La Cruz, J.A. Diaz, L. Mancera, N. Takeuchi, G. Soto, *Yttrium nitride thin films grown by reactive laser ablation*, J. Phys. Chem. Solids **64**, 2273, (2003)

[171] John M. Gregoire, Steven D. Kirby, George E. Scopelianos, Felix H. Lee, and R. Bruce van Dover, *High mobility single crystalline ScN and single-orientation epitaxial YN on sapphire via magnetron sputtering*, J. Appl. phys., **104**, 074913, (2008)

[172] Z. Gu, J.H.Edgar, J.Pomeroy, M. Kuball, D.W.Coffey, *Crystal growth and properties of scandium nitride*, J. Mater. Sci.: Mater. Electron., **15**, 555 (2004)

[173] Li Du, J.H. Edgar, Edward A. Kenik and Harry Meyer III, *Sublimation growth of titanium nitride crystals*, J. Mater. Sci.: Mater. Electron. **21**, 78, (2010)

[174] J.H. Edgar, L. Du, R.G. Lee, L. Nyakiti, J. Chaudhuri, Native oxide and hydroxides and their implications for bulk AlN crystal growth, J. Cryst. Growth 310 (2008) 4002-4006

[175] H.E. Boyer and T.L. Gall editors, Metals Handbook - Desk Edition, (ASM, Metals Park, OH, 1985).

[176] [26] D.W. Greenwell, B.L. Markham, F. Rosenberger, *First and second order Raman scattering in transition metal compounds*, J. Cryst. Growth **51,** 413, (1981)

[177] W. Spengler and R. Kaiser, Solid State Commun. **18**, 881 (1976)

[178] G. Travaglini, F. Marabelli, R. Monnier, E. Kaldis and P. Wachter, *Electronic structure of ScN*, Phys. Rev. B **34**, 3876 (1986)

CHAPTER 8 - Conclusions

8.1 Main results

This research aimed to explore the growth of potential substrates suitable for AlGaInN technology. Homoepitaxy growth of AlGaInN epilayers are in great demand because the disadvantages of the conventional substrates, sapphire and SiC are restricting the AlGaInN devices technology development. High impurities concentrations, high cost, and limited usable area limits the application of current commercialized AlN substrate.

Prior to the experiment research, the species responsible for impurities incorporation in different systems were identified from thermodynamic analysis. High temperature sintering (>1900 °C) was proved to be important in reducing oxygen. Low temperature growth can possible limit SiC degradation Carbothermal reduction at a low temperature can reach the minimum AlN mass loss possible. Then a two step process was shown to be effective both theoretically and experimentally in reducing impurities in AlN source. More than 98% of the oxygen, 99.9% of hydrogen, and 90% of carbon originally in the source was removed.

In the self-seeded growth of AlN study, polycrystalline AlN boules with preferential (0001) orientation were obtained. AlN crystals with large grain size were achieved in the self-seeded growth. In seeded growth, SiC substrates are thermally etched at temperature higher than 1520 °C, and the AlN grown at this temperature or above tend to crystallize from the etch pits. At growth temperature of about 1432 ~1460°C, almost no etch pits were formed for samples originated from polycrystalline source and the

obtained AlN crystals were uniformly distribution over the polished substrate. The use of O-rich AlN powder source in the growth increases the SiC decomposition and promotes Al transport. The substrates were heavily etched even at conditions in which no thermal etching was found in the growth with very low oxygen-containing source. But if the substrate surface was scratched, crystals tend to nucleate from these scratches. Thus, low temperature growth with low oxygen concentration source is more effective in protecting the SiC substrate from thermal etching. The AlN crystals can be deposited on both Si-face and C-face of *c*-plane SiC, as well as *m*-plan SiC substrates. The growth surface of grains is always parallel to the c-plane. The grains tend to have same tilt with the substrate. However, the growth conditions for *m*-plan SiC is very critical. Continuous AlN crystals growth on *m*-plane SiC was achieved at 1428 ~1460 ˚C and 600 torr. Very few irregular crystals but etch pits was found at same pressure but temperature higher than 1520 ˚C; therefore, low temperature growth is more effective for m-plan SiC.

Physical vapor transport was shown to be a viable method to produce TiN and YN crystals on tungsten substrates. The stoichiometry of the TiN crystals (N/Ti ratio) is 0.99. Lateral growth predominates initially and vertical growth becomes more important after TiN crystals merge together. The crystal growth rate increases exponentially with temperature, inversely with the total pressure to the 1.5 power, and the calculated activation energy was 775.8±29.8kJ/mol. The XRD and EBSD analysis revealed that the TiN crystals and underlying tungsten substrate grains have an orientation relationship of TiN (001) || W (001) with TiN [100] || W [110], which leads a 45° angle between the TiN and W lattice. For tungsten substrate grains with W (001) planes offset from the surface, the TiN (001) planes are still parallel to W (001) planes to minimize the lattice mismatch.

With fully nitridized yttrium as the source, the sublimation-recondensation technique proved viable for producing YN bulk crystals on tungsten substrates. The growth temperature and pressure are the major factors that impact the morphology and growth rate of YN crystals. Experiments proved that the growth rate increases exponentially with temperature, inversely with the total pressure, and this trend is the same with ScN and TiN crystal growth under sublimation recondensation technique. The highest growth rate was 9.64×10^{-5} mol/hr after 24 hours of growth at 2100 °C and 125 torr. Combining the Arrhenius equation with growth kinetics, the deducted activation energy was 467.1±21.7kJ/mol. The crystal structure of YN was confirmed as rocksalt (NaCl) with 4 YN in the unit cell by x-ray diffraction. The calculated lattice constant was 4.88Å, which is bracketed by values reported in the literature. YN has a poor stability in the air. XRD patterns indicated present of cubic yttrium oxide in YN sample after exposure to air for limited time, while the Raman spectra implied the present possibility of none-cubic yttrium oxide in samples that exposure to air for more than one hour.

8.2 Future work

The oxygen concentration in well grown AlN bulk crystals is still high currently. How to remove oxygen in the obtained bulk crystal AlN remain challenging. Detailed impurities analysis is needed to minimize their concentration maximum possible.

Detailed thermodynamic, kinetics study and reactor design are needed to further enlarge of the single AlN crystal size for physical vapor transport method or other proposed concepts.

Testing TiN as a substrate for AlGaInN epitaxy or combined layer has not been done yet. Although the nitridation of Zr metal was studied in general in my work (not included in this thesis), the bulk crystal growth and characterization of ZrN haven't been researched in detail yet.

The semiconducting, magnetic, and optical properties of transition metal nitrides remained to be explored. There are also interesting properties from alloys or layered structures of transition metal nitrides combined with group III nitrides need more investigation.